Title
Development of Co-Ni-Ga Ferromagnetic Shape Memory Alloys (FSMAs) by Investigating the Effects of Solidification Processing Parameters

Author
Kalaantari, Haamun

Publication Date
2013

UNIVERSITY OF CALIFORNIA
RIVERSIDE

Development of Co-Ni-Ga Ferromagnetic Shape Memory Alloys (FSMAs) by Investigating the Effects of Solidification Processing Parameters

A Dissertation submitted in partial satisfaction
of the requirements for the degree of

Doctor of Philosophy

in

Mechanical Engineering

by

Haamun Kalaantari

March 2013

Dissertation Committee:
Professor Reza Abbaschian, Chairperson
Professor Cengiz Ozkan
Professor Javier Garay

The Dissertation of Haamun Kalaantari is approved:

Committee Chairperson

University of California, Riverside

Acknowledgments

I wish to take this opportunity and express my appreciation and respect to all of them who made my journey unforgettable to this point.

First and the foremost, I am deeply indebted and thankful to my PhD advisor, Professor Reza Abbaschian for all of his enlightening guidance, unreserved support, kindness, generosity, motivation, enthusiasm and the confidence he gave me through each single step of this journey. He taught me a lot through those numerous research and stimulating discussions and provided me with constructive suggestions. His mentorship was paramount in providing a well-rounded experience consistent with my long-term career goals. I have been amazingly fortunate to have an advisor who gave me the freedom to explore on my own, and at the same time the guidance to recover when my steps faltered. His patience and support helped me overcome many crises and finish this dissertation. He encouraged me to grow not only as an experimentalist but also as an instructor and an independent thinker. I am not sure many graduate students are given the opportunity to develop their own individuality and self-sufficiency by being allowed to work with such independence. For everything you have done for me, Professor Abbaschian, I thank you.

My thanks also go to the members of my internal dissertation committee, Professor Cengiz Ozkan and Professor Javier Garay for reading the research proposal and previous drafts of this dissertation and providing valuable comments that improved the presentation and contents of this dissertation.

I would like to thank Dr. Abraham Munitz for his kindness and help in putting together our Electromagnetic Levitation system parts and performing early experiments in our lab at University of California, Riverside.

My gratitude is also extended to Professor Sakhrat Khizroev and his colleagues Dr. Nissim Amos and Dr. Jeongmin Hong at the Center for 3D Electronics within the Department of Electrical Engineering for helping me with magnetic characterization experiments and VSM measurements.

I am truly thankful to all my friends, colleagues and staff in the Department of Mechanical Engineering at UC Riverside specially Shaahin Amini, Melina Roshandell, Jun Wang, Roseanna Baron-Lopez, Terry Traver, Katie Dell, Paul Talavera, Sarah Nosce, Jennifer Morgan, and Becki Jo Ray and Eilene Montoya in the Dean's office for their unconditional help and support during these years.

None of this would have been possible without the endless love and patience of my family. I am really indebted and deeply thankful to my parents, Mohammad Amir and Nezhat for their faith in me and allowing me to be as ambitious as I wanted. It was under their watchful eye that I gained so much drive and an ability to tackle challenges head on. My sisters Leila and Zahra have been a constant source of love, concern, support and strength all these years. I would like also to express my heart-felt gratitude to my all extended-family members.

And last, but not the least, I warmly appreciate the generosity and understanding of my lovely wife, Fatemeh, who supported me spiritually from the first day of our common life and never left me alone with this journey until the last day.

Haamun Kalaantari
Riverside
March 2013

To my all wonderful teachers who believe in diligence, science and pursuit of academic excellence. Particularly, to my very first teachers, my mom Nezhat and my dad Mohammad Amir

ABSTRACT OF THE DISSERTATION

Development of Co-Ni-Ga Ferromagnetic Shape Memory Alloys (FSMAs) by Investigating the Effects of Solidification Processing Parameters

by

Haamun Kalaantari

Doctor of Philosophy, Graduate Program in Mechanical Engineering
University of California, Riverside, March 2013
Professor Reza Abbaschian, Chairperson

Among Ferromagnetic Shape Memory Alloys (FSMAs), Co-Ni-Ga ternary alloys have attracted great attention due to their high Curie and martensitic transformation temperatures as well as improved ductility. Single β phase undergoes the martensitic transformation in this system, which is the base of ferromagnetic shape memory effect. In this investigation, Electromagnetic Levitation (EML) technique was employed to assess the effect of bulk supercooling and rapid solidification on near *Heusler-type* dual phase $Co_{46}Ni_{27}Ga_{27}$ and single phase $Co_{48}Ni_{22}Ga_{30}$ (at%) compositions. The effects of γ+β microstructure on the martensitic and austenitic transformation temperatures and magnetic properties were also investigated. The presence of γ phase was found to suppress the martensitic and austenitic transformations to below room temperature. Bulk supercooling and rapid solidification led to the formation of homogeneous single martensitic phase from hyperperitectic alloy, which under normal solidification form the dual $\gamma+\beta$ phases. Moreover, in contrast with martensite forming from $Co_{48}Ni_{22}Ga_{30}$, the hyperperitectic martensite in supercooled $Co_{46}Ni_{27}Ga_{27}$ samples showed no grain boundary microsegregation. The martensite also showed a high Curie temperature about 127°C and good directional magnetic properties, including different in- and out-of-plane magnetization up to saturation level, and different coercivity from around 14 Oe for in-plane direction to about 42 Oe at the 50° angle. The role of solidification variables and chemical composition in the microstructure, and phase transformation in the ternary alloys $Co_{50}Ni_{50-x}Ga_x$ (at%) with x ranging up to 50, and $Co_{100-2y}Ni_yGa_y$(at%) with y ranging from 15 to 35 were studied as well. For the metastable single β phase of supercooled $Co_{50}Ni_{22.5}Ga_{27.5}$ alloy in $Co_{50}Ni_{50-x}Ga_x$ series, the martensitic transformation showed thermal stability during cyclic cooling and heating (up to 350°C) revealing its potential as a FSMA candidate. In $Co_{100-2y}Ni_yGa_y$ series, on the other hand, paramagnetic $Co_{40}Ni_{30}Ga_{30}$ alloy showed martensite to austenite transformation temperature higher than 470°C, indicating its potential as High Temperature Shape Memory Alloy (HTSMA).

Contents

1. Literature Review 1

1.1. Introduction to Ferromagnetic Shape Memory Alloys (FSMAs) 2

1.1.1. Martensitic Transformation and Twining 2

1.1.2. Martensite Crystallography 6

1.1.3. Shape Memory Phenomenon 11

1.1.4. Twin Variants Boundary Motion Mechanism 17

1.1.5. Transformation Thermodynamics 21

1.1.6. Co-Ni-Ga and Co-Ni-Al FSMAs 24

1.1.7. Phase Transformations in FSMAs 26

1.1.8. Magnetic Properties in FSMA 34

1.2. Solidification Process 52

1.2.1. Rapid Solidification (RS) 55

1.2.2. Midrib Curve (T_0) and Partitionless Solidification 59

1.2.3. Interfacial versus Bulk Supercooling 61

1.2.4. Electromagnetic Levitation Melting for a Containerless Processing 66

1.3. Co-Ni-Ga Ternary System 72

1.3.1. Crystal Structures of Co-Ni-Ga 72

1.3.2. Solidification and Microstructure of Co-Ni-Ga 77

1.4. Characterization of FSMAs 80

1.4.1. Vibrating Sample Magnetometer (VSM) Systems for Magnetic Characterization ……………………………………………...……………………………………..…..80

1.4.2. Differential Scanning Calorimeter (DSC) and Thermo-Magnetization Curves 84

1.5. Summary 84

2. Technical Approach 86

2.1. Specimen Preparation 87

2.2. Electromagnetic Levitation (EML) 87

2.3. Induction Melting 90

2.4. Experimental Procedure 91

2.5. Specimen Characterization 92

2.6. Thermal Information 93

3. Results and Discussion 96

3.1. Effects of Bulk Supercooling and Rapid Solidification on Near *Heusler* Co-Ni-Ga FSMAs 97

3.1.1. Microstructures 97

3.1.2. Metastable Phase Formation in Supercooled and Rapid Solidified Samples 102

3.1.3. Martensitic Transformation 104

3.2. Magnetic Properties 108

3.2.1. Magnetization Hysteresis Loops 108

3.2.2. Magnetization Saturation 114

3.2.3. Coercivity 115

3.3. Solidification and Microstructural Evolution of Co-Ni-Ga Alloys 116

3.3.1 Investigation of Solidification Parameters and Microstructure of $Co_{50}Ni_{50-x}Ga_x$ (at%) Alloys 116

3.4. Solidification Parameters and Microstructure of $Co_{100-2y}Ni_yGa_y$ (at%) Alloys 133

3.4.1. Martensitic Transformation in $Co_{50}Ni_{50-x}Ga_x$ (at%) Alloys 138

3.5. Summary 148

4. Conclusions 151

5. References 156

List of Tables

Table 1. Summary of the amount of MFIS, structure of the parent and martensitic phase, transformation temperature (T_M) and ductility (in relation to Ni-Mn-Ga) of different alloys [55].25

Table 2. Available techniques for obtaining bulk supercooling in liquid metals and alloys 65

Table 3. Nominal composition and condition of alloys in this study 98

Table 4. Nominal composition and solidification condition of alloys in $Co_{50}Ni_{50-x}Ga_x$ (at%) series 118

Table 5. Nominal composition and condition of alloys in $Co_{100-2y}Ni_yGa_y$ (at%) series 134

Table 6. Results for $Co_{100-2y}Ni_yGa_y$ (at%) with y ranging from15 to 35 and near *Heusler-type* $Co_{46}Ni_{27}Ga_{27}$ and $Co_{48}Ni_{22}Ga_{30}$ (at%) compositions 149

Table 7. Results for $Co_{50}Ni_{50-x}Ga_x$ (at%) alloys serieswith x ranging up to 50 150

List of Figures

Fig. 1. Schematics in 2D of the cubic-to-tetragonal martensitic transformation (a) Two different tetragonal twin variants (martensite-M) originate from cubic austenite (A), (b) twinned microstructure formed from two twin variants connected by one twin boundary, and (c) 3D sample containing two martensitic twin variants [30]. 5

Fig. 2. (a) and (b) illustrate how a martensite plate remains (macroscopically) coherent with the surrounding austenite and even the surface it intersects; (c) Schematic representation of the invariant-plane strain shape deformation characteristic of a MT. The initial straight scratch DE is displaced to the position DF when the martensite plane ABC is formed. The plane ABC is invariant (undistorted and unrotated as a result of the MT) [32]. 7

Fig. 3. Bain correspondence for the γ (Austenite) → $\alpha^{'}$(Martensite) transformation. Possible interstitial sites for carbon are shown by crosses. To obtain $\alpha^{'}$ the γ unit cell is contracted about 20% on the C axis and expanded about 12% on the a axes [34]... 8

Fig. 4. (a) The effect of the Bain strain on austenite, which when undeformed is represented as a sphere of diameter wx=yz in 3D. The strain transforms it to an ellipsoid of revolution. (b) The invariant-line strain obtained by combining the Bain strain with a rigid body rotation through an angle θ [34].. 9

Fig. 5. (a) As shown for twinning (left) and slip (right), the same magnitude of the homogeneous shear, as given by the angle γ, can be accomplished by either. (b) Twins in martensite may be self-accommodating and reduce energy by having alternate regions of the austenite undergo the Bain strain along different axes [34]. 10

Fig. 6. Coil-spring example illustrating the differences between the one-way and two-way shape memories [34]. 12

Fig. 7. Electrical resistance changes during cooling and heating Fe-Ni and Au-Cd alloys, illustrating the hysteresis of the martensitic transformation on cooling, and the reverse transformation on heating (After Kaufman and Cohen) [25]. 13

Fig. 8. Mechanism of SME; (i) original parent single crystal, (ii) self-accommodated martensite, (iii)-(iv) deformation in martensite proceeds by the growth of one variant at the expanse of the other (i.e. twinning or detwinning), (v) upon heating to a temperature above A_f, each variant reverts to the parent phase in the original orientation by the reverse transformation [39]. 14

Fig. 9. Optical micrograph of self-accommodation of the R-phase (Ti-48.2Ni-1.5Fe (at%) alloy) [40]. 15

Fig. 10. (a) Ni-Mn-Ga Cubic Heusler structure in the high temperature austenitic phase and (b) tetragonal variant structure [53] 18

Fig. 11. Schematic illustration of the magnetic shape memory effect (H2 >H1) [54] 19

Fig. 12. 2D schematics of twinning (a) s is the magnitude of twin shear and its direction is parallel to the twin plane (101). (b) magnetic moments direction in the connected twin variants. The easy axis of magnetization is related to the short crystallographic axis. The rotation of magnetic moments in reality is across over the twin boundary producing a 90° magnetic domain wall [34]. 20

Fig. 13. (a) Thermoelastic Shape Memory (TSM) and (b) Ferromagnetic Shape Memory (FSM) behavior (Note:Ku: mechanical energy, MsH: magnetic energy) [57]. 23

Fig. 14. DSC curve of Co-23.5at%Ni-30at%Ga (a) and magnetization-temperature curve of Co-22.5at%Ni-30at%Ga quenched from 1200 °C (b). 28

Fig. 15. Three types of transformation behavior in shape memory alloys [12] 29

Fig. 16. The dependence of characteristic temperatures (T_c and M_s) on Co and Ni concentration [12].(a) Co-Ni-30 at% Ga (b)Co-Ni-32%at% Ga. 30

Fig. 17. Conceptual position of several alloy systems in the Martensite, Ferromagnetic and Special Lattice Relationship groups. Alloys in the overlap group of all three are FSMAs [16]....31

Fig. 18. Martensitic start (*Ms*) temperatures versus the component ratio for the investigated Co-Ni-Ga alloys [28]. 32

Fig. 19. Compositional range for the formation of Co_2NiGa FSMAs (see text for details) [28]..33

Fig. 20. The effect of the electron/atom ratio on the M_s temperature in $Co_2NiGa(Al)$ and Ni_2MnGa FSMAs. Ni_2MnGa data (■) [19]. 34

Fig. 21. Magnetization curves measured along different axes of orthorhombic seven-layered phase (the single-variant constrained state) in the$Ni_{48.8}Mn_{29.7}Ga_{21.5}$alloy at 300 K [83]. 36

Fig. 22. Temperature dependence of the magnetization of (a) as-grown and annealed crystals with stoichiometric composition of Ni_2MnGa and (b) the crystals with off-stoichiometric composition of $Ni_{52.7}Mn_{22.6}$ $Ga_{24.7}$ (at.%) at low (0.08T) and high (2T) magnetic field [95]. 37

Fig. 23. Thermomagnetization curves of the (a) $Ni_{50}Mn_{34}In_{16}$, (b)$Ni_{50}Mn_{37}Sn_{13}$ and (c) $Ni_{50}Mn_{37}Sb_{13}$ alloys measured by VSM [96] 38

Fig. 24. Temperature dependencies of low-field magnetic susceptibility (χ) of (a) $Ni_{2+x}Mn_{1-x}$ Ga alloys [26] and (b) $Ni_{48.8}Mn_{29.7}Ga_{21.5}$ alloy. Arrows mark phase transformations. *C*: ferromagnetic cubic phase, Or: orthorhombic seven-layered phase, *T*: tetragonal non-modulated phase.......... 40

Fig. 25. Magnetization curves of $Co_2Ni_{0.88}Ga_{1.12}$ determined at room temperature. ▼for as-solidified sample, □ for 3 hours annealed at 850°C and quenched. 41

Fig. 26. Magnetic properties of the $Co_{52.1}Ni_{26.1}Ga_{21.8}$ ribbon. (a) Temperature dependence of the magnetization in an external magnetic field of 40 kAm^{-1}. (b) Magnetic hysteresis loops at 293K (martensite phase) and 373K (austenite phase) upon heating [97]. 42

Fig. 27. (a) Direction dependence of magnetization of the $Co_{52.4}Ni_{22}Ga_{25.6}$ ribbon sample, and (b) schematic diagram of measurement directions 43

Fig. 28. Magnetic properties of Co-18 at% Ni-30at% Ga FSMAs. (a) M-T curve in an external magnetic field 0.04 MAm $^{-1}$ on heating (b) M-H curves at 84 K and 223 K............................... 44

Fig. 29. (a) Magnetization dependence of the magnetic field for the$Co_{50}Ni_{20}Ga_{30}$ ribbon at various temperatures; (b) temperature dependence of magnetizations for the $Co_{50}Ni_{20}Ga_{30}$ ribbon under a field of 50 kOe. Inset graph shows the ribbon data for T<100K as a function of $T^{3/2}$ [101]. 45

Fig. 30. (a) Direction dependence of coercive force of the bulk and ribbon samples, (b) temperature dependence of coercive force of the three ribbons. 46

Fig. 31. Magnetic field induced strain in Ni-Mn-Ga FSMAs (a) in different crystallographic directions, (b) and (c) their corresponding strains [1]. 47

Fig. 32.Variants observed by optical microscope on the (010) surface of $Co_{50}Ni_{22}Ga_{28}$single crystal sample cooled from parent phase in zero field (a) and in a bias field of 0.3 T (b)............ 49

Fig. 33. $Co_{52.4}Ni_{22}Ga_{25.6}$ directional manetostriction measurement at room temperature of (a) ribbon sample, (b) bulk samples and (c) schematic of magnetostriction measurement method [82, 101] 50

Fig. 34. $Co_{50}Ni_{20}Ga_{30}$ directional manetostriction measurement at 200K.................................. 51

Fig. 35. Magnetostriction strain (ε) vs. temperature curves for the $Co_{52.4}Ni_{22}Ga_{25.6}$ ribbon.......... 52

Fig. 36. A solute boundary layer of thickness, $\delta_{o,i}$ [108]. 53

Fig. 37.Velocity-dependent partitioning coefficient predicted by Aziz's and Abbaschian's models [115] 59

Fig. 38. A schematic demonstrates the mechanism of solute trapping [119] 60

Fig. 39. The free energy-tempearture (G-T) curves at a constant composition demonstrate possible phase transformations of supercooled liquid.. 61

Fig. 40. A coaxial levitation coil first used for containerless processing of metals [126] (a) the solid sphere, and (b) the sphere in a molten state 67

Fig. 41. A series of pictures demonstrate levitation and melting process of a specimen in EML system. 67

Fig. 42. Microstructure of Fe-10Cr alloy solidified at different undercoolings. (a) ΔT= 125 K, dendritic microstructure; (b) *ΔT*= 200 K, cellular microstructure; (c) *ΔT*= 230 K, cellular microstructure; (d) *ΔT*= 315 K microsegregation-free microstructure [133]. 70

Fig. 43. Cross-sectional SEM micrograph of as-solidified Ni 84 Nb 16 samples for different undercooling levels prior to solidification and post-solidification cooling, respectively: (a) ΔT ‹ 70 K, quenched on a Cu substrate (bottom): metastable α-Ni dendrites (dark); (b) ΔT ‹ 70 K, central part of the sample quenched on a Cu substrate: dendritic microstructure along with lamellar eutectic [α-Ni (dark) +Ni 3 Nb (bright)] cells in interdendritic regions; (c) ΔT ‹ 160 K, gas cooled: anomalous eutectic α-Ni+Ni 3 Nb microstructure; (d) ΔT ‹ 240 K, quenched on a Sn-coated substrate: Ni Nb phase layer (bright) near the chill substrate interface (bottom) succeeded by a weakly segregated twinned α-Ni microstructure (greyish) [134]. 71

Fig. 44. TEM micrographs of (a) Ti-1.4Er (b) Ti-1.7Ce and (c) Ti-1.5La undercooled about 200 K before splat quenching [135] 71

Fig. 45. (a) BCC in FCC structure [59] (b) cF4 (FCC structure) [138] (c) cP2 (BCC structure) [138] 72

Fig. 46. The bcc parent phase undergoes to the fct martensite based on Bain model [137] 73

Fig. 47. (a) A *β*-phase region and two-phase area in Co-Ni-Ga ternary system at room temperature projected from binary diagrams [137-139]. 74

Fig. 48. The Ga-Co-Ni phase diagram for the martensitic phase at room temperature with the isothermal room-temperature martensite start temperature *Ms* (T_R) represented in the isothermal section of 1000°C [141]. 76

Fig. 49. The Co_2NiGa cubic crystal structure $L2_1$ with four interpenetrating face-centered cubic sub-lattices [141]. 77

Fig. 50. Three possible solidification routes; toward (1) Ga-rich, (2) Ni-rich and or (3) Co-rich regimes for Co-Ni-Ga alloys with compositions in the β-phase region. 78

Fig. 51. Precipitation of γ-phase in β'-matrix (a) results in improved ductility in Co-Ni-Ga FSMAs [12] (b). 80

Fig. 52. The parameters in hysteresis loop that characterize the magnetic properties of FSMA [144] 81

Fig. 53. Direction dependence of magnetization at room temperature in Co2Ni0.85Ga1.15 bulk and as-spun ribbon samples. The coordinates l, t and w denote the longitudinal, thickness and width directions, respectively [18, 58]. 83

Fig. 54. Relation between coercive force and direction of as spun Co-Ni-Ga ribbons. Open and closed symbols denote data taken from ribbon and bulk samples, respectively. All data were observed at 8 KOe and 293K (room temperature) [18, 58]. 83

Fig. 55. An arc-melting furnace for specimen preparation 87

Fig. 56. The levitation station; A) high-power supplying units, B) step transformer, C) data acquisition system and D) electromagnetic levitation coil set up and Cu-chill. 88

Fig. 57. The details of the electromagnetic levitation apparatus used for containerless melting processes; A) levitation coil, B) quartz glass, C) processing gas inlet (He and Ar/Ar+5%H_2), D) specimen positioning mechanism and protective gas outlet [148] 89

Fig. 58. The slope Cu-chill 90

Fig. 59. The configuration of the induction melting process [149] 91

Fig. 60. Time-Temperature profile of a levitated specimen (J1-$Co_{60}Ni_{20}Ga_{20}$) with bulk-supercooling and recalesence phonemenon (circled). 94

Fig. 61. (a) Normal solidification (b) Bulk supercooling prior to solidification [119] 95

Fig. 62. (a) Microstructures of a $Co_{48}Ni_{22}Ga_{30}$ (at%) sample quenchedfromsuperheated melt. The grain boundaries contain cobalt-rich phase. (b) SEM micrograph (sample D1) shows severe grain boundaries embrittlement that caused detached grains and one fallen off grain. 99

Fig. 63. (a) Dendritic microstructure of primary γ phase of $Co_{46}Ni_{27}Ga_{27}$ (at%) sample quenched from the superheated melt. (b) BSE micrograph (sample C2); martensite matrix has been shown. 99

Fig. 64. (a) A pseudo binary diagram for Co-Ni-Ga alloys containing 47 at% Co [137, 152]. The metastable extension of the liquidus and solidus lines and T_0 line for the β phase are also shown. The dashed arrow shows the composition of the supercooled sample as described in the text. (b) The interface velocity effect on the solute distribution at the moving S/L interface. 100

Fig. 65. Microstructure of $Co_{46}Ni_{27}Ga_{27}$ (at%) sample slowly cooled during levitation (sample C6), consisting of fragmented dendrites and interdendritic martensite matrix......................... 101

Fig. 66. Microstructure of $Co_{46}Ni_{27}Ga_{27}$ (at%) sample solidified with ΔT= 143°C supercooling (sample C11). (a) The lower portion (zone I), solidified near the chill surface, consists of non-equilibrium, off-composition, martensite. The upper portion (zone II) contains primary γ dendrite and interdendritic β' (martensitic β). (b) Shows a higher magnification of interface between two different zones. 102

Fig. 67. DSC graphs of four heating/cooling cycles for $Co_{48}Ni_{22}Ga_{30}$ (at%) sample quenched from the superheated melt (sample D1) with cooling/heating rates: (a) 10ºC/min and (b) 1ºC/min.... 105

Fig. 68. DSC graphs of four heating/cooling cycles with 10ºC/minheating/cooling rate of $Co_{46}Ni_{27}Ga_{27}$ (at%) samples (a) C2 , (b) C6 and (c) C11 (with ΔT= 143ºC supercooling). 107

Fig. 69. Magnetic properties of $Co_{48}Ni_{22}Ga_{30}$ (at%) alloy quenchedfromthesuperheated melt (D1sample), the inserted graphs at low scale (500 Oe and 20 emu/g) also show coercive forces (a) in-plane (θ= 0º) (b) out-of-plane (θ= 90º). 109

Fig. 70. Magnetic properties of $Co_{46}Ni_{27}Ga_{27}$ (at%) alloy quenchedfromthesuperheated melt (C2 sample), the inserted graphs at low scale (500 Oe and 20 emu/g) also show coercive forces (a) in-plane (θ= 0º) (b) out-of-plane (θ= 90º).. 110

Fig. 71. Magnetic properties of $Co_{46}Ni_{27}Ga_{27}$ (at%) alloys cooled during levitation (C6 sample), the inserted graphs at low scale (500 Oe and 20 emu/g) also show coercive forces (a) in-plane (θ= 0º) (b) out-of-plane (θ= 90º). 111

Fig. 72. Magnetic properties of $Co_{46}Ni_{27}Ga_{27}$ (at.%) alloys with ΔT= 143°C supercooling (C11 sample), the inserted graphs at low scale (500 Oe and 20 emu/g) also show coercive forces (a) in-plane (θ= 0º) (b) out- of-plane (θ= 90º).. 112

Fig. 73. M-H curves at room temperature of (a) $Co_{48}Ni_{22}Ga_{30}$ (at%) (D1sample) and different $Co_{46}Ni_{27}Ga_{27}$ (at%) alloy samples (b) C2, (c) C6 and (d) C11 samples. 113

Fig. 74. Magnetization saturation (Msat) in different temperatures (dashed lines are related to cooling cycles) of (a) $Co_{48}Ni_{22}Ga_{30}$ (D1sample) and different $Co_{46}Ni_{27}Ga_{27}$ (at%) alloy samples (b) C2, (c) C6 and (d) C11. 115

Fig. 75. Coercive force in different directions at room temperature for $Co_{48}Ni_{22}Ga_{30}$ (at%) (D1sample) and different $Co_{46}Ni_{27}Ga_{27}$ alloy samples (C2, C6 and C11 samples). 116

Fig. 76. Isothermal section schematic phase diagram of the Co-Ni-Ga system at 800 and 1150°C [137, 152]. The designed two composition series, the circles denote $Co_{50}Ni_{50-x}Ga_x$ and the triangles denote $Co_{100-2y}Ni_yGa_y$ have shown. The solid shapes show the alloys with the Curie temperature lower than room temperature and hallow ones represent the alloys with the Curie temperature higher than room temperature. 117

Fig. 77. Microstructures of $Co_{50}Ni_{40}Ga_{10}$ (at%) samples quenched from (a) S+L region (G1) and (b) liquidus temperature (G2). The well-developed γ dendrites in β matrix in both microstructures and forming single metastable γ phase in a very thin layer near to the Cu-chill surface in (b) have been shown. 120

Fig. 78. Microstructure of $Co_{50}Ni_{35}Ga_{15}$ (at%) sample (S) quenched from liquidus temperature. (a) The lower portion (zone 1), solidified near the chill surface, consist of metastable single γ phase. The upper portion (zone2) contains primary γ dendrite and interdenderitic β phase. (b) A higher magnification of metastable γ phase and interface between two different zones 121

Fig. 79. A pseudo binary diagram for Co-Ni-Ga alloys containing 50 at% Co. The metastable extension of the liquidus and solidus lines and T_0 lines for the γ and β phases are alos shown. The dashed arrow shows the estimated critical composition, Ga= 20 at% , for partitionless solidification and solute entrapment due to supercooling effect during RS to form metastable single γ phase (below γ-T_0) in about Ga<20 (at%) and metastable single βphase (below β-T_0) in Ga>20 (at%) as described in the text. 122

Fig. 80. Optical micrograph of $Co_{50}Ni_{32.5}Ga_{17.5}$ alloy (R) with γ phase (dendrites) and β (matrix) phases in slow cooled and solidified with Ar+He in levitation. The dark areas in the microstructure are related to the pores (see text). 123

Fig. 81. Optical micrographs of $Co_{50}Ni_{30}Ga_{20}$ (H) samples (a) β' (martensite)+ γ (dendrites) phases in quenched sample from T_L (H1) (b) two zones area in the supercooled and quecnched sample (H2), zone 1- single metastable γ phase forming on near Cu-chill region from 60°C supercooled liquid, zone 2- γ+β phase region. 124

Fig. 82. Optical micrographs of $Co_{50}Ni_{30}Ga_{20}$ (H) samples in two different thermal conditions. (a) β+γ phase micorstructure with well dvloped primary γ denderites in dropped sample from S+L

(H3) (b) Two zones, zone 1- single metastable γ phase forming on Cu-chill from 45°C supercooled liquid, zone 2- β+ γ phase region (H4).. 125

Fig. 83. Microstructure of $Co_{50}Ni_{27.5}Ga_{22.5}$ (P) alloy quenched from about T_L has shown here in different distance from Cu-chill (manifesting different cooling rates). (a) fine lamellar β+γ phase micorstructure (with primary γ denderites) near to Cu-chill (faster cooling rate). (b) coarse β+γ phase region near to the sample surface (slower cooling rate). 126

Fig. 84. Optical micrographs of $Co_{50}Ni_{25}Ga_{25}$(A1) alloy quenched from about $T_L$at different distances from Cu-chill (manifesting different cooling rates)(a) The lower portion solidified near the chill surface, consists of single β parent phase matrix with the precipitates of the secondory γ phase. The upper portion contains primary γ denderites and interdendritic β phase (b) A higher magnification of interface between two different regions (c) Fine equiaxed γ grains and β'(marrtensitic β) matrix near to the top of two-region interface (d) Primary dendrite γ phase embeded in β'(marrtensitic β) matrix in well farther part from Cu-chill. 127

Fig. 85. Dendritic microstructure of primary γ phase and interdendritic β matrix of $Co_{50}Ni_{25}Ga_{25}$ alloy dropped from $S+L$ (A2). 128

Fig. 86. Optical micrographs of $Co_{50}Ni_{25}Ga_{25}$ (A3) alloy solidified near the chill with ΔT= 76°C supercooling, single metastable β phase forming on the surface of Cu-chill from supercooled liquid. 129

Fig. 87. Metastable single β phase formation in ΔT=147°C supercooled $Co_{50}Ni_{22.5}Ga_{27.5}$ (O) sample. This supercooled $Co_{50}Ni_{22.5}Ga_{27.5}$ sample has a single β phase. (a) Two zones (b) single metastable β phase (near to the Cu-chill) and (c) β (matrix) +γ (dendrite) phases (farther to the Cu-chill). 131

Fig. 88. Single β phase formation through the entire cross section of $Co_{50}Ni_{20}Ga_{30}$ samples (E). (a) Quenched directly from T_L (E1) and (b) with ΔT= 54°C degree of supercooling before

quenching (E2). The supercooled sample has the martensitic microstructure (β' phase) at room temperature. 132

Fig. 89. Microstructure of $Co_{50}Ni_{10}Ga_{40}$ sample with ΔT= 26°C supercooling quenched on the Cu-chill (F1). Single β phase with sever intergranular cracking through the entire cross section of sample are shown. 133

Fig. 90. Optical micrographs of $Co_{70}Ni_{15}Ga_{15}$ alloy (I) quenched from T_L(a) fine lamellar β (matrix)+ γ (dendrites) phases in micorstructure near to the Cu-chill (faster cooling rate). (b) coarse β+ γ phase region near to the sample surface (slower cooling rate). 135

Fig. 91. Optical micrographs of $Co_{60}Ni_{20}Ga_{20}$ alloy (J) quenched from above T_L. (a) The lower portion (zone 1), solidified near the chill surface, consists of a single γ phase. The upper portion (zone 2) contains primary γ dendrite and interdenderitic β phase. (b) A higher magnification of fine lamellar β (matrix)+ γ (dendrites) phases in micorstructure fartehr from the Cu-chill (slower cooling rate). 135

Fig. 92. Optical micrographs of $Co_{40}Ni_{30}Ga_{30}$ alloy (K) quenched from T_L. (a) Developed a brittle martensitic microstructure (single β' phase) through the entire of the cross section. (b) A higher magnification of martensitic micorstructure 136

Fig. 93. Optical micrographs of $Co_{30}Ni_{35}Ga_{35}$ alloy (L) sample dropped from about T_L, (a) martenstic microstructure (β') for contact surface with Cu-chill (b) β' (martensic phase) and dark intergranular Ga-rich(Ga_2NiCo) phase (farther to the Cu-chill) (c) SEM micrograph in higher magnification for intergranular Ga-rich (Ga_2NiCo) brittle phase in (b). 138

Fig. 94. DSC graphs of four heating/cooling cycles for (a) $Co_{50}Ni_{35}Ga_{15}$ (at%) sample quenched from the liquidus temperature (sample S) and (b) $Co_{50}N_{30}Ga_{20}$ (at%) sample quenched with ΔT= 45°C supercooling (sample H4) 140

Fig. 95. DSC graphs of four heating/cooling cycles for $Co_{50}Ni_{22.5}Ga_{27.5}$ (at%) with ΔT= 147°C supercooling (sample O). 141

Fig. 96. DSC graphs of (a) single heating/cooling cycle for $Co_{50}Ni_{20}Ga_{30}$ (at%) sample quenched from the liquidus temperature (sample E1), (b) single heating/cooling cycle for $Co_{50}Ni_{20}Ga_{30}$ (at%) sample with ΔT= 45°C supercooling (sample E2), (c) fourheating/cooling cycles for sample E1 and (d) four heating/cooling cycles for sample E2. 144

Fig. 97. DSC graphs of four heating/cooling cycles for $Co_{70}Ni_{15}Ga_{15}$ (at%) sample quenched from the liquidus temperature (sample I). 145

Fig. 98. DSC graphs of (a) single heating/cooling cycle with 10°C/m rate for $Co_{40}Ni_{30}Ga_{30}$ (at%) sample quenched from the liquidus temperature (sample K) and (b) three heating/cooling cycles with 20°C/m rate for sample K. 147

Chapter I

Literature Review

1.1. Introduction to Ferromagnetic Shape Memory Alloys (FSMAs)

In 1996, a new class of smart materials called Ferromagnetic Shape Memory Alloys (FSMAs) in a Ni-Mn-Ga ternary system was discovered [1]. This type of materials with a *Heusler-type* composition exhibits both ferromagnetic and shape memory behavior. Under the applied magnetic field, a large reversible strain up to 10% in a particular crystallographic direction can be observed. This strain was attributed to the motion of the martensitic twins, which is different from the conventional (magnetoelastic) magnetostriction [2, 3]. The discovery of this type of materials has brought much interest in Mechanical Engineering, Physics and Materials Science and Engineering aspects of the alloys. These materials are promising candidates for biomedical devices, Micro-Electro-Mechanical-System (MEMS) [4] and aerospace applications [5], particularly as sensing and actuating devices [6, 7, 8]. There are a few alloys including Fe-Pd [9], Fe-Pt [10], Ni-Mn-Ga [1-3, 11-13], Co-Ni-Al [14-17], and Co-Ni-Ga [14, 18-20] exhibiting such Ferromagnetic Shape Memory (FSM) behavior.

1.1.1. Martensitic Transformation and Twining

Martensitic Transformation (MT) is a subset of the displacive transformations. Precisely, it is defined as shear-dominant, lattice-distortive, diffusionless transformation [21].

In most cases, MT is a term extensively applied in metal physics to describe any diffusionless transformation in which from beginning to completion of the transformation, each individual atomic movement is less than one interatomic spacing. Its technological significance was first realized through the determination of the microstructure of hardened steel in the late 19th century. If the steel is quenched rapidly enough from the austenite phase, there is insufficient time for the eutectoid diffusion-controlled decomposition transformation to occur, and the steel transforms to martensite, which is simply a supersaturated solid solution of carbon in α-Fe (γ→ α') [22]. Therefore, the average chemical composition of martensite is identical to that of the parent austenite. It has been indicated that a fully grown plate spanning a whole grain may form within ~10^{-7} s. As plates are formed, they immediately grow to their full size with a speed of sound [23]. The rapid nucleation and growth of martensite cause an independent thermal character of the MT. In the vast majority of cases, the extent of reaction is found to be virtually independent of time [24]:

$$1-V_{\alpha'}=\exp[\beta-(M_S-T)] \qquad \text{Eq. 1}$$

$V_{\alpha'}$ is the fraction of martensite, and T is a temperature below M_S, the temperature martensitic transformation starts. This equation is called Koistinen and Marburger equation [24]. It should be noted that time does not enter in this relation, so that the fraction of martensite depends only on the undercooling below the martensite-start temperature. In hardened steels, the martensitic phase is not a kinetically equilibrium state, and cannot be found in the Fe-C phase diagram.

Martensite is also known to form at very low temperatures, where diffusion, even through interstitial atoms, is not significant. These observations strongly confirm that martensitic transformations are diffusionless. The martensitic transformations involve a characteristic of reverse transformations, which are absent in deformation by slip or twinning.

It has been known that the materials with the ability to return to their previously defined shape or size when subjected to appropriate thermal procedure are termed as Thermoelastic Shape Memory Alloys (TSMAs). Typically, the microstructure of TSMAs is composed of a martensitic phase (M) resulting from the diffusionless transformation of a parent phase (P) [25]. The deformation in this type of material can take place in a certain crystallographic relationship between the parent and martensitic phases, which is energetically favorable [25].

As mentioned earlier, a martensitic transformation is a structural phase transformation of the diffusionless and cooperative type, where the rearrangement of atoms occurs with relatively small displacements compared to interatomic distances. There is a rigorous crystallographic connection between the lattices of the initial and final phases. The transformation is of the first order. The martensitic transformation is called thermoelastic, when it is thermally reversible.

During martensitic transformation, the high-temperature phase (usually with high symmetry, e.g. cubic) transforms to the low-temperature phase (usually with lower symmetry, e.g. tetragonal). As it is a first-order structural phase transformation, the high-temperature phase and the low-temperature martensitic phases coexist in a specific temperature range. This is due to the elastic strains that accompany the nucleation and growth of the martensitic or parent phase. The parent-martensite phase boundaries are fully or partially coherent. The elastic strains due to the martensitic transformation increase with increasing martensite fraction. To compensate the transformation strains, different crystallographic domains (twin variants) are formed within the martensite [26-29], which are often visible as parallel bands on the sample surface under microscope.

The simplest martensitic transformation is from the cubic austenite to the tetragonal martensitic phase. It results in three martensitic twin variants with different c-axis orientation. The volume of the Bravais cell is (nearly) conserved. The transformation strain is described by transformation matrices which depend on lattice constants [28]. They have only diagonal components proportional to a/a_0 and c/a_0. Here a and c are the lattice constants of the tetragonal martensite and a_0 is the lattice constant of the cubic austenite, respectively.

A martensitic transformation in two dimensions is schematically depicted in Fig. 1. The tetragonal distortions of the cubic lattice occur with the same probability along each of the crystallographic equivalent axes <100>, if there are no additional constraints favoring a single orientation. Therefore, equal amounts of these three differently oriented twin variants appear in the sample, and are connected by twin boundaries.

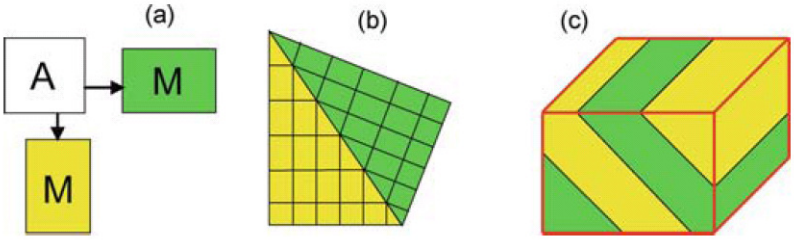

Fig. 1. Schematics in 2D of the cubic-to-tetragonal martensitic transformation (a) Two different tetragonal twin variants (martensite-M) originate from cubic austenite (A), (b) twinned microstructure formed from two twin variants connected by one twin boundary, and (c) 3D sample containing two martensitic twin variants [30].

1.1.2. Martensite Crystallography

Since the formation of martensite cannot rely on assistance by thermal activation, there must exist a high level of continuity across the interface, which should be coherent or semi-coherent. Observations have shown that the transformed regions appear relatively coherent with the surrounding austenite. This means that intersection of the lenses with the surface of the specimen does not result in any discontinuity. Therefore, lines on a polished surface are displaced, as illustrated in Fig. 2, but remain continuous after the transformation. In fact, in comparison between a perfectly coherent interface and a semi-coherent interface, there is an array of parallel dislocations in semi-coherent interface, which compensate the lattice mismatch accommodation between the austenite matrix and the martensite nucleus [31].

Assuming that a twinning shear occurs parallel to the habit (twinning) plane plus a simple uniaxial tensile dilation perpendicular to the habit plane, as shown in Fig. 2, the habit plane, which is common to both the austenite and martensite, will be macroscopically undistorted, i.e. all directions and angular separations in the plane are unchanged during transformation. Hence, the shape deformation accompanying a MT can be characterized by the Invariant Plane Strain (IPS), by which the positions or magnitude of vectors lying in the habit plane will not be altered. In an IPS, the strain experienced by any point in the lattice has a common direction and its magnitude is proportional to its distance from a fixed plane, which is not distorted by the strain.

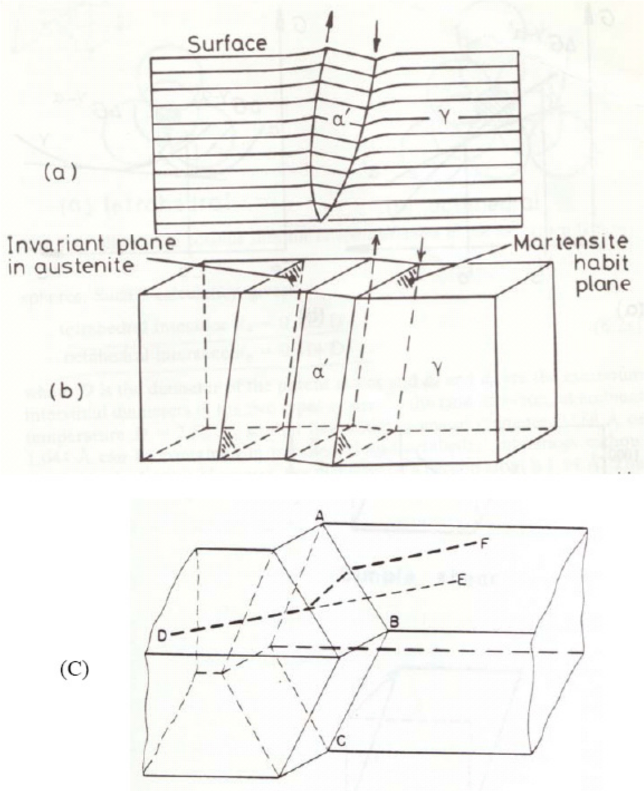

Fig. 2. (a) and (b) illustrate how a martensite plate remains (macroscopically) coherent with the surrounding austenite and even the surface it intersects; (c) Schematic representation of the invariant-plane strain shape deformation characteristic of a MT. The initial straight scratch DE is displaced to the position DF when the martensite plane ABC is formed. The plane ABC is invariant (undistorted and unrotated as a result of the MT) [32].

To illustrate the martensite crystallography, Bain was first to propose a lattice distortion with the minimum of atomic movement and the minimum of strain in the parent lattice, demonstrating how the bct lattice could be obtained from the fcc structure [33]. Based on this model and using the convention of x, y, z and x', y', z' representing the original and final axes of the fcc and bcc unit cell as plotted in Fig. 3, an elongated unit cell of the bcc structure can be drawn within two fcc cells. Transformation to a bcc unit cell is achieved by a 20% compression along the z axis and a 12% uniform expansion along the x and y axes. Fig. 3 indicates that the Bain deformation results in the following correspondence of crystal planes and directions between the parent and the product phase:

$$(111)_{\gamma} // (011)_{\alpha'} [001]_{\gamma} // [001]_{\alpha'} [110]_{\gamma} // [100]_{\alpha'} [1\bar{1}0]_{\gamma} // [010]_{\alpha'}$$

But in fact, the experimental observed orientation relationships are irrational. The relative directions can vary between $<101>_{\gamma}$ // $<111>_{\alpha'}$ (the Kurdjumov-Sachs relation) and $<110>_{\gamma}$ // $<101>_{\alpha'}$ (the Nishiyama-Wasserman relation), and these two orientation differ by ~5° about $[111]_{\gamma}$.

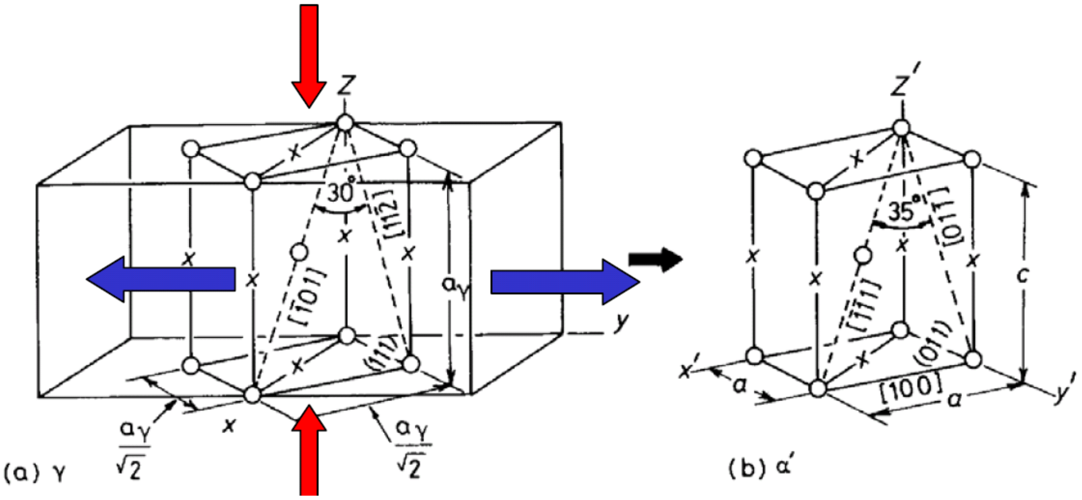

Fig. 3. Bain correspondence for the γ (Austenite) → α′(Martensite) transformation. Possible interstitial sites for carbon are shown by crosses. To obtain α′ the γ unit cell is contracted about 20% on the C axis and expanded about 12% on the a axes [34].

In Fig. 4, the austenite (fcc) is represented as a sphere which, as a result of the Bain distortion, is deformed into an ellipsoid of revolution which represents the martensite (bcc). The expression of the ellipsoid is given by:

$$\frac{x'^2}{1.12^2} + \frac{y'^2}{1.12^2} + \frac{z'^2}{0.80^2} = 1 \qquad \text{Eq. 2}$$

There are no lines in the $(010)_\gamma$ plane which are undistorted. The lines, wx and yz are undistorted in their magnitudes but rotate to the new positions w'x' and y'z'. These directions constitute the initial and final cones of the unextended lengths. Any vector lying inside these cones is reduced in length by Bain deformation, and any vector lying outside these cones is extended. The combined effect of the Bain strain and the rigid body rotation (with an angle θ) is the reason why the observed irrational orientation relationship differs from that implied by the Bain strain. However, in order to find an invariant plane in the fcc structure due to transformation, it requires that the vector oa_2 (perpendicular to the paper) must also be undistorted [35].

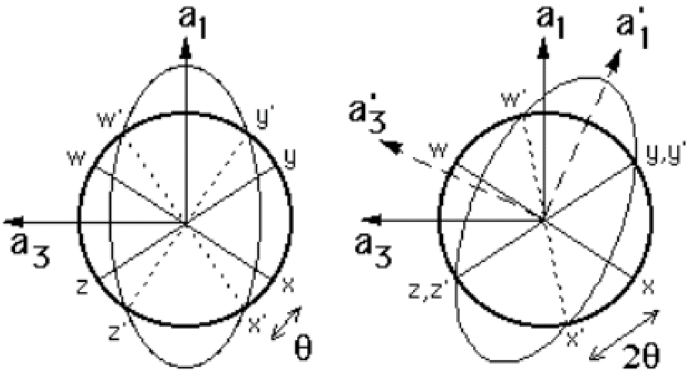

Fig. 4. (a) The effect of the Bain strain on austenite, which when undeformed is represented as a sphere of diameter wx=yz in 3D. The strain transforms it to an ellipsoid of revolution. (b) The invariant-line strain obtained by combining the Bain strain with a rigid body rotation through an angle θ [34].

Now, it is clear that the Bain deformation does not fulfill the requirements to cause a transformation with an invariant plane. Instead, the total transformation strain can be envisioned as the sum of a total of three strains: Bain, lattice-invariant distortion and a rigid body rotation, and these three components are not necessary to occur in a step-lock fashion.

From the above discussion, it can be seen that the key to the crystallographic theory of martensitic transformations is to postulate an additional distortion, which reduces the extension of oa_2 to zero. A direct consequence of this lattice invariant distortion is the manifestation of a martensite substructure in the form of slip or twins, as illustrated in Fig. 5 (a). These are called the lattice invariant shear, since neither process changes the structure of the martensite. In the case of slip, the martensite is a single crystal, though internally slipped. In the case of twinning, the lattice deformation along adjacent regions of the martensite occurs along crystallographic equivalent directions. The distortion is such that the adjacent regions fit together along a twinning plane in the martensite. The features of twinned martensite plates are demonstrated in Fig. 5 (b).

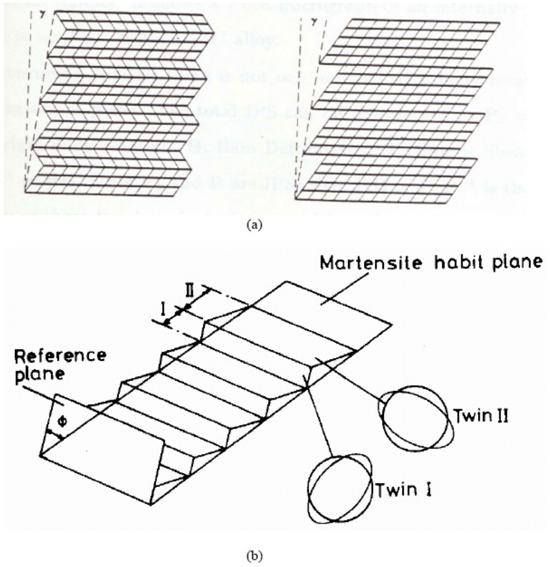

Fig. 5. (a) As shown for twinning (left) and slip (right), the same magnitude of the homogeneous shear, as given by the angle γ, can be accomplished by either. (b) Twins in martensite may be self-accommodating and reduce energy by having alternate regions of the austenite undergo the Bain strain along different axes [34].

The two adjacent contraction axes were originally 90º from each other. A vector lying in the interface, which experiences contraction in region A, would undergo expansion in region B. The final result is an overall averaged cancelled out vector with local expansions and contractions. The resulting zig-zag interface cancels the long range interfacial strain. The relative twin thicknesses depend on the value of γ, and by adjusting the width of the individual twins, the habit plane of the plate can even be made to adapt to any desired orientation.

1.1.3. Shape Memory Phenomenon

Shape Memory Alloys (SMAs) undergo a reversible martensitic transformation with relatively small temperature hysteresis. Reversibility can be assured in two ways. First, the transformation can be second order, and second, it can be of first order if the lattice constants of the parent and product structures permit the martensite to grow in the austenite without creating long-range stress fields or excess interfacial energy. Therefore, SMAs form a subgroup of all alloys undergoing a martensitic transformation. These materials have potential technical applications, and their martensitic transformations have been extensively studied in the past few decades.

The Shape Memory Effect (SME) is a unique property of certain alloys exhibiting martensitic transformations. A SMA that is deformed at a low temperature ($T< T_M$) recovers its original shape by the reverse transformation upon heating above a critical temperature. This effect was first found in an Au-47.5 at% Cd alloy by Chang and Read [36], and then it was publicized with its discovery in Ni-Ti alloys by Buehler *et al.* [37].

Historical developments of the study of SME have been reviewed by Waymen *et al.* [38]. If subsequent cooling back to the temperature of deformation does not restore the specimen to its deformed shape, this type of memory is known as the one-way SME. However, under suitable thermomechanical treatments involving the martensite and the parent phase, for example by introducing precipitation of Ti_3Ni_4 in Ni-rich Ti-Ni alloys and thereby training the material to transform back and forth to predetermined shapes, it constitutes a two-way SME [39]. Obviously, the difference between the one-way SME and two-way SME is that the latter is associated with cooling. A schematic illustration of the one-way and two-way SME has been given in Fig. 6.

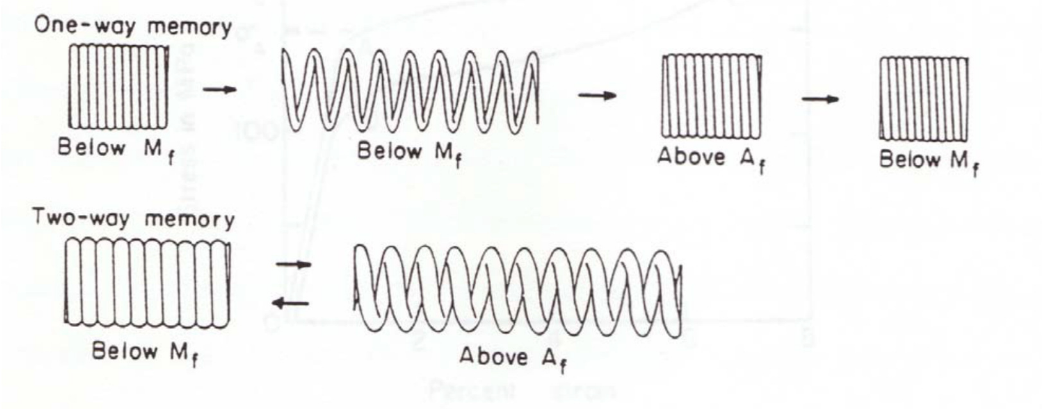

Fig. 6. Coil-spring example illustrating the differences between the one-way and two-way shape memories [34].

Considering that the martensitic transformations are associated with hysteresis, four temperatures are generally required for characterization of the reversible SME. Transformation to austenite begins at the austenite start temperature (A_s) and ends at the austenite finish temperature (A_f). Accordingly, transformation into martensite begins at the martensite start temperature (M_s) and finishes at the martensite finish temperature (M_f) shown in Fig. 7.

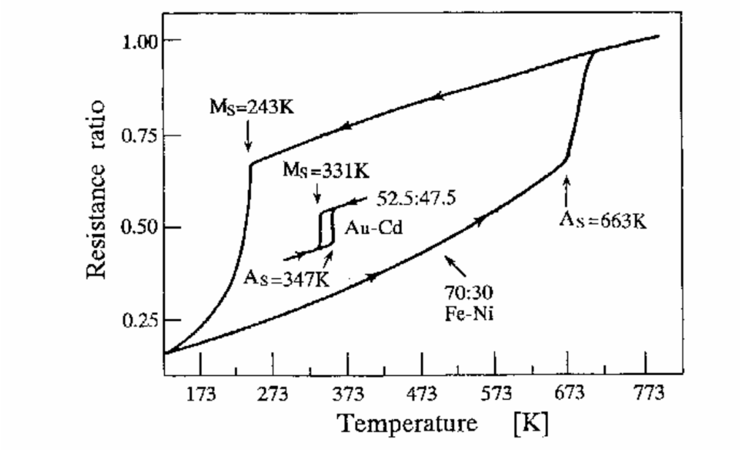

Fig. 7. Electrical resistance changes during cooling and heating Fe-Ni and Au-Cd alloys, illustrating the hysteresis of the martensitic transformation on cooling, and the reverse transformation on heating (After Kaufman and Cohen) [25].

As mentioned before, the invariant plane strain condition is necessary in reducing strains associated with the formation of a martensite plate. However, a simple shear component is still not eliminated under this condition. As shown in Fig. 5 (b) and discussed before, the martensites in region A and in region B have the same structure, but their orientations are different. They are referred to as different martensitic variants. Thus, a second step strain accommodation is necessary, and this may be possible by the combination of different martensitic variants, which is called the self-accommodation of martensites. The mechanism of SME is described by using a simplified model of a single crystal parent phase, as shown in Fig. 8.

Suppose a single crystal of austenite was cooled below M_f, at which temperature the entire sample has transformed, martensites are formed in a self-accommodation manner.

Macroscopically, this process produces no change of the shape of the specimen. However, these martensitic variants are twin related and quite mobile. Thus, if an external stress is applied, the twin boundaries move to accommodate the applied stress, and it will be transformed to a single variant state if the external stress is high enough, creating a large twinning shear strain. Unloading the sample leaves it deformed, but when the specimen is heated to a temperature above A_f, the crystallographically reversible transformation causes the sample to snap back to its original macroscopic shape. An optical microscopical image illustrating self-accommodation of martensitic variants in Fe-Ti-Ni has been shown in Fig. 9.

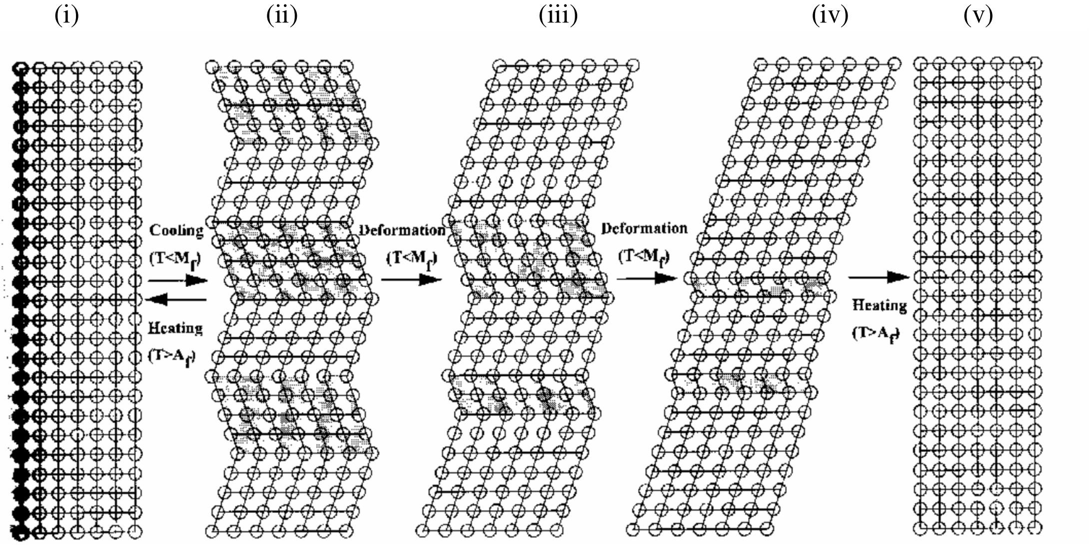

Fig. 8. Mechanism of SME; (i) original parent single crystal, (ii) self-accommodated martensite, (iii)-(iv) deformation in martensite proceeds by the growth of one variant at the expanse of the other (i.e. twinning or detwinning), (v) upon heating to a temperature above A_f, each variant reverts to the parent phase in the original orientation by the reverse transformation [39].

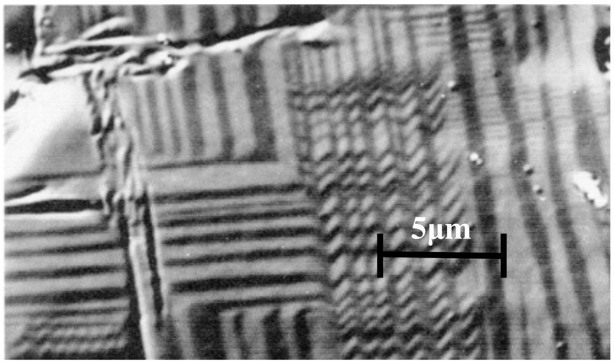

Fig. 9. Optical micrograph of self-accommodation of the R-phase (Ti-48.2Ni-1.5Fe (at%) alloy) [40].

1.1.3.1. Thermoelastic Shape Memory

Originally, thermoelastic transformation was introduced by Kurdjumov and Khandros, who observed the growth and shrinkage of a martensite plate upon cooling and heating respectively, in an Au-Cd alloy [41]. Since then, a number of thermoelastic SMAs have been extensively studied [42]. The widely used commercial alloy is Nitinol.29 NiTi which transforms from the parent phase (β) with a B2 structure to the product phase with a monoclinic B19' structure, or more often in association with the two-step transformation, from the β to a trigonal phase (so called R-phase) and to the B19' phase on cooling [30,31,32,33-]. This transformation is reversible and effectively enables the alloy to be deformed by a shear transformation by up to 16% elongation or contraction, and without irreversible plastic deformation. In contrast to the hard martensite in steel, the martensitic phase in SMAs is pseudo-elastically soft due to twin motion. Thus, the SMAs can be deformed below M_s easily, and recover their original forms by re-heating to above the M_s. These unique properties are used in such applications as medical devices, self-expanding endovascular stent [43], sensing devices [5, 6] and self-erecting space antenna.

The transformation in NiTi is interesting for two reasons; first, it involves a diffusionless transformation from one ordered structure to another. Fundamentally, if the austenitic phase is ordered, the martensitic phase must also be ordered. Secondly, the mode of the transformation is such that very extensive deformation (up to 16%) can occur by a thermoelastic martensitic shear mechanism, i.e. the transformation is reversible. Another interesting feature of this transformation is that it appears to cause an abrupt change of the apparent Young's modulus and yield strength. This change in Young's modulus also leads to distinct changes in the modulus of resilience, the "damping" properties of the material being much greater in the NiTi martensite [44].

1.1.3.2. Ferromagnetic Shape Memory

In spite of the large strain achieved, the activation of the thermoelastic SME is slow and inefficient because it depends on the transportation of heat to or from the sample. There is a type of shape memory alloys, which in their martensitic phase can produce a stress or strain in response to an applied magnetic field. In principle, the application of a magnetic field enables the devices to operate at high frequencies, and facilitates their remote control as well. However, the strength of the field required may be prohibitively large for practical applications [45]. Instead, a magnetic field can be very effective in changing the twin structure, and hence the sample shape, if the uniaxial easy direction of magnetization changes across the twin boundary, and the anisotropy energy is large. Subsequently, a new form of Magnetic-Field-Induced Strain has been observed in certain SMAs within their ferromagnetic martensitic phase, and these alloys that display MFIS are called Ferromagnetic Shape Memory Alloys (FSMAs) [7]. FSMAs distinguish themselves from the TSMAs by the fact that the magnetic field induced shape change occurs fully within the low-temperature martensitic phase.

1.1.4. Twin Variants Boundary Motion Mechanism

The FSM effect is associated with the motion of twin boundaries between regions in which the magnetization direction differs. It necessitates large magnetocrystalline anisotropy. Therefore, the field-induced strain in FSMAs arises from a mechanism different from that responsible for magnetostrictive materials, i.e. the rotation of the magnetization direction having appreciable spin-orbit coupling. The strains produced by these materials are much greater than those from magnetostrictors, and can be as large as 10% in orthorhombic Ni-Mn-Ga [46].

Apart from the practical interests, these materials also offer an excellent opportunity to investigate the various aspects of phase transformations and microstructural formation because magnetic and structural phase transformations can be realized in a single system. In Ni-Mn-Ga alloy, which is one of the prototypical ferromagnetic shape memory alloys, a high temperature cubic phase of this alloy has the $L2_1$ ordered structure, also known as the *Heusler* structure. This alloy has relatively high Curie temperature (~363 K), and martensitic transformation temperature can be controlled by changing chemical composition of the alloy. Large MFISs in these alloys [47] together with other interesting effects, like the existence of a premartensitic phase transition [48] or a large magnetocaloric effect [49], has multiplied the interest on this FSMA system. For instance, very large magnetic-field-induced strains (up to 10%) can be obtained in properly treated single crystals with good repeatability at elevated frequencies (hundreds of Hz or even kHz). Therefore, applications such as rapid magnetic actuators can be pictured. Another property of these alloys that can be of interest is the possibility to have elevated martensitic transformation temperatures with relatively good reproducibility.

As in other shape memory alloys, the martensitic transformation temperatures (T_M) of these alloys (i.e. Ni-Mn-Ga) strongly depend on the composition, and their values spread in a very wide range. For Ni-Mn-Ga alloys, a clear increase of T_M with the electron-to-atom-ratio (*e*/*a*) takes place, while the Curie point (T_C) decreases very slightly [50]. The large MFIS occurs through a field-induced reorientation of the martensitic variants (Fig. 10) [47, 51].

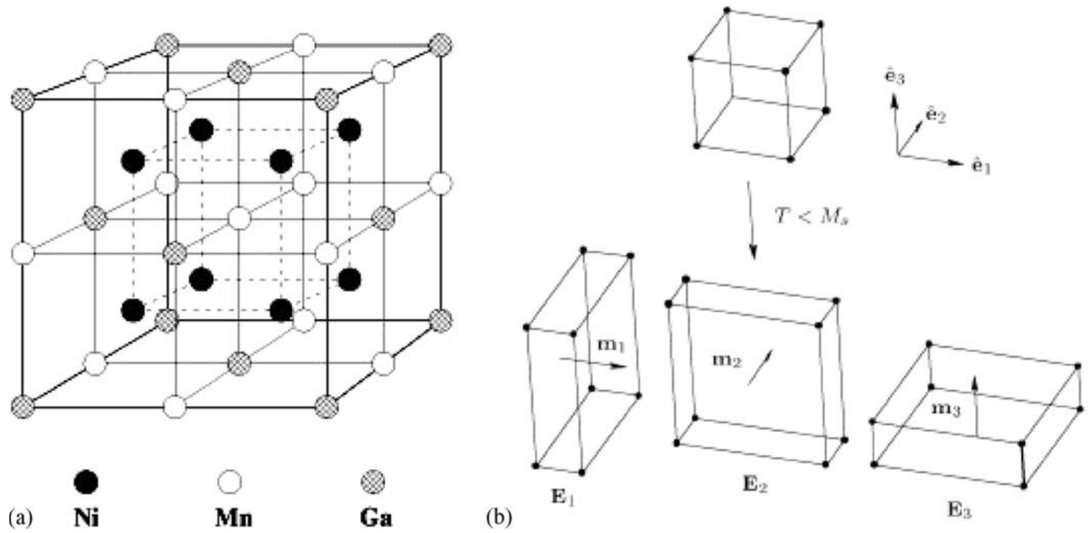

Fig. 10. (a) Ni-Mn-Ga Cubic Heusler structure in the high temperature austenitic phase and (b) tetragonal variant structure [53].

Besides the ferromagnetic nature of the martensitic phase, two additional conditions must be fulfilled: high magnetic anisotropy energy and very low critical stress for variant reorientation in the order of a few MPa (Fig. 11).

The alloys transforming to the so-called five- or seven-layered (10M, 14M, respectively) martensites satisfy such conditions in Ni-Mn-Ga alloys [52]. Their structures have nearly tetragonal or orthorhombic unit cells with $c/a < 1$ and $c < b < a$, respectively (in the axes derived from the parent cubic cell), accompanied by periodic shifts of the {1 1 0} planes with periods of five or seven basic unit cells [53]. In both structures, the easy axis of magnetization is along the shortest c axis.

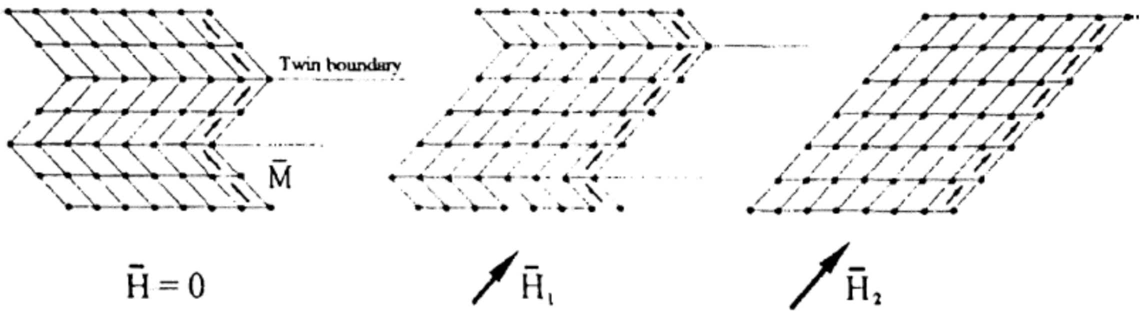

Fig. 11. Schematic illustration of the magnetic shape memory effect (H2 >H1) [54].

The FSMA alloys usually have martensitic transformation temperatures not much above room temperature or below. At an atomic level, two twin variants connected with a twin boundary are depicted in Fig. 12. The twin structure is created by a simple shear of one part of the crystal along the shear plane. For a coherent twin boundary, the twin boundary plane is a mirror plane between the adjacent variants.

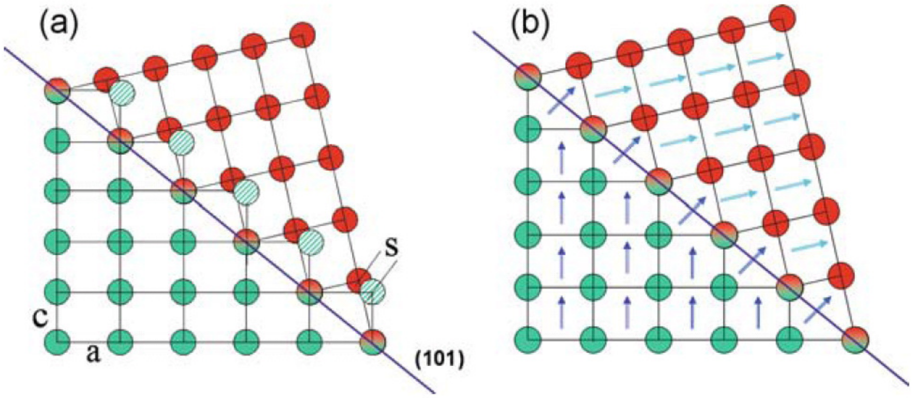

Fig. 12. 2D schematics of twinning (a) *s* is the magnitude of twin shear and its direction is parallel to the twin plane (101). (b) magnetic moments direction in the connected twin variants. The easy axis of magnetization is related to the short crystallographic axis. The rotation of magnetic moments in reality is across over the twin boundary producing a 90◦ magnetic domain wall [34].

The Ni-Mn-Ga alloys transforming to the non-layered tetragonal martensite generally having relatively high values of *e*/*a* and do not show large MFIS. This structure again in the axes derived from the parent cubic cell and has tetragonal structure with $c/a > 1$ knowing also as 2M in other axes. In spite of the 10M and 14M structures in Ni-Mn-Ga alloys, the crystallographic axis *c* shows the hard axis of magnetization, and the easy axis is on the orthogonal plane [52]. The Ni-Mn-Ga alloys with high values of *e*/*a* ratio compositions are relatively far from the stoichiometric Ni_2MnGa, and exhibit the paramagnetic martensitic transformation above room temperature [50] which can be taken into consideration as high temperature conventional shape memory alloys (not magnetically driven).

Nevertheless, the Ni-Mn-Ga alloys have some problems for their use in industrial applications. Concerning the magnetic actuation, the characteristics of the strain versus magnetic-field curve change considerably from one crystal to another (elaborated in the same way), which makes it difficult to control the actuators at large-scale productions. This is due to the high dependency of some critical parameters (like the stress for variant reorientation) on the internal defects present in the material.

The Curie point of Ni-Mn-Ga alloys is below 373 K, which is a too low temperature for some applications. The most important problem, however, is the high fragility of the material.

In the last few years, other ferromagnetic shape memory alloys exhibiting a thermoelastic martensitic transformation are being investigated in order to overcome these problems, and to increase the fundamental knowledge in systems presenting both structural and magnetic transitions. Among them are alloys where the magnetic actuation is mainly with the same mechanism as in Ni-Mn-Ga, i.e. the field-induced variant reorientation. Many researchers have evaluated the effects of additions of different fourth elements to Ni-Mn-Ga, and continued with investigating other *Heusler* (or B2) Ni-based alloy systems, like Ni-Mn-X or Ni-Fe-Ga, as well as Co-Ni-Al and Co-Ni-Ga alloys. Ferromagnetic Fe-based alloys, such as Fe-Ni or Fe-Pt have also been assessed, together with the field-induced variant reorientation in Fe_3Pt and Fe-Pd alloys. A new mechanism of magnetic actuation in Ni-Mn-In-Co was recently introduced [55].

1.1.5. Transformation Thermodynamics

Generally, martensitic transformation advance only when the temperature drops below *Ms* [40]. For the simplicity, the total energy change ($\Delta G^{P \to M}$) due to the martensitic transformation of a parent phase (P) phase into a lens-shaped martensite (M) phase with the thickness of 2t and radius r is:

$$\Delta G^{P\rightarrow M} = \pi r^{2} t \Delta g_{c} + 2\pi r^{2}\sigma + \pi r t^{2}(A+B) \qquad \text{Eq. 3}$$

where Δg_c is the change in chemical free energy per unit volume, σ is the interface energy between the P and the M phase per unit area, A (t/r) is the elastic strain energy per unit volume and B (t/r) is the plastic strain (deformation) energy per unit volume of M and P crystal accordingly [25].

In order for thermoelastic martensite transformation to occur, both the interfacial energy and the energy needed by the plastic deformation must be so small that they can be neglected. This is possible when during the transformation the structural changes and, consequently, the volume changes are both small, and when there is a good coherency between the P phase lattice and the M phase lattice [25]. According to the Eq. 3, the total energy change during the thermoelastic martensitic transformation can be shown as:

$$\Delta G^{P\rightarrow M} = \pi r^{2} t \Delta g_{c} + \pi r t^{2}(A) \qquad \text{Eq. 4}$$

On the other hand, the total energy change for the transformation from M phase to P phase can be shown in a similar manner. According to the Eq. 4, it can be separated into two terms named thermal and non-thermal terms. For the TSMAs, the interplay between thermal energy associated with the thermal term and the mechanical work associated with the second term are mainly contributed to the shape memory behavior (Fig. 13 (a)). Recently, it has also been found that the magnetic field can affect the non-thermal term, and can result in significant deformation of crystal structure in materials (Fig. 13 (b)).

The applied magnetic field (H) in a certain direction with respect to a martensite twin boundary can create a "*Zeeman pressure*" of the magnitude 2MsH on the twin boundary [56-59]. The Zeeman pressure resulting from the magnetic field acts on the ferromagnetic moment (Ms) may be sufficient to swap the crystallographic axes [60].

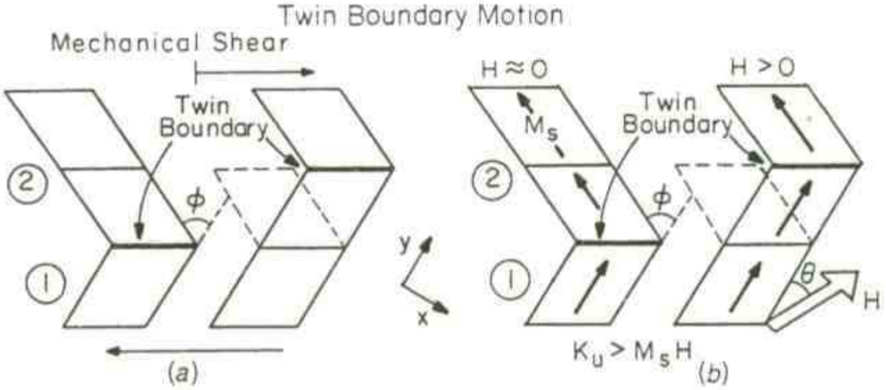

Fig. 13. (a) Thermoelastic Shape Memory (TSM) and (b) Ferromagnetic Shape Memory (FSM) behavior (Note:Ku: mechanical energy, MsH: magnetic energy) [57].

Unlike the thermoelastic shape memory effect, the magnetic shape memory effect occurs fully within the low temperature (martensitic) phase. Therefore, it has the potential to be faster and more efficient than thermoelastic shape memory [2].

The response time of shape memory alloys is a crucial factor for determining its application [61]. In TSMAs, the response time mainly depends on the thermal properties and the size of the materials due to heat transfer rate [62]. On the other hand, the response time for FSMAs depends on the magnetic susceptibility of the alloys. It has been determined that the response time of FSMAs can be 20 times faster than that of TSMAs due to the faster transport behavior of the magnetic field compared to the thermal field [2].

1.1.6. Co-Ni-Ga and Co-Ni-Al FSMAs

It has been found that the recently discovered Co-Ni-Al and Co-Ni-Ga alloys can provide improved ductility compared to other FSMA members since these Co- and Ni-based alloys generally consist of a dual-phase structure with the second phase imparting enhanced room temperature ductility significantly [12-18]. The improvement in ductility of FSMAs is a desirable characteristic for subsequent handling and processing steps, and has been investigated from many points of view like different chemical composition, single crystals, rapid solidification, and bulk undercooling [26, 27, 63-70].

The behavior of the different alloys on the amount of MFIS (achieved by variant reorientation), domain of martensitic transformation temperature and ductility of the alloys, as summarized by Pons *et al.* has been given in Table 1 [55].

According to this summary, most of the alloys considered can have better ductility than Ni-Mn-Ga, either as an intrinsic feature (Fe based alloys) or because of a controlled γ phase precipitation. The maximum amount of MFIS obtained in these alloys is clearly lower than in Ni-Mn-Ga (ternary or modified with quaternary additions).

In principle, it is also possible to cause the martensitic phase transformation by application of a magnetic field, which enables the devices to operate at high frequencies, and facilitates their remote control. However, the strength of the field required is prohibitively large for practical applications [71]. Instead, a magnetic field can be very effective in changing the twin structure, and hence the sample shape, if the uniaxial easy direction of magnetization changes across the twin boundary and the anisotropy energy is large. As a result, the martensitic variants with favorable orientation to the field grow at the expense of other variants. Eventually, the maximal magnetic field induced strain is limited by the tetragonality (1-*c*/*a*) ratio. The distinction between the strains due to twin boundary motion and magnetostriction is that the former is linearly and the latter is quadratically proportional to magnetization, M, below saturation.

Table 1.Summary of the amount of MFIS, structure of the parent and martensitic phase, transformation temperature (T_M) and ductility (in relation to Ni-Mn-Ga) of different alloys [55].

Alloy	**MFIS reported**	**Parent/martensite structure/T_M**	**Ductility**
Ni-Mn-Ga	6-10% in SC around RT or below	L2$_1$/10M or 14M/around RT or below; L2$_1$/2M above or well below RT	
Ni-Mn-Ga-Fe	1-5.5% in SC around RT or below	L2$_1$/10M or 14M	Better
Ni-Mn-Al	0.17% in SC, 0.01% in PC at 253 K	B2 (L2$_1$)/10M 12M 14M/around RT or below; B2 (L2$_1$)/14M or 2M/above or well below RT	Improved by γ phase
Ni-Fe-Ga	0.02% in SC at ~100 K	L2$_1$/10M 6M 14M/above and below RT	Improved by γ phase
Ni-Fe-Ga-Co	0.7% in SC at 300 K		
Co-Ni-Al	0.06% in SC at 165 K; 0.013% in PC at 293 K	B2/L1$_0$ (=2M) below, above and well above RT	Improved by γ phase
Co-Ni-Ga	0.011% in MS ribbons; 0.003% in PC at RT	B2/L1$_0$ (=2M) below, above and well above RT	Improved by γ phase
Fe$_3$Pt	~0.6% in SC at 4.2 K	Ordered fcc/fct/~100 K	Intrinsically better
Fe-Pd	3.1% in SC at 77 K; 0.01-0.05% in PC; 0.06-0.07% in MS ribbons	Disordered fcc/fct/around RT or below	Intrinsically better

SC: single cycles; PC: polycrystals; RT: room temperature

FSMAs can be found naturally in Fe-based alloys and a few engineered alloys; For example, FeNiCoTi [72]. Fe-Pt [73] alloys are FSMAs but their transformation temperatures are at low technologically uninteresting temperatures. Fe$_{70}$Pd$_{30}$ alloys [44, 75] are FSMAs at slightly below room temperature (RT) with reversible field-induced strains of 0.5 %at -17 ºC. FeMnSiX alloys [76] are SMAs and potentially FSMAs, but they are limited in their practicality due to their large hysteresis.

It is thus obvious that the twin boundary motion can be induced by the mechanical stress in all the SMAs. The same effects of macroscopic deformation can be produced by exerting magnetic forces to the twin boundaries in FSMAs, which makes this new class of material technically interesting.

1.1.7. Phase Transformations in FSMAs

In 1968, Webster was the first to describe in detail the magnetic properties of a new alloy with stoichiometric composition Ni_2MnGa [77]. Extensive research in Poland [78], and later on in Russia [79-81] revealed the existence of a martensitic transformation in this system. Large, reversible, magnetic-field-induced strains of order 0.2% were reported in single crystals of Ni_2MnGa by Ullakko *et al.* in 1996, and a shift in the martensitic transformation temperature of at most one or two degree under 10 kOe magnetic field was also reported [1]. In 1997, Ullakko *et al.* [54], and a little later, Wuttig and James first suggested and established that this transformation can be utilized in the form of a two-way shape memory effect. In 1999, a 5% shear strain was discovered at RT in a field of 4 kOe in 5-layer tetragonal NiMnGa martensite by Murray *et al.* [82]. More recently, the MFIS close to 10% was detected in 7-layer orthorhombic NiMnGa modulated martensite [83], which is, as for now, the largest MFIS attained in FSMAs.

The necessary conditions for the occurrence of FSMAs have been surveyed by Wuttig *et al*. [7, 47], and a constrained theory of magnetostriction intended to describe strain versus field and the associated microstructural changes in these materials was given by DeSimone and James [84]. Various phenomenological models have been proposed to understand the elastic and magnetic properties in FSMAs. O'Handley [45] presents a model for the magnetization process, field-induced strain by twin-boundary and phase-boundary motion and accounts for the magnetic anisotropy, based on a particular twinned domain structure. It shows good agreement with experimental data of Ullakko *et al*., and suggests that the competition of twin blocking stress and magnetic driving force leads to a restricted temperature window for magnetic actuation using Ni_2MnGa alloys. L'vov [86] starts from an expression for the Helmholtz free energy of a cubic crystal to derive the expressions for the static magnetic susceptibility and for the magnetization of the martensite. Their analysis demonstrates that the magnetization of FSMAs is closely related to the spontaneous strains arising at martensitic temperature T_M, which indicates a strong magneto-elastic coupling in the vicinity of martensitic phase transformation.

1.1.7.1 Phase Transformations in Co-Ni-Ga FSMAs

Co-Ni-Ga and Co-Ni-Al has been recently discovered as new members of the FSMA family, and they have been found to have many advantages over existing FSMAs. The most important advantage is that these two alloys possess improved ductility [12-18], which is important for subsequent processing. Compared to Ni-Mn-Ga, Co-Ni-Ga alloys have higher Curie temperature (T_C) which causes higher magnetization at operating environment. Some investigations have been carried out on Co-Ni-Ga polycrystal line samples, melt spun ribbons as well as single crystal samples [16-18].

Fig. 14 shows typical DSC and thermomagnetization curves. The endothermic and exothermic reactions relating to the martensitic transitions are observed upon heating and cooling, respectively. Temperatures characterized as the martensitic and austenite transitions (M_s, M_f, A_s and A_f,) were defined as the cross points of the baseline and the tangent of the maximum or minimum inclination in the DSC curves (Fig. 14 (a)). The thermomagnetization curves of a Co-22.5 at% Ni-30 at% Ga alloy quenched from 1200°C in a magnetic field of 500 Oe (Fig. 14 (b)) show steps corresponding to the martensitic and austenite transition temperatures. This is because the magnetization saturation is more easily accomplished in the austenite phase than in the martensite phase.

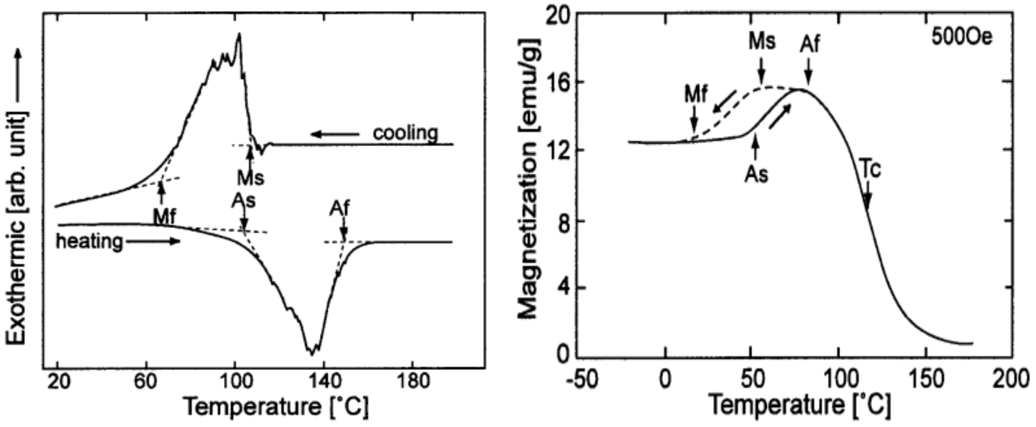

(a) (b)

Fig. 14. DSC curve of Co-23.5at%Ni-30at%Ga (a) and magnetization-temperature curve of Co-22.5at%Ni-30at%Ga quenched from 1200 °C (b).

The relative position between two characteristic temperatures; the martensitic transformation (Ms) and the Curie temperatures (T_C) are critical for determining whether or not an alloy would exhibit the FSM behavior [9, 12]. Fig. 15 shows three types of transformation behavior in shape memory alloys in which *P* and *M* are parent (austenite) and martensite phases, accordingly, and indices show the phase structure (β or β') as well as paramagnetic (*p*) and ferromagnetic (*f*) state in each stage of phase transformation. Type I transformation (Fig. 15) is attributed to FSMAs since the deformation in the SMA can be induced by the applied magnetic field. This is because the T_C is at a higher temperature compared to the *Ms* temperature. On the other hand, the material will exhibit TSM behavior if it experiences Type III transformation. Depending on the alloy composition, the magnitude and the relative position between these two characteristic temperatures can be manipulated to obtain a desirable FSM behavior.

	Hot $\leftrightarrows$ **Cold**
Type I	$P_p^{\beta} \xleftrightarrow[Tc]{} P_f^{\beta} \xleftrightarrow[Ms]{} M_f^{\beta'}$
Type II	$P_p^{\beta} \xleftrightarrow[Tc\,,Ms]{} M_f^{\beta'}$
Type III	$P_p^{\beta} \xleftrightarrow[Ms]{} M_p^{\beta'} \xleftrightarrow[Tc]{} M_f^{\beta'}$

Fig. 15. Three types of transformation behavior in shape memory alloys [12]

It was experimentally found that the interplay between Co and Ni content for a certain Ga concentration has an impact on the FSM behavior. High Co content is favorable for obtaining the FSM behavior by elevating the *Tc* temperature, while high Ni content will increase the *Ms* temperature [12] (Fig. 16). At a critical Ni content, the Co-Ni-Ga will lose the FSM behavior and tend to exhibit an ordinary TSM behavior [12].

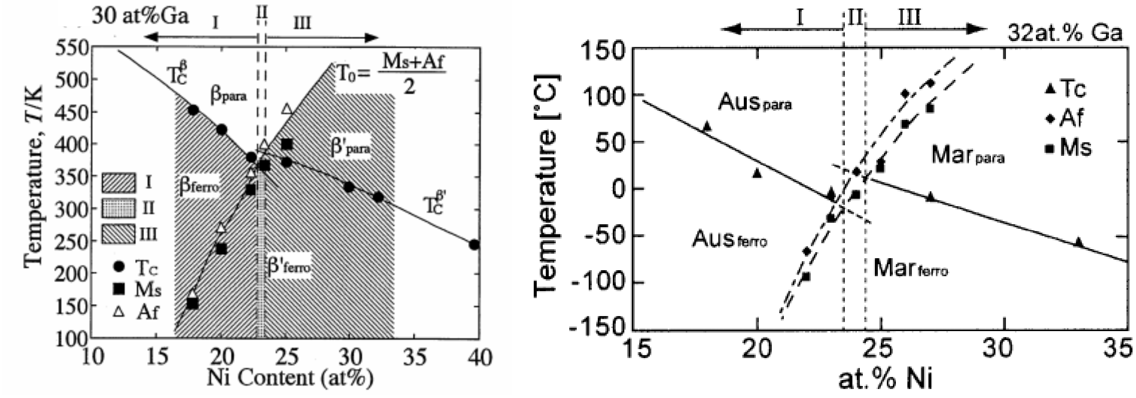

(a) (b)

Fig. 16. The dependence of characteristic temperatures (T_c and M_s) on Co and Ni concentration [12].(a) Co-Ni-30 at% Ga (b)Co-Ni-32%at% Ga.

1.1.7.2. Martensite Transformation Temperatures versus Valence Electron Concentration

SMAs can be located by considering electronic instabilities, elastic softening of the bcc β phase, and the detailed structural relationship between the phases at high and low temperatures [47]. Therefore, diffusionless martensitic transformations can occur at certain critical average electron concentrations in shape memory alloys. For instance, the martensitic transformations in Cu-based alloys systems occur at average valence electron (s electrons layer) concentration about 1.5 ($<s> \approx 1.5$) [87] while those in Fe-based alloys occur at average valance electron (s, p, d electrons layer) concentration about 8.5 ($<s+p+d> \approx 8.5$) [88]. The martensitic transformation in Ni-Mn-Ga *Heusler* alloys occurs at an average valence electron concentration of approximately 7.3 [89]. Their saturation magnetization falls on the known Bethe-Slater plot only if all outer electrons are counted, i.e. $<s+p+d> \approx 10$ [47]. As mentioned previously, not all martensites are SMAs, but those that fulfill certain special relationships between the lattice parameters of the austenite and martensite phases [90]. This is schematically indicated in Fig. 17 [16].

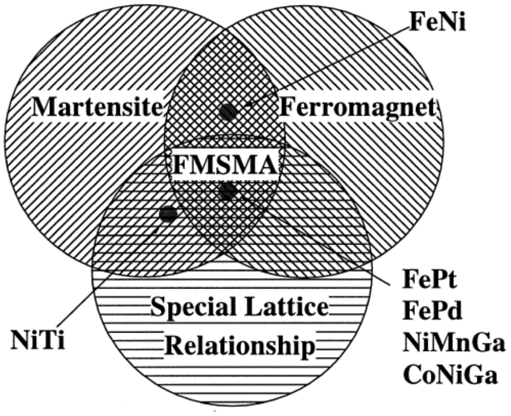

Fig. 17. Conceptual position of several alloy systems in the Martensite, Ferromagnetic and Special Lattice Relationship groups. Alloys in the overlap group of all three are FSMAs [16].

In its simplest form, a search for new Co-based FSMAs can thus start by identifying a potential Co-based *Heusler* alloy with an average valence electron concentration of approximately 7.3 [16]. Among Co-based alloys, Co-Ni-Ga is similar to Ni-Mn-Ga in thevalance electron concentration <s+p+d> ≈ 10. Thus, $Co_2Ni_{1-x}Ga_{1+x}$ alloys may be ferromagnetic, and display SMA characteristics.

The microstructural analysis suggests that the cause for the decrease in transformed phase percentages resides in the presence of the γ phase (Co-rich precipitates). It has been shown by Craciunescue *et al.* [28] that the higher the Co/Ga ratio, the more precipitates form and the less the matrix. The change in the transition temperature is tentatively attributed to the Ga content of the matrix as shown in Fig. 18. The lower the Ga content is the higher the transition temperature. The analysis of the binary Co-Ga and Ni-Ga phase diagrams suggests that Ga content of the matrix can be reduced by solution treatment followed by quenching. Accordingly, the quenched state of a Co-rich two-phase alloy in the Co-Ni-Ga system should display a higher transition temperature compared to the unquenched one due to the higher solubility at high temperatures.

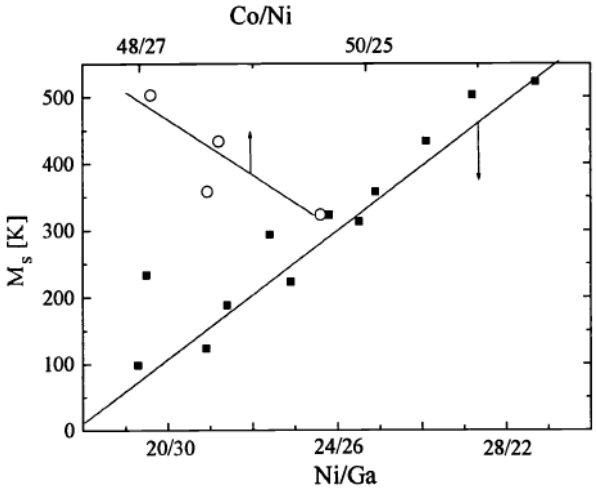

Fig. 18. Martensitic start (*Ms*) temperatures versus the component ratio for the investigated Co-Ni-Ga alloys [28].

The alloys showing the phase transformation are in the compositional range of the *Heusler-type* alloys. In the Co-Ni-Ga ternary phase diagram, favorable conditions exist for the formation of solid solutions of this kind because the Co-Ni binary phase diagram shows a very large solubility of the components [91]. Thus, the overall metallurgical limitations are not so tight. Furthermore, both Ga-Ni and Co-Ga binary phase diagrams contain B2 phases that favor the formation of *Heusler* alloys in the ternary diagram [92]. The shaded region in Fig. 19 shows an estimated composition range in which Co-Ni-Ga solid solutions might be obtained. It is likely that this range can be expanded; In both Ni-Ga and Co-Ga phase diagrams, the regions of the B2 phase expand at higher temperatures, and can be stabilized by quenching, thereby extending the shaded region where *e*/*a*> 7.3.

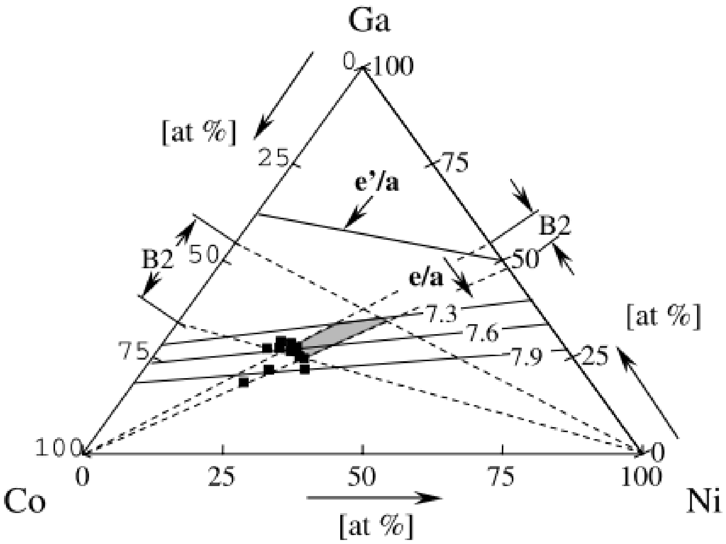

Fig. 19. Compositional range for the formation of Co_2NiGa FSMAs (see text for details) [28]

Insight into the potential saturation magnetization of the alloys can be obtained from the known Slater-Pauling curve [Wutig-FSMA1] and Wuttig *et al.* studies [16] on the occurrence of FSMAs. It is suggested that finite values of the saturation magnetization can be obtained from electron (d+s+p) per atom (electron/atom) ratios larger than 11.5 (*e'*/*a*≈ 11.5). The structural stability of the alloys is determined by an electron/atom ratio as well [20]. However, only the outer <s+p> valence electrons of Ga must be counted. The empirical stability diagram of Ni-Mn-Ga and Co-Ni-Ga *Heusler-type* alloys is shown in Fig. 20. This figure indicates that the limit of the structural stability of both alloy systems occurs at a critical electron/atom ratio *e*/*a*≈ 7.3 [17].

The two electron concentrations *e/a* and *e'/a* have been included in Fig. 19. It can be seen that only the metallurgical and structural stability criteria control the formation of potentially unstable ferromagnetic Co-Ni-Ga *Heusler* alloys.

Fig. 20 also shows the similarities in the evolution of the transformation temperatures as a function of the electron concentration of Co-Ni-Ga and Ni-Mn-Ga *Heusler-type* FSMAs as discussed by Chernenko [29], and summarized by Schlagel *et al.* [19]. A similar trend can be observed for both systems, in which the transition temperatures tend to 0 K when *e/a*=7.3 increasing with the same slope as *e/a* increases. While in the Ni-Mn-Ga system, higher transition temperatures can be reached by adding Ni at the expense of Ga and Mn, in the Co-Ni-Ga system both Co and Ni can be used to increase the transition temperatures, because their electron concentrations are very close.

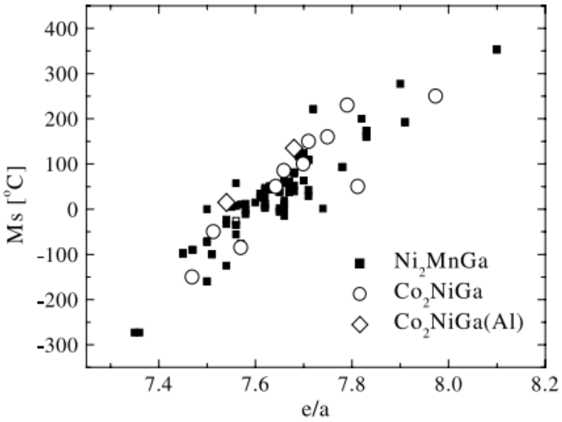

Fig. 20. The effect of the electron/atom ratio on the M_s temperature in $Co_2NiGa(Al)$ and Ni_2MnGa FSMAs. Ni_2MnGa data (■) [19].

1.1.8. Magnetic Properties in FSMA

The interaction of the electron-induced magnetic moments with an external magnetic field results in the macroscopic magnetic properties of the materials. The three most common ferromagnetic elements are Fe, Ni, and Co. Magnetic domains are microscopic volumes in which the dipoles are aligned. When an external field is applied, it increases the net magnetic moment in the direction of the field. This process can occur either by the growth of favorably oriented domains or by dipole rotation. Because of the irreversible work required to move domain walls, a hysteresis loop is associated with a ferri or ferromagnetic material's response to alternating external magnetic fields [93].

In ferromagnetic shape memory alloys, magnetization vectors lie along certain definite crystallographic axes called easy axes or directions of easy magnetization. Crystal anisotropy energy is an energy that directs the magnetization along these directions [12]. When an external magnetic field is applied, the magnetization tends to turn from the easy direction of the unit cell to the direction of the external magnetic field. If the anisotropy energy is high, magnetic field strengths required to turn the magnetization are also high. If the energy of the motion of twin boundaries is low enough at the same time, magnetization can turn the unit cells as it turns to the direction of the external field. Magnetization then remains in the original easy direction in the turned unit cells.

Fig. 13 (b) illustrated how the unit cells of one variant are turned into another by external magnetic field. As a result, twins in favorable orientation to the magnetic field grow at the expense of other twins. This causes the twin boundary motion and the shape change of the material, which finally results in the stroke of the actuator made from this material [94].

The magnetic properties for an orthorhombic seven-layered phase in $Ni_{48.8}Mn_{29.7}Ga_{21.5}$ (at%) alloy at 300 K have been determined by Sozinov *et al.* [83] for single variant samples from the magnetization curves M (H) recorded along the [100], [010], and [001] directions. The samples were constrained by epoxy to prevent a magnetically field-induced redistribution of martensite variants during the measurements. The obtained results by their group for the magnetic measurements are shown in Fig. 21. The magnetization curves indicate that the shortest axis (*c* axis) is the axis of easiest magnetization, the longest (*a* axis) is the axis of hard magnetization, and the *b* axis is the intermediate one. Unlike for a single uniaxial magnetic anisotropy constant of tetragonal phase, two magnetic anisotropy parameters are required to characterize the orthorhombic crystal structure in this case. The values of magnetic anisotropy constants $K_b = 0.7\times10^5$ J/m^3 and $K_a = 1.6\times10^5$ J/m^3 were calculated from the magnetization data (Fig. 20) as the area cross section between the easiest curve (*c* axis) and the two others (*b* and *a* directions).

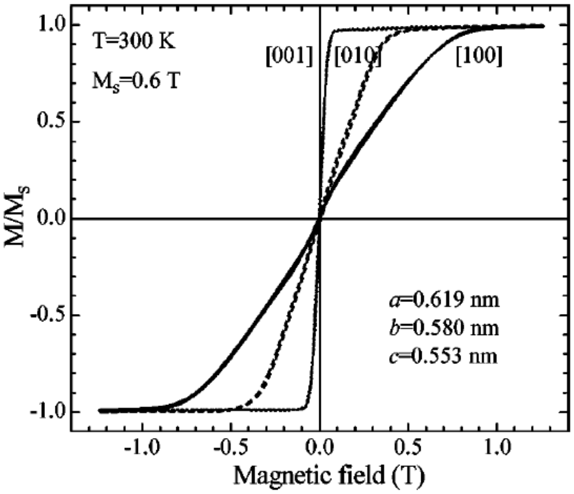

Fig. 21. Magnetization curves measured along different axes of orthorhombic seven-layered phase (the single-variant constrained state) in the$Ni_{48.8}Mn_{29.7}Ga_{21.5}$alloy at 300 K [83].

The temperature dependence of the magnetization of the as-grown and post-annealed single crystals with nearly stoichiometric (Ni_2MnGa) composition, which was reported by Chu *et al.* is shown in Fig. 22 (a) [95].

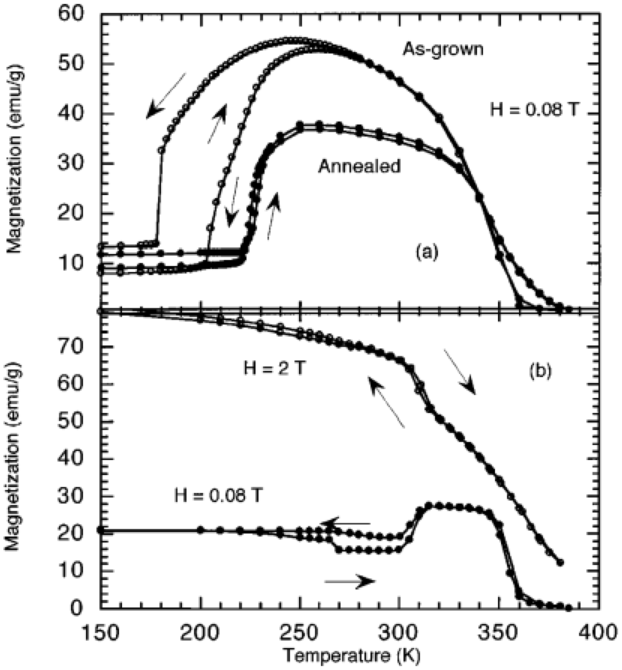

Fig. 22. Temperature dependence of the magnetization of (a) as-grown and annealed crystals with stoichiometric composition of Ni_2MnGa and (b) the crystals with off-stoichiometric composition of $Ni_{52.7}Mn_{22.6}\,Ga_{24.7}$ (at.%) at low (0.08T) and high (2T) magnetic field [95].

The experimental protocol they employed was as follows. 1) The sample was first cooled from 385 K to 5 K in zero field; 2) its DC magnetic moment was then measured as a function of increasing temperature as the sample was heated above the ferromagnetic Curie temperature in applied field of 0.08 T; 3) the crystal was finally cooled to 5 K under the same applied field. Compared to the as-grown sample, the M_s, and A_s temperatures in the post-annealed sample were significantly enhanced from 177.5 to 221.5 K and from 202.5 to 224.5 K, respectively. An off-stoichiometric alloy of composition $Ni_{52.7}Mn_{22.6}Ga_{24.7}$ (at.%) exhibits onset temperature for the structure transition and magnetic transition (T_C) at 304 K and 359 K. The shape of the magnetization curves shown in Fig. 22 (b) is a typical magnetization curve for occurring a structure transition in the FSMAs at low and high field.

Fig. 23 shows the thermomagnetization curves on cooling and heating cycles obtained by Sutou *et al.* [96] in the VSM technique for Ni-Mn-X alloys (a) $Ni_{50}Mn_{34}In_{16}$, (b) $Ni_{50}Mn_{37}Sn_{13}$ and (c) $Ni_{50}Mn_{37}Sb_{13}$ alloys at a magnetic field strength of H=500 Oe.

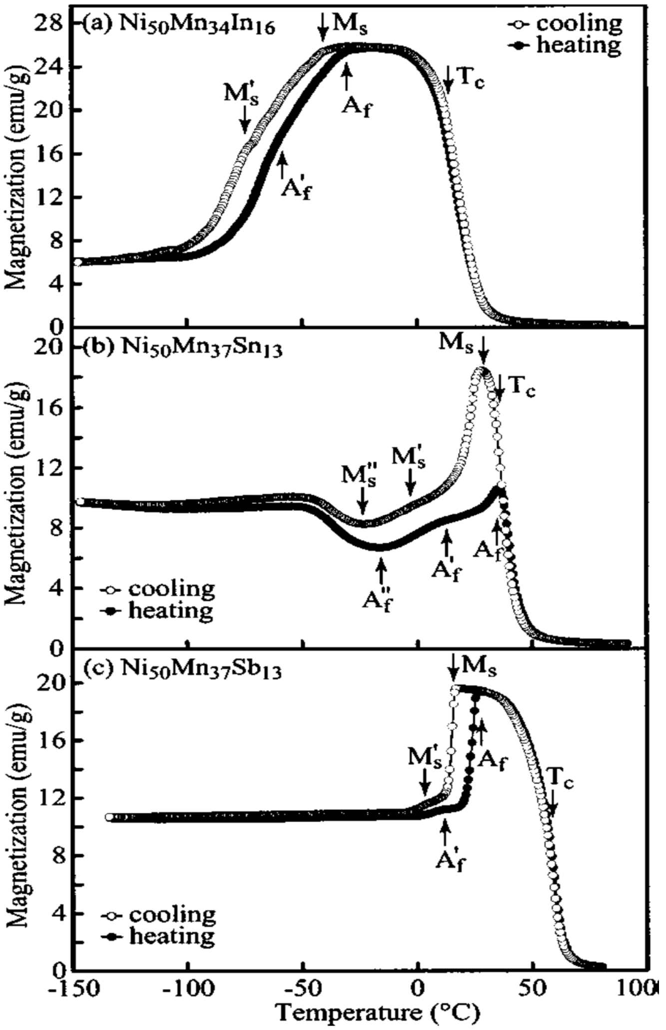

Fig. 23. Thermomagnetization curves of the (a) $Ni_{50}Mn_{34}In_{16}$, (b)$Ni_{50}Mn_{37}Sn_{13}$ and (c) $Ni_{50}Mn_{37}Sb_{13}$ alloys measured by VSM [96].

The thermomagnetization curves first drastically increase due to the magnetictrans formation from the paramagnetic to the ferromagnetic state in the cooling stage from around 80°C. The *Tc* temperature is defined as the temperature at which the slope of magnetization versus temperature curve is the largest, as shown in Fig. 23. Subsequently, the magnetization abruptly decreases because of the martensitic transformation and intricately changes with further cooling.

There is another technique to investigate the magnetic properties of FSMA in different temperatures through measuring of the low-field ac magnetic susceptibility (χ). The temperature dependencies of the low-field ac magnetic susceptibility, χ, for $Ni_{2+x}Mn_{1-x}Ga$ has been measured by Vasil'ev *et al.* as shown in Fig. 24 (a), which displayed a very sharp changes at martensitic and magnetic transitions [26].

The drastic drop of χ indicates the martensitic phase transition from the cubic to the tetragonal structure. The low-field ac magnetic susceptibility, χ, also sharply decreases at the Curie temperature when the ferromagnetic phase is destroyed.

Fig. 24 (b) shows the temperature dependence of the low field ac magnetic susceptibility of the $Ni_{48.8}Mn_{29.7}Ga_{21.5}$ alloy during heating and cooling [83]. The abrupt change in the value of the susceptibility at 367-369 K is attributed to paramagnetic-ferromagnetic transformation of the $L2_1$ cubic phase. The Curie temperature is about T_C= 368 K. The cooling–heating cycle in Fig. 24 (b) also shows a sequence of martensitic and intermartensitic transformations. The martensitic transformation starts at 337 K (M_s) and is completed at 333 K (M_f) during cooling. At lower temperatures, starting at 245 K, the value of the magnetic susceptibility increased, indicating the intermartensitic transformation. During heating both structure transformations occur in reverse order, and show some temperature hysteresis. In particular, the reverse intermartensitic transformation happens during heating at 306–316 K. So reverse martensitic transformation from the orthorhombic to the cubic parent phase upon heating takes place between A_s= 338 K and A_f= 342 K.

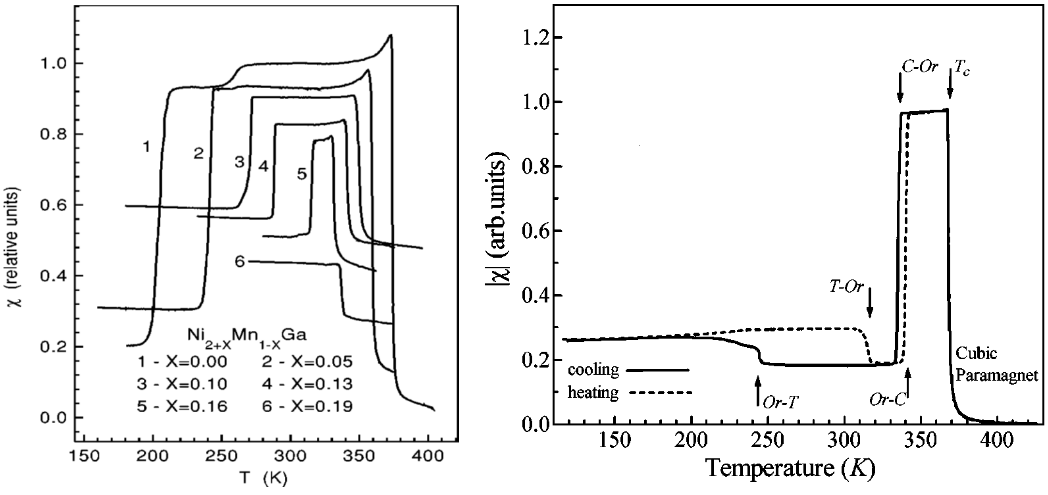

(a) (b)

Fig. 24. Temperature dependencies of low-field magnetic susceptibility (χ) of (a) $Ni_{2+x}Mn_{1-x}$ Ga alloys [26] and (b) $Ni_{48.8}Mn_{29.7}Ga_{21.5}$ alloy. Arrows mark phase transformations. *C*: ferromagnetic cubic phase, Or: orthorhombic seven-layered phase, *T*: tetragonal non-modulated phase.

1.1.8.1. Magnetic Properties in Co-Ni-Ga

Cobalt is a serious candidate for the fabrication of FSMAs because of its magnetic characteristics. However, only very few research has shown promising results in the use of Co as a component for the FSMAs [28]. Co-based FSMAs have been produced following two paths. One path uses the NiA1 shape memory system as a model in which Co has been added to cause a magnetic behavior [13, 28]. The other path has as a model the *Heusler-type* FSMAs for which the unique representative was the Ni_2MnGa system.

The Co-Ni-Ga FSMAs have been discovered [16] after a thorough analysis of *Heusler-type* alloys [12], and show ferromagnetic and shape memory behavior as bulk [16, 17] or thin films [18].

The magnetization curve of $Co_2Ni_{0.88}Ga_{1.12}$ was measured by Wuttig *et al.* [16], was and presented in Fig. 25. It depicts that the saturation magnetization in the quenched state (martensite phase) is comparable to that of nickel, as expected, and that the coercive force equals approximately 200 mT. In addition, the saturation magnetization depends on the state of the alloy, and it is different from the as-solidified sample. This agrees with previous observations on the ferromagnetic properties of $Co_2Ni_{1-x}Ga_{1+x}$, $0.3<X< 1$ [16, 25]. These indicated that the quenched alloys are ferromagnetic for $X< 0.5$, and that the saturation magnetization depends on the composition as well as the annealing state. It was also showed that the alloys possess an ordered B2 structure at austenite state.

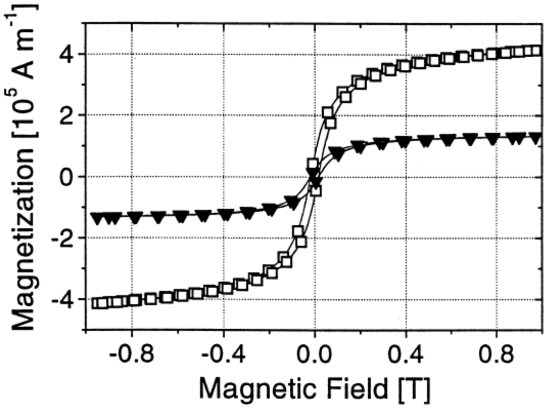

Fig. 25. Magnetization curves of $Co_2Ni_{0.88}Ga_{1.12}$ determined at room temperature. ▼for as-solidified sample, □ for 3 hours annealed at 850°C and quenched.

Fig. 26 (a) shows the magnetization versus temperature hysteresis at external magnetic field of 40 kAm^{-1} and Fig. 26 (b) shows the M-H loops for the $Co_{52.1}Ni_{26.1}Ga_{21.8}$ ribbon sample measured at 293 K (martensite phase) and 373 K (austenite phase). As shown in Fig. 26 (a), the magnetization curves have steps on heating and cooling process, which indicate the *As* and *Ms* temperatures, respectively. The M-H loops in Fig. 26 (b) show a wide hysteresis meaning that much magnetic energy is dissipated during the rearrangement of martensite twins. It can be observed that magnetization versus temperature curve has hysteresis loop and rapid variation occurred near phase transformation temperatures. The $Co_{52.4}Ni_{22}Ga_{25.6}$ ribbon sample also exhibits a similar behavior. Both results are similar to those seen for martensite phase of Ni_2MnGa, Ni_2MnAl and CoNiAl [13].

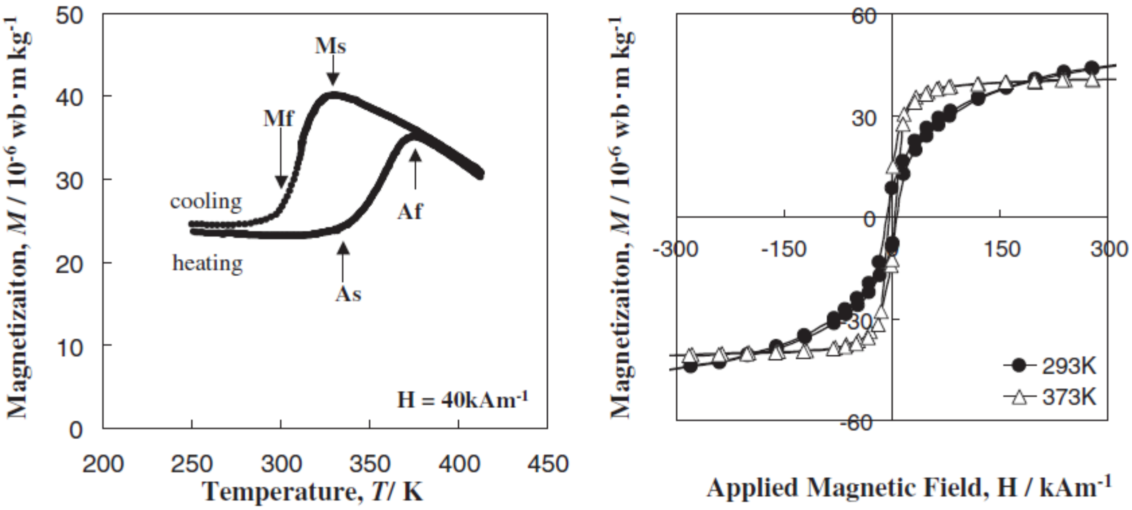

(a) (b)

Fig. 26. Magnetic properties of the $Co_{52.1}Ni_{26.1}Ga_{21.8}$ ribbon. (a) Temperature dependence of the magnetization in an external magnetic field of 40 kAm^{-1}. (b) Magnetic hysteresis loops at 293K (martensite phase) and 373K (austenite phase) upon heating [97].

Fig. 27 (a) shows the M vs. H loops of the $Co_{52.4}Ni_{22}Ga_{25.6}$ ribbon and Fig. 27 (b) represents a schematic diagram of measurement arrangement, which was reported by Sato *et al.* [82]. In their adjustment for measurement, the sample can be rotated around the rolling (longitudinal) direction (RD), and the magnetic field was applied perpendicular to the RD. Angle θ of the sample rotated around the RD is defined as an angle between the transverse direction of ribbon and magnetic field, as seen in Fig. 27 (b). They reported that magnetization M for θ= 0° was saturated at H= 400 kAm^{-1}, and had small coercive force, Hc of 5.44 kAm^{-1}. The saturation magnetization for ribbon sample, 47.73 $\times 10^{-6}$ $Wb.m.kg^{-1}$ at H= 800 kAm^{-1} has shown nearly equal to that of the bulk one. On the other hand, in the ribbon sample, the M for θ= 90° was not saturated still at H= 800 kAm^{-1} because of the induced large demagnetic field due to the very thin shape of the ribbon sample, and had larger coercive force than that for θ= 0° [82].

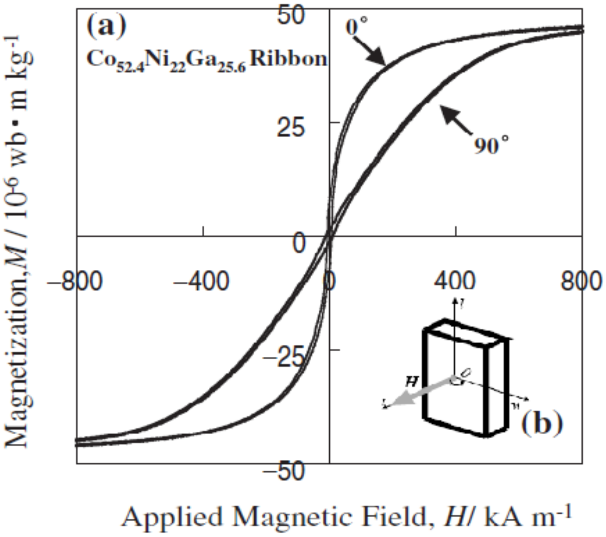

Fig. 27. (a) Direction dependence of magnetization of the $Co_{52.4}Ni_{22}Ga_{25.6}$ ribbon sample, and (b) schematic diagram of measurement directions

In summary, the ribbon sample has magnetically anisotropic texture because of its shape factor [98]. The bulk sample generally exhibits M versus H loops similar to that of the ribbon, but the coercive force is smaller. The similar results were also reported for the

$Co_{50.3}Ni_{23.2}Ga_{26.5}$ and $Co_{52.1}Ni_{26.}Ga_{21.8}$ ribbons. Based on the experimental data, the Ni_2MnGa alloy needs appropriate heat treatment in order to obtain a large magnetization, but Co_2NiGa system alloys have large magnetization at room temperature without any heat treatment.

Fig. 28 (a) and (b) also show the magnetization-temperature (M-T) curve at 0.04 MAm^{-1} on heating and the magnetization-external field (M-H) curves at 84 K and 223 K respectively for Co-18 at% Ni-30 at% Ga alloy, reported by Oikawa *et al.* , which is a typical FSMA under type I in Fig. 15 [12]. Note that the stable phase is β' at 84 K and β at 223 K [12].

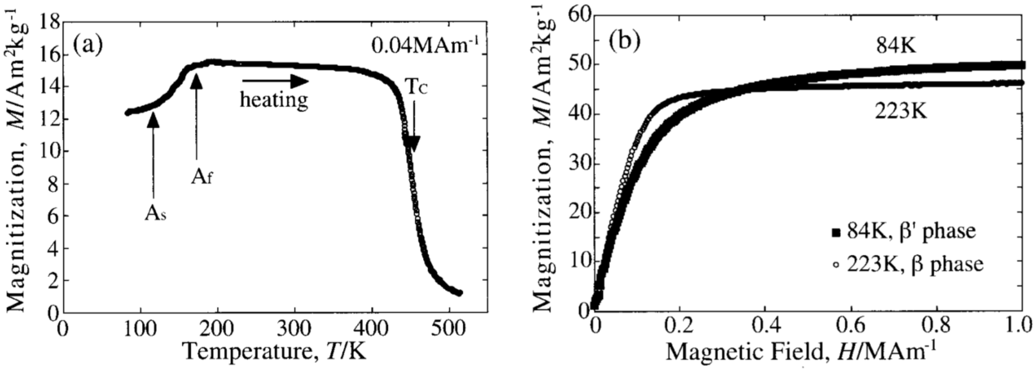

Fig. 28. Magnetic properties of Co-18 at% Ni-30at% Ga FSMAs. (a) M-T curve in an external magnetic field 0.04 MAm^{-1} on heating (b) M-H curves at 84 K and 223 K.

There is a step in the magnetization curve in the temperature interval between A_s and A_f as shown in Fig. 28 (a). As mentioned before, this is because the magnetization saturation is more easily accomplished in the β (austenite) phase than in the β' phase, as seen in Fig. 28 (b). These results are similar to those obtained in the Ni_2MnGa and Ni_2MnAl. The magnetic properties of the Co-Ni-Ga *β*-base alloys are very similar to those of the Co-Ni-Al *β*-base alloys [99].

Fig. 29 (a), which is reported by Zhang *et al.*, shows the isothermal M-H curves measured at above and below the martensitic transformation temperature. The apparent difference between the two phases clearly indicates the rolling direction of the magnetic moment when the temperature is increased to 280 K. The martensitic phase at a lower temperature (at 5 K) exhibited a high-saturated magnetization of 51.00 $Am^2\ kg^{-1}$ and a high anisotropy field of more than 1 T, but both decreased to 41.95 $Am^2\ kg^{-1}$ and 0.4 T at 300 K. A high-saturated magnetization was very important for high *Zeeman energy* driving the twin boundary motion and establishing a large MFIS [100].

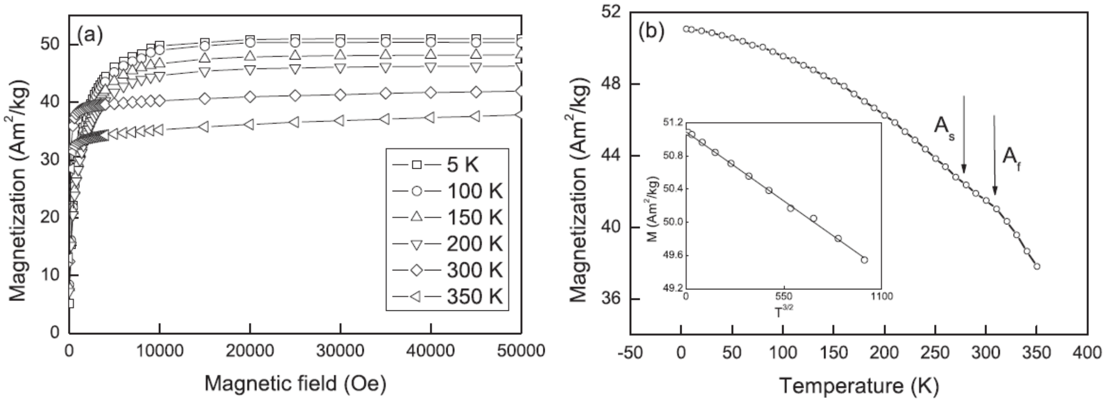

Fig. 29. (a) Magnetization dependence of the magnetic field for the$Co_{50}Ni_{20}Ga_{30}$ ribbon at various temperatures; (b) temperature dependence of magnetizations for the $Co_{50}Ni_{20}Ga_{30}$ ribbon under a field of 50 kOe. Inset graph shows the ribbon data for T<100K as a function of $T^{3/2}$ [101].

The spontaneous magnetization curves are shown in Fig. 29 (a). In addition, as seen in Fig. 29 (b), there were two unapparent kinks at temperatures of about 275 and 304 K relating to the reverse martensitic transformation during heating. The solid line in the inset graph in Fig. 29 (b) is a linear fit to the data, demonstrating the $T^{3/2}$ dependence of the magnetization for that low T range.

Fig. 30 (a) shows the direction dependence of coercive force of the ribbon and bulk samples which were reported by Sato *et al.* [82]. The coercive force of $Co_{50.3}Ni_{23.2}Ga_{26.5}$, $Co_{52.4}Ni_{22}Ga_{25.6}$ and $Co_{52.1}Ni_{26.1}Ga_{21.8}$ ribbons depends considerably on θ, and has maximum at θ= 70°-80°. It can be considered that this anisotropy originates from the strong texture that consists of columnar microstructure caused by the rapid solidification. On the other hand, the coercive force of the bulk samples depends scarcely on θ, indicating magnetically isotropic texture for the bulk samples.

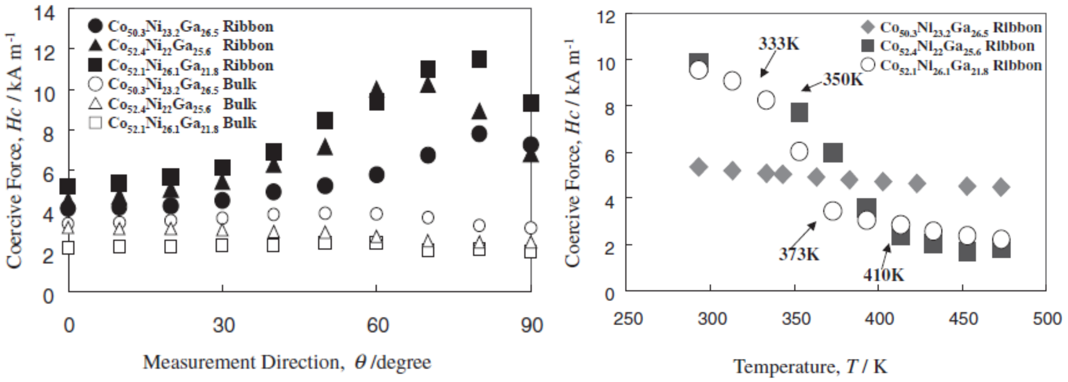

(a) (b)

Fig. 30. (a) Direction dependence of coercive force of the bulk and ribbon samples, (b) temperature dependence of coercive force of the three ribbons.

Fig. 30 (b) shows the temperature dependence of the maximum coercive force for three ribbons, obtained from M-H loops at the same source. When temperature increased, the coercive force of $Co_{52.4}Ni_{22}Ga_{25.6}$ ribbon rapidly decreased between 350 K and 410 K. The coercive force of $Co_{52.1}Ni_{26.1}Ga_{21.8}$ribbon also decreased at temperatures between 333 K and 373 K. This phenomenon occurred when the specimen becomes magnetically isotropic, which is accompanied with the phase change to austenite. It was also claimed the coercive force of $Co_{50.3}Ni_{23.2}Ga_{26.5}$ ribbon did not change in the same temperature range of their measurement.

1.1.8.2. Magnetostriction and Magnetic-Field-Induced Strains in FSMA

The FSM behavior with extensional strain of 0.2% was first observed in an unstressed Ni_2MnGa off-stoichiometry single crystal at 5 KOe in 1996 by Ullakko *et al.* (Fig. 31) [1]. A 4.3% extensional strain was observed in the same alloy under applied stress [102]. Recently, a shear strain of 5.7% at an applied field of 4 KOe at room temperature was observed [103].

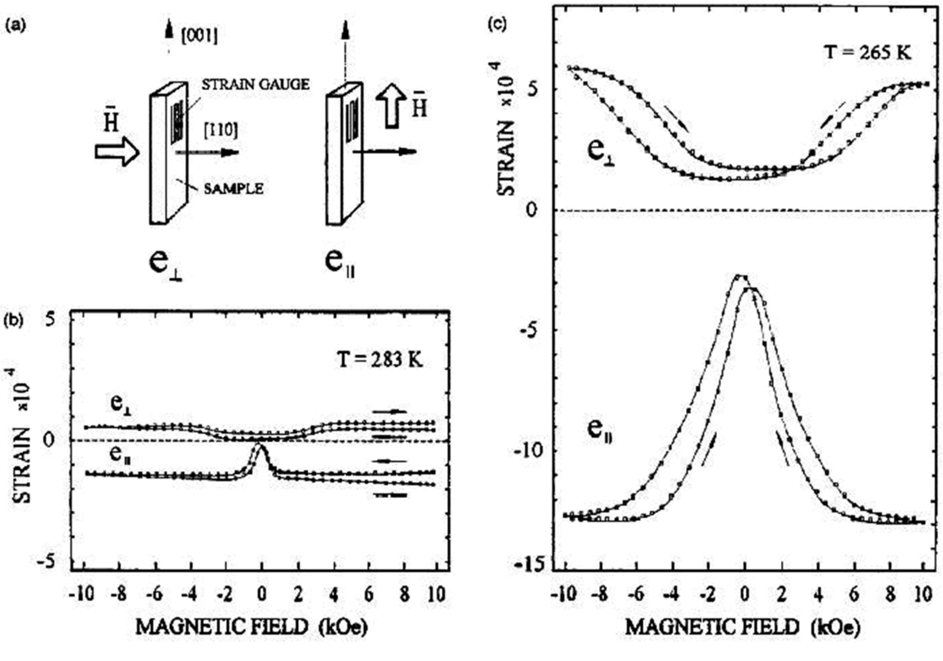

Fig. 31. Magnetic field induced strain in Ni-Mn-Ga FSMAs (a) in different crystallographic directions, (b) and (c) their corresponding strains [1].

Since the field of FSMAs is relatively new, there are a few alloy systems exhibiting FSM behavior; Fe-Pd, Fe-Pt, and Ni-Mn-Ga. Unfortunately, the first two Fe-based FSMAs require a relatively large magnetic field to induce FSM behavior compared to the Ni-based ternary FSMAs.

1.1.8.3. Magnetostriction and Magnetic-Field-Induced Strains in Co-Ni-Ga

Sato *et al.* [104] researched and developed a polycrystalline *Heusler-type* ferromagnetic shape memory alloy, Co_2NiGa, and showed a large magnetostriction effect caused by the magnetic-field-induced rearrangement of martensite twins. They produced ribbon samples by rapid-solidification melt-spinning method and showed strong texture and large magnetostriction strain (ε) of about 110×10^{-6} for an applied magnetic field of 800 kAm^{-1} at room temperature. Li *et al.* [105] reported a field-controlled two-way shape memory effect in single crystals of Co-Ni-Ga. They made single crystals of $Co_{50}Ni_{22}Ga_{28}$, $Co_{50}Ni_{21}Ga_{29}$ and $Co_{50}Ni_{20}Ga_{30}$ that can achieve a high transformation strain of 2.3% for two-way shape memory in a wide temperature range. By applying a bias field of about 0.8 T to the sample, they also claimed that the shape memory strain can be continuously adjusted from -2.3% to 0.0%. A positive strain up to +2.2% was obtained by increasing the field to 2.0 T in the different direction of shape deformation. A net strain of 4.5% has been reported upon the martensitic transformation under the influence of a bias magnetic field [12, 105].

Fig. 32 shows the optical image of the martensite on the (010) polished surface of a single crystal of $Co_{50}Ni_{22}Ga_{28}$. The martensitic variants with one set of parallel strips have been shown by Li *et al.* In the single crystal sample, there are two sets of variants which cross and overlap each other, and are symmetrically aligned with respect to the [001] direction. This morphology clearly reflects the preferential orientation of the variants about some crystallographic direction, which is a key condition for a large directional shape deformation upon the martensitic transformation, as revealed in Ni-Mn-Ga alloys [106]. On the sample cooling down to room temperature without a bias field, the generated reliefs had relatively large strips of 250 μm width, as shown in Fig. 32 (a). By applying a bias field of about 0.3 T, the variants nucleated during cooling, and the strips became quite narrow, about 100 μm, though still oriented in the same direction (Fig. 32 (b)). The figure also reveals the magnetic sensitivity of martensite in this ferromagnetic alloy, which indicates the possibility of shape memory being controlled by a bias magnetic field.

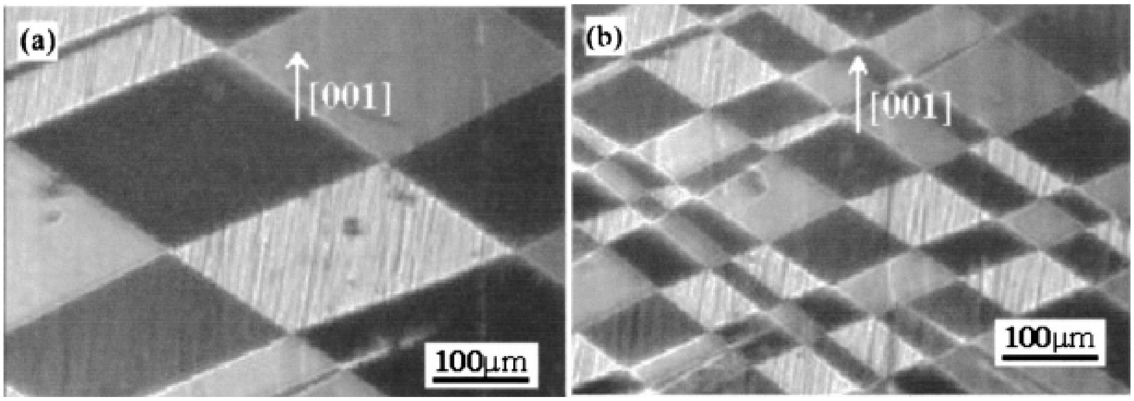

Fig. 32.Variants observed by optical microscope on the (010) surface of $Co_{50}Ni_{22}Ga_{28}$single crystal sample cooled from parent phase in zero field (a) and in a bias field of 0.3 T (b).

Fig. 33 (a) illustrates magnetostriction ε-H curves for $Co_{52.4}Ni_{22}Ga_{25.6}$ (a) ribbon and (b) bulk samples. Magnetostriction of ribbon depends remarkably on θ, and exhibits a maximum value of -110×10^{-6} at θ= 60° possibly due to the strong oriented texture of the sample. On the other hand, ε of the bulk sample in randomly oriented polycrystal has a maximum of -30 $\times10^{-6}$ at $\theta = 0°$, and is saturated at H = 450 kAm^{-1}. It was demonstrated that the magnetostriction of ribbon sample becomes 3.5 times larger than that of bulk sample for the same alloy [101, 104]. The enhancement of ε for ribbon is due to the strong texture, which consists of a fine columnar microstructure parallel to the thickness direction of ribbon film prepared by rapid solidification.

The magnetostrictions of $Co_{50.3}Ni_{23.2}Ga_{26.5}$ and $Co_{52.1}Ni_{26.1}Ga_{21.8}$ ribbons are smaller than that of the $Co_{52.4}Ni_{22}Ga_{25.6}$. As shown in Fig. 33 (b), during the measurements, the sample could be rotated with respect to the magnetic field. The angle θ is defined as an angle between the longitudinal direction and the magnetic field, i.e. $\theta = 0°$ and 90° means that the magnetic field is parallel or perpendicular to the surface of the ribbon, respectively.

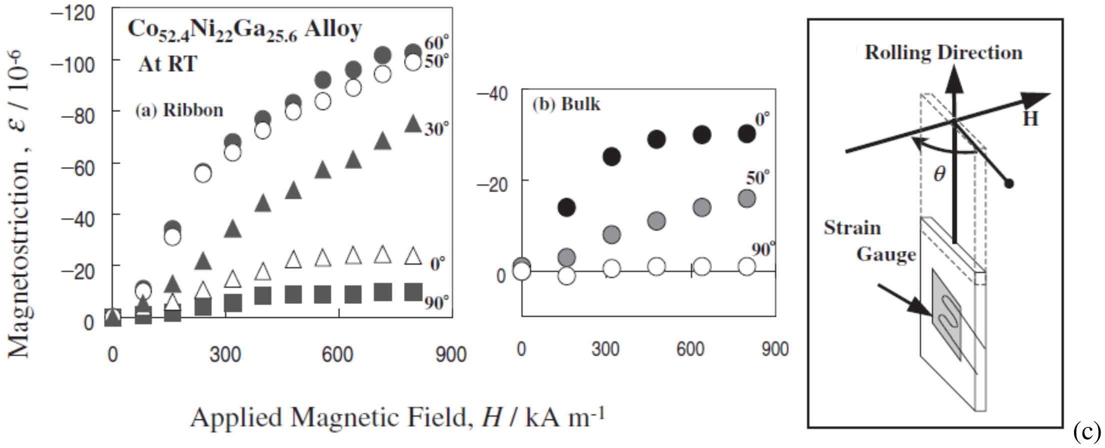

Fig. 33. $Co_{52.4}Ni_{22}Ga_{25.6}$ directional manetostriction measurement at room temperature of (a) ribbon sample, (b) bulk samples and (c) schematic of magnetostriction measurement method [82, 101]

Magnetostriction ε-H curves for the $Co_{50}Ni_{20}Ga_{30}$ ribbon at 200 K, which is reported by Zhang *et al.*, are shown in Fig. 34 [101]. Similar to the results reported by Sato *et al.* [82], the magnetostriction depended on θ, and exhibited a maximum value of 97 ppm shrinkage at θ= 60°,which is probably due to the texture of the ribbon induced by rapid solidification. At the same time, the transformation strain in the transverse direction was measured by Zhang *et al.*, and reported in the smaller amount than that in the longitudinal direction [101].

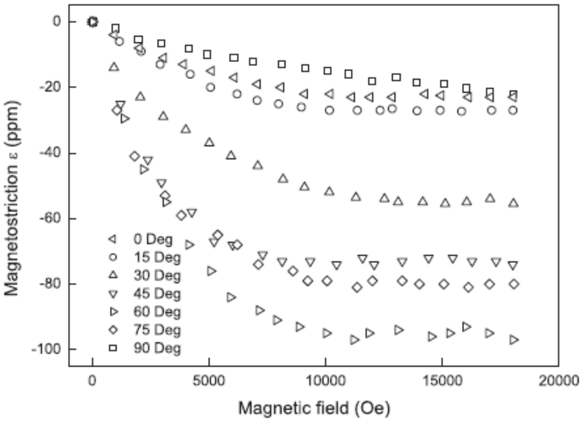

Fig. 34. $Co_{50}Ni_{20}Ga_{30}$ directional manetostriction measurement at 200K.

The temperature dependence of magnetostriction strain (ε) of the $Co_{52.4}Ni_{22}Ga_{25.6}$ ribbon has been shown in Fig. 35. Sato *et al.* reported that when temperature increases, the ε first increases and reaches to a maximum amount at 340 K, and then decreases rapidly at 370 K. Inversely, when decreasing temperature, the ε increases again and reaches a maximum at 353 K, and then decreases to the bottom value at 340 K. Consequently, they concluded that the magnetostriction is caused by rearrangements of the martensite twin variants activated in the temperature range below the austenite-phase starting temperature, A_s.

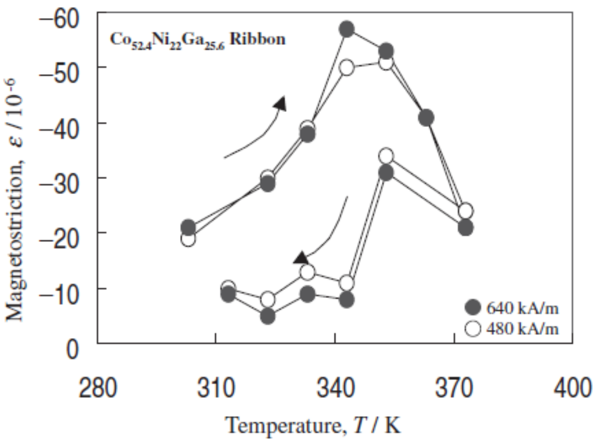

Fig. 35. Magnetostriction strain (ε) vs. temperature curves for the $Co_{52.4}Ni_{22}Ga_{25.6}$ ribbon.

1.2. Solidification Process

Typically, FSMAs are synthesized using the solidification process. The raw materials with high purity are arc-melted, homogenized, and quenched to obtain a martensitic structure [1, 7-18]. Processing of such FSMAs has currently concentrated only on the effect of elements and composition on their final FSM behavior. On the other hand, it should be noted that for a certain alloy composition, the final properties can be changed by manipulating processing parameters, such as bulk undercooling, solidification rate, and heat transfer condition during solidification. For example, it was found that the significant chemical segregation exists along the Ni-Mn-Ga ingot growth using Bridgman technique [19]. In addition, it has been reported that homogenization of FSMAs would take hours or days, which is undesirable in terms of cost and time [20]. These examples demonstrate the importance of processing parameters on FSMAs, and therefore, detailed study on processing parameters has to be accomplished.

It is known that transport phenomena at the microscale S/L interface during solidification dictates solutes distribution in solidifying alloys. For the case that limited diffusion in liquid and solid are assumed, solute atoms are rejected into the liquid ahead of the solidifying S/L interface according to its corresponding equilibrium partitioning coefficient value, k_e. Solute rejection into the liquid causes a solute boundary layer ($\delta_{o,i}$) forming (Fig. 36) [107, 108]. The magnitude of this boundary layer can be calculated using the following equation:

$$\delta_{o,i} = \frac{D_{o,i}}{V_{o,i}} \qquad \text{Eq. 5}$$

where $D_{o,i}$ is the interfacial diffusion coefficient of the liquid, and $V_{o.i}$ is the interface solidification velocity.

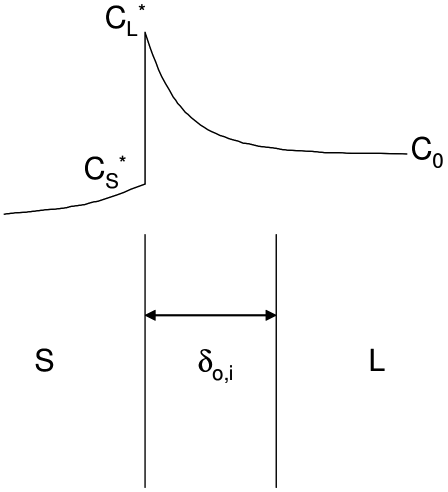

Fig. 36. A solute boundary layer of thickness, $\delta_{o,i}$ [108].

For near-equilibrium solidification in which the interfacial composition can be approximated using an equilibrium phase diagram, the solidification velocity (V_i) has to be small enough to allow for the compositional distribution at the S/L interface related to a K_e value. For a typical equilibrium solidification, the values for $D_{o,i}$ and $\delta_{o,i}$ are 2.5×10^{-9} m^2/s and 0.5×10^{-9} m, respectively [107], and the solidification velocity (V_i) is necessary to be equal or less than the $\frac{D_{o,i}}{\delta_{0,i}}$ ratio in Eq. 6, which is approximately 5 m/s in order to maintain the equilibrium condition at the S/L interface.

$$V_i \le \frac{D_{o,i}}{\delta_{o,i}} = V_{o,i} \qquad \text{Eq. 6}$$

On the other hand, an equilibrium condition at the S/L interfacial diffusion can no longer be existed if the solidification velocity or the inter-diffusion coefficient deviates from the equilibrium condition severely. In this case, a single term called an interfacial Peclet number (P_i) can be used to describe the boundary layer as follows:

$$P_i = \frac{\delta_{o.i} \cdot V_i}{D_i} = \frac{\delta_{o,i}}{\delta_i} \qquad \text{Eq. 7}$$

where V_i and D_i are the solidification velocity and the interfacial diffusion coefficient of a S/L interface for non-equilibrium condition, respectively.

Eq.7 suggests that an increase in the solidification velocity will result in a small solute boundary layer (δ_i) according to the Eq. 5, and hence, a large Peclet number. Diffusion coefficient is an intrinsic property of a material, and can be affected by convection or fluid flow. It was found that an increase in the convection in the liquid could decrease the boundary layer thickness [109].

1.2.1. Rapid Solidification (RS)

Rapid solidification of liquid alloys was first explored by Duwez [110], which opened a new era of metal processing. Rapid solidification not only can enhance solubility of alloys, but also it can result in formation of metastable phases and amorphous phases [110]. Rapid solidification has several special preferences compared to conventional solidification as follows: 1) large deviation from equilibrium composition and constitution resulting in substantial extensions of solid solubility and formation of new non-equilibrium crystalline phases and or amorphous phase, 2) more uniform and refined solidification microstructure widely eliminating detrimental effects of segregation obtained especially in thick sections, and showing more consistent response to heat treatment and working, 3) elimination of redundant working and finishing operations involved in ingot casting, by solidifying or consolidating to dimensions nearer to or identical to those actually required.

Rapid solidification is most readily achieved by imposing a high cooling rate e.g. 10^2-10^{10} K/s. Methods for achieving high cooling rate during solidification may involve fragmentation of a melt, heat extraction to a quenching fluid or by contact with a conducting chill surface. It may also involve rapid surface melting to a limited depth in situ on the substrate surface itself [111]. A variety of product forms are obtainable ranging from spherical, elongated or flake particulate to continuous fiber, ribbon or sheet to treated surfaces. Methods of consolidation are available that avoid degradation of intrinsic properties of the rapidly-solidified materials and, indeed, may enhance such properties by producing beneficial microstructural change thermomechanically.

Complete extension of solid solubility between terminal phases with the same crystal structure and partial extensions well beyond eutectic composition have been observed repeatedly [111]. The required formation of single-phase solids with the composition of the parent melt involves propagation of a morphologically stable front at sufficiently high velocity.

Microstructure effects are obvious in rapid solidification samples. Grain size, dendrite spacing and eutectic interphase separation all decrease with increasing cooling rate or front velocity according to power relationships derived theoretically and observed experimentally. Such relationships are frequently employed to estimate operative cooling rates or heat transfer coefficients from observed dendrite or eutectic spacing.

Lattice defects generated include additional excess vacancies that either collapse into dislocation loops or associate with solute atoms. High volume densities of planar defects (stacking faults or transformation twins) can also result in alloys prone to martensitic transformation during the quench. Such defects, together with solute clustering and the increased area of grain boundary per unit volume, can markedly influence hardening and precipitation behavior.

Coupled growth can be maintained to high front velocities in eutectic alloys but a large degree of undercooling can lead to formation of an extended solid solution, a new crystalline phase or a metallic glass (amorphous).

Rapid solidification has been applied for many metals and alloys to improve both individual and combinations of properties in conventional alloys, and to enhance thermal stability and elastic stiffness by means of nonconventional alloy additions that are actually detrimental at normal rates of solidification.

It has been recognized that bulk undercooling prior to solidification can lead to diverse solidification modes in metals and alloys, such as microstructural refinement, morphological change, solid solubility extension, partitionless (massive) solidification, and formation of alternate phases [63-66]. Bulk undercooling is also expected to result in improved properties of Co-Ni-Ga FSMAs, especially reducing or eliminating chemical segregation in these alloys. Moreover, bulk undercooling might lead to morphological change and/or new phase formation, which might provide an improved FSM behavior. Nevertheless, there is no available research conducting on the effect of bulk undercooling on the FSMAs, especially new coming Co-Ni-Ga alloys with a *Heusler-type* composition.

Various types of rapid solidification apparatus [112, 113] have been invented for exploring and synthesizing metals and alloys with unusual properties. The most common rapid solidification techniques being utilized these days are melt spinning, atomization, spray forming, laser surface melting and laser forming. These techniques rely on rapid heat extraction from the liquid through solidifying solid to enhance the S/L interfacial velocity. Thermal condition at the S/L interface also has significant effect on the S/L interfacial velocity.

It was found that the S/L interface velocity affects partitioning coefficient of alloys [115]. As proposed by Aziz in 1982 [114], the velocity-dependent partitioning coefficient (k (V_i)) can be described by the following equation:

$$k(V_i) = \frac{k_e + \left(\frac{\delta_{o,i} \cdot V_i}{D_i}\right)}{1 + \left(\frac{\delta_{o,i} \cdot V_i}{D_i}\right)} \qquad \text{Eq. 8}$$

Sobolev [116] proposed a similar relationship as that of Aziz, which is described using the following equation.

$$k(V_i) = \frac{k_e\left(1 - \frac{V_i^2}{V_D^2}\right) + \left(\frac{V_i}{V_{Di}}\right)}{1 - \left(\frac{V_i^2}{V_D^2}\right) + \left(\frac{V_i}{V_{Di}}\right)} \quad for\ V_i < V_D \qquad \text{Eq. 9}$$

$$and\ = 1 \qquad for\ V_i \geq V_D$$

where V_D and V_{Di} are the bulk and interfacial diffusion speed respectively.

Abbaschian and Kurz [115] also proposed similar velocity-dependent partitioning coefficient, where the relationship can be described by the following equation:

$$\frac{1 + k(V_i)}{2(1 - k(V_i))} \cdot \ln\left(\frac{k(V_i)}{k_e}\right) = P_i \qquad \text{Eq. 10}$$

Comparison between Aziz's and Abbaschian's models is shown in Fig. 37. Both relationships predicted that the partitioning coefficient approaches unity as the Peclet number increases. When the partitioning coefficient reaches unity, partitionless solidification occurs, where the interface composition on the solid (C_S^*) and liquid (C_L^*) sides are equal.

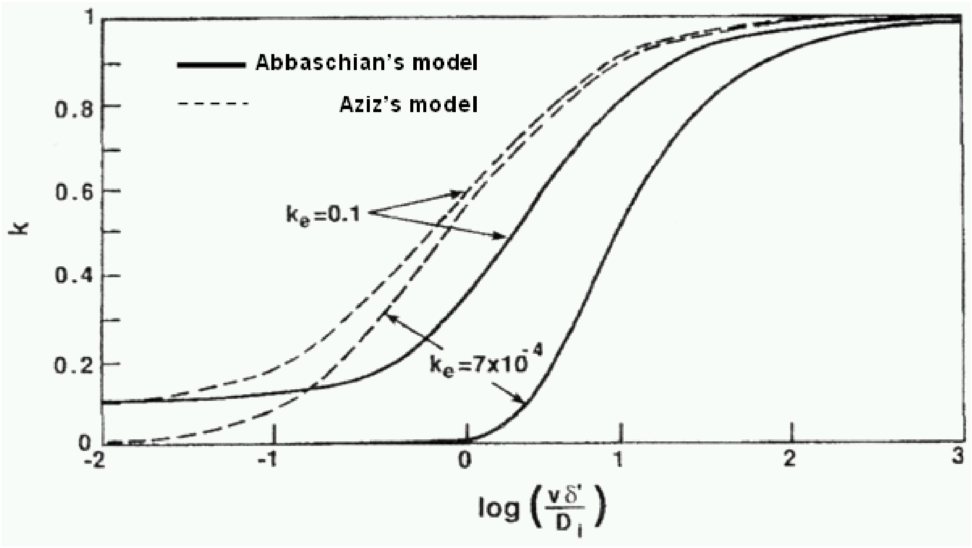

Fig. 37.Velocity-dependent partitioning coefficient predicted by Aziz's and Abbaschian's models [115]

1.2.2. Midrib Curve (T_0) and Partitionless Solidification

Solidus (T_S) and liquidus (T_L) curves in a phase diagram can be constructed from a series of C_S^* and C_L^*compositions as a function of temperature, where the chemical potential ($\mu = \left(\frac{\partial G}{\partial X}\right)_{T,P}$), the slopes of the free energy-composition (*G-X*) curves of liquid and solid are equal (Fig. 38). Similarly, a series of C_m compositions, where the liquid and solid phases have the same free energy can be constructed known as a midrib curve (T_0). The midrib curve has a technological importance for rapid solidification processes, and the detail on this particular topic can be found elsewhere [117]. For the liquid of the composition between T_S and T_0 curves, there is a chance that the liquid can transform into solid of the same composition, which is corresponding to the *k* value of 1. The theoretical study by Boettinger [64, 118] showed that T_S and T_L curves converge to a single line but below T_0 curve at high solidification velocities indicating that rapid solidification processes can enhance the homogeneity of solidified alloys by reducing chemical segregation.

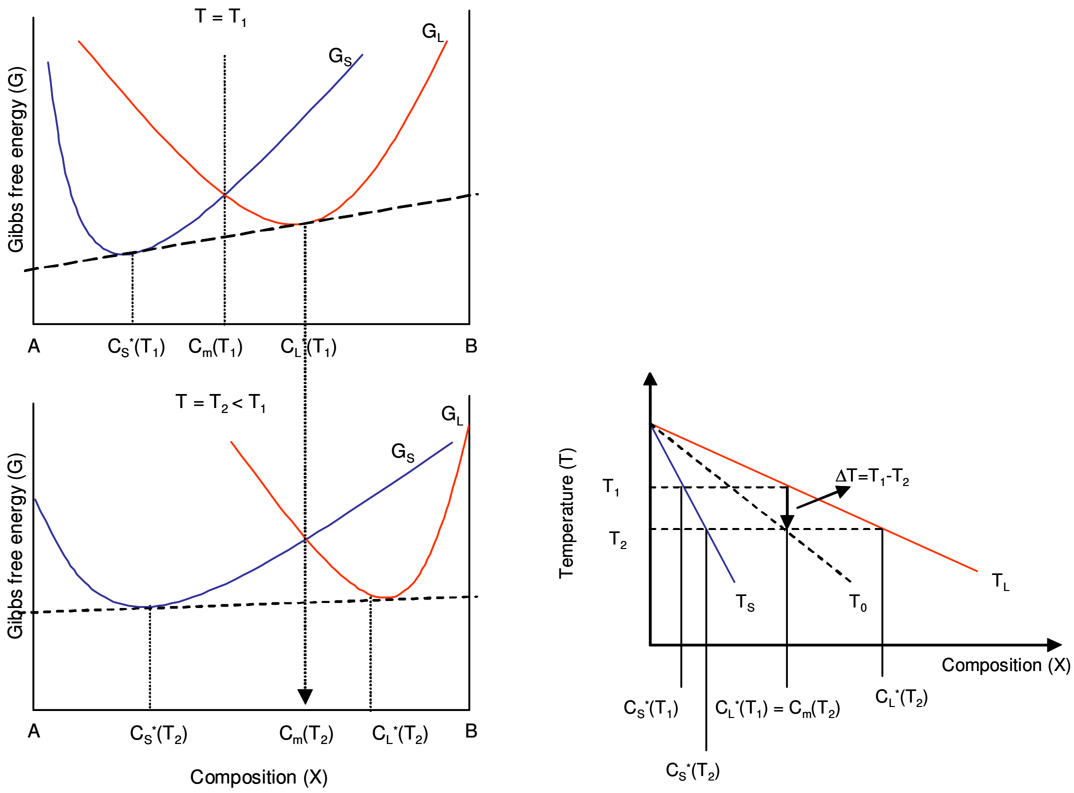

Fig. 38. A schematic demonstrates the mechanism of solute trapping [119]

As mentioned before, rapid solidification mostly enhances the solubility in several alloys that do not exhibit significant separation between liquidus and solidus curves. This is because at high solute content, the temperature difference between T_L and T_0 curves increases and it is more difficult for the S/L interfacial temperature to be maintained below T_0, where partitionless solidification can take place [64, 118]. Most rapid solidification techniques are, therefore, limited by the rate of external heat extraction and the thickness of the material being processed [120], which prevents production of a large-dimension specimen. There have been attempts to enhance solubility of Ga in Co-Ni-Ga through rapid solidification processes particularly using melt spinning [121]. Nevertheless, there were indications from samples solidified by laser melting or splat cooling that such processes can lead to extremely fine distribution of one phase in the other due to dynamic supercooling.

1.2.3. Interfacial versus Bulk Supercooling

1.2.3.1. Interfacial Supercooling

Liquid is said to be in a supercooled state if its temperature is brought below the equilibrium melting temperature. Below an equilibrium melting point, the free energy of liquid is normally higher than that of other phases (Fig. 39).

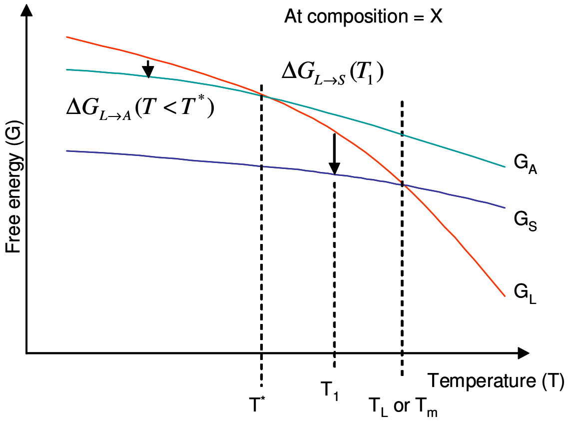

Fig. 39. The free energy-tempearture (G-T) curves at a constant composition demonstrate possible phase transformations of supercooled liquid.

In general, small amount of supercooling (ΔT) is required as a driving force for solidification ($\Delta G_{L\rightarrow S}$), which can be approximated using the following equation [122]:

$$\Delta G_{L\rightarrow S}(T) = \frac{\Delta H \cdot (T_m - T)}{T_m} = \frac{\Delta H \cdot \Delta T}{T_m} \qquad \text{Eq. 11}$$

where ΔH is the heat of solidification, T_m is the melting temperature and T is the supercooled temperature.

Supercooling, a major driving force in the solidification process, can be obtained due to several effects, such as curvature (ΔT_r), kinetic (ΔT_k), pressure (ΔT_p), constitutional (ΔT_c) and thermal (ΔT_t) [109]. Supercooling due to the first three effects normally influences the solidification around the S/L interfacial region known as interfacial supercooling. Curvature, kinetic and pressure supercoolings are typically small (2 K for r= 0.1 µm for ΔT_r, 0.01 to 0.05 K for ΔT_k and 10^{-2} K/atm for ΔT_p). On the other hand, constitutional supercooling resulting from the existence of a solute boundary layer ahead of the S/L interface can be a few or several degree depending on the difference between the equilibrium liquidus profile and the temperature gradient ahead of the interface, which can be approximately calculated using the following equation [109]:

$$\Delta T_c = -m(C_L^* - C_0) \qquad \text{Eq. 12}$$

where m is the slope of a liquidus line, C_L^* is the composition of liquid at the interface on the liquid side, C_0 is the composition of the bulk liquid.

Nucleation of a new phase from liquid can take place by three different mechanisms; homogeneous, heterogeneous and dynamic nucleation [107]. Homogeneous nucleation of a new phase is mentioned to occur on a nucleation site of the same chemistry, while heterogeneous nucleation requires nucleation sites of different chemistry to that of a new phase. Heterogeneous nucleation can be also divided into continuous and instantaneous mechanisms [107]. The last mechanism called dynamic nucleation, which takes place under the dynamic conditions of liquid, can be subdivided into two mechanisms; the big bang and the crystal fragmentation mechanisms. The big bang mechanism involves the pre-dendritic nuclei formed during pouring by the initial chilling action of the mold. These nuclei survive and mix with the liquid. The latter mechanism is similar to the first one but nuclei are parts of detached dendrite arms.

Nucleation of a solid phase depends on the wettability between the phase and the nucleating site; the smaller the dihedral angle, the smaller the geometrical factor and the better the wettability is. Homogeneous nucleation, where a new phase nucleates within a liquid itself, will take place if the geometrical factor is equal to one.

The driving force for overcoming the nucleation barrier of a solid phase (ΔG^*) can be related to supercooling as [122]:

$$\Delta T = \left[\frac{16}{3} \frac{\pi \sigma_{S/N}^3 V_S T_m^2}{\Delta H_f^2 \Delta G_{L \to S}^*} S(\theta) \right]^{1/2} \qquad \text{Eq. 13}$$

where $\sigma_{S/N}$ is a surface energy between a nucleating phase and an active nucleation site, V_S is a molar volume of a nucleating phase, $S(\theta)$ is a geometrical factor depending on θ, the wetting or dihedral angle between a nucleating phase and an active nucleation site. θ varies from 0 to 180°, and can be calculated using the Young's equation [122]:

$$\cos\theta = \frac{\sigma_{L/N} - \sigma_{S/N}}{\sigma_{S/L}} \qquad \text{Eq. 14}$$

1.2.3.2. Bulk Supercooled Liquid

Liquid is one of the three principal states of matter. Metastable liquid, an unusually state of liquid said to be in superheated or supercooled states can be found in industrial processing and manufacturing plants, and some natural phenomena like clouds [123].

A liquid can experience a considerable thermal and bulk supercooling before the nucleation of a solid phase. In unusual cases, metastable transformations of liquid can take place if the liquid experiences a considerable thermal supercooling; bulk supercooling and the formation of an equilibrium phase is suppressed [123]. For example, the liquid (*L*) can transform into an "A" phase at below T^* if it is supercooled for at least T_m-T^* degree, and no preferential nucleation site for a solid (*S*) phase exists (Fig. 39) [119].

The difficulty of obtaining large supercooling in metals and alloys for conventional processing is associated with active nucleation sites, such as container surface and impurities, which can result in a small value of the geometrical factor $S(\theta)$, and can reduce the ability for getting high degree supercooling. In general, the following approaches can be used to achieve a large supercooling in a liquid: 1) High purity materials as raw materials are used to minimize possible impurities; 2) Since the probability of finding impurities is proportional to the volume of liquid, dispersion of liquid into a large number of small droplets is needed; 3) Utilization of a non-reactive crucible material or cotainerless processing may be required [119].

There are several techniques to achieve large bulk undercooling in a melt, such as emulsification [67], glass fluxing method [68], Electromagnetic Levitation (EML) [69], and recently developed Electrostatic Levitation (ESL) [70]. A summary for these techniques has been given in Table 2. Among these techniques, EML and ESL are most favorable techniques since they provide controllable and large undercooling of a bulk specimen [124].

Table 2. Available techniques for obtaining bulk supercooling in liquid metals and alloys

Technique	Bulk Supercooling	Typical Specimen	Process Description
Atomization	Yes	Powder	Liquid stream is injected through the cooling medium (gas or liquid)
Drop tube	Yes	Droplets	Free-fall in an atmospheric controlled tower
Emulsification	Yes	Droplets	Specimen is injected into a denucleating agent (non-wetting liquid)
Electromagnetic Levitation (EML)	Yes	7-mm sphere	Good for paramagnetic and diamagnetic materials with a good electrical conductivity. Levitation coil is critical. Magnetic force stabilizes as well as heats the specimen. Levitation-Heating dependent
Electrostatic Levitation (ESL)	Yes	< 2 mm sphere	Positive charge is generated on the specimen using high-energy UV-light. Negative-charge plates stabilize the sample. Levitation-Heating independent
Melt Fluxing	Yes	Droplets	Specimen is encapsulated in a denucleating agent (non-wetting solid).

These techniques can be used to melt and undercool metallic and non-metallic (only for ESL) specimens without physical contact with container wall. In addition, a bulk specimen can be cyclically melted, undercooled, and subsequently solidified. Particularly, EML can be used to process a moderate specimen size of approximately 7-mm diameter compared to that of ESL, where the specimen size is less than 1 mm [124]. Therefore, the EML technique is suitable for the current study.

Furthermore, a specially designed quenching system is proposed in this study. Such system will allow one to quench the levitated specimen at any moment during levitation. In addition, this special quenching system will provide various cooling rates from low to ultra-high rates depending on the mold geometry and materials as well as quenchant media used. The combination of the electromagnetic levitation and a specially designed quenching system would be an ideal approach for investigating the effect of undercooling and cooling rate on microstructural evolution in Co-Ni-Ga FSMAs.

1.2.4. Electromagnetic Levitation Melting for a Containerless Processing

Electromagnetic field has been utilized in several materials processing, particularly induction melting [125]. In EML melting, magnetic field is employed to generate magnetic force on a conducting specimen. Magnetic field then induces currents within the surface of the specimen due to skin effect, and results in heating of the specimen. The application of the EML for heating and melting metals without crucible was accomplished in 1952 by Okress *et al.* [126]. Two sets of coils were used to stabilize a specimen as shown in Fig. 40.

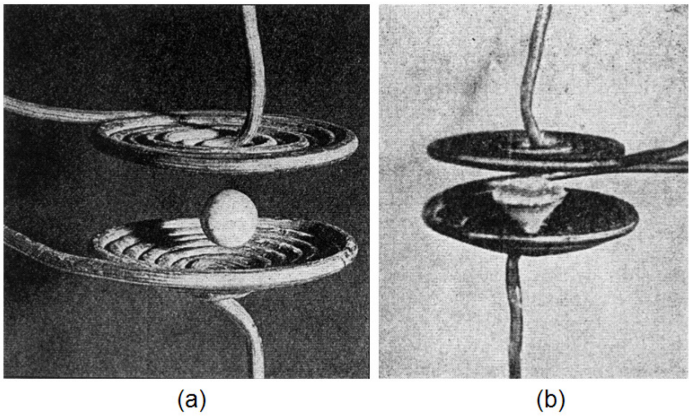

Fig. 40. A coaxial levitation coil first used for containerless processing of metals [126] (a) the solid sphere, and (b) the sphere in a molten state

In 1983, the first analytical study on the physical behavior of the EML melting was done by El-Kaddah [127]. Until dates, EML melting has been a useful tool for the investigation of various supercooled alloys. The design of a levitation coil has a major impact on the magnetic force, heating, and cooling rate of the specimen [124]. It was demonstrated that a coil with the shape displayed in Fig. 41 is effective [124]. For this particular design, a specimen can be levitated within a quartz tube, which is inserted into a coil providing a controlled atmosphere for vacuum, inert gas or process gases i.e. Ar + 5% H_2 as shown in Fig. 41.

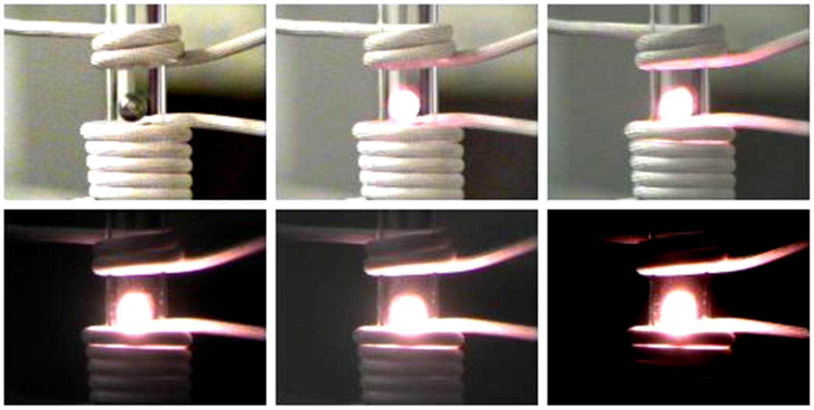

Fig. 41. A series of pictures demonstrate levitation and melting process of a specimen in EML system.

The AC current is used to generate a magnetic field around the coil. The magnetic field can induce inductive currents within the surface layer of the depth of the specimen, δ, known as a skin effect [128] as described by the following equation:

$$\delta = \frac{1}{\sqrt{\frac{1}{2}\omega\sigma\mu}} \qquad \text{Eq. 15}$$

where ω is the angular frequency of the applied field, σ and μ are the conductivity and the magnetic permeability of the specimen, respectively.

Instantaneously, the inductive currents produced within the skin depth interact with the applied magnetic field from the levitation coil resulting in “Lorentz forces” acting toward the specimen as described by the following equation:

$$F_{Lorentz} = q\vec{V} \times \vec{B} \qquad \text{Eq. 16}$$

where $q\vec{V}$ is the analogous to the inductive current generated on the specimens surface, and $\vec{B}$ is the magnetic field generated by the levitation coil.

Depending on the electrical and magnetic properties and the size of the specimen, the levitation coil has to be designed in such a way that the levitated specimen can be stabilized throughout the levitation process. For more details on the operating theory of the electromagnetic levitation system, the information can be found in reference [126]. It was numerically demonstrated by EL-Kaddah [127] and Li [129] that temperature difference in levitated specimens of the diameter between 5 to 9 mm were less than 5 degrees. Nevertheless, the fluid flow velocity within an EML specimen is quite severe.

Due to a containerless nature of the technique, the EML technique can provide bulk supercooling to the liquid by eliminating the heterogeneous nucleation sites due to a container wall. In addition, the chance of heterogeneous nucleation within a liquid during the EML experiment can be minimized by supplying reducing gases such as hydrogen and argon mixes. These gases prevent the formation of inclusions that can result in heterogeneous nucleation, which decreases supercoolability of the liquid.

There have been several early studies on metals and alloys using EML system to investigate the effect of undercooling on microstructural evolution accomplished by Kattamis, Abbaschian and Flemings [130-132]. Following them, many other research groups have applied this technique for different metals and alloys systems. For example, Zhang [133] did EML experiments on Fe-Cr binary system of 4 different compositions (5, 10, 15 and 20 wt% Cr). In his study, the maximum undercoolings of larger than 280 K were observed. It was found that the microstructures of levitated samples varied with the degree of undercooling. For undercooling smaller than about 180-200 K, a dendritic solidification was obtained. At increased undercoolings, the microstructures were changed to cellular and microsegregate-free microstructures (Fig. 42).

Leonhardt *et al.* [134] studied Ni-Nb system using the EML. Specimens of average sizes of 6 mm were levitated and solidified at different undercoolings. Interesting features were observed when Ni-16 wt% Nb specimens were undercooled at different levels. The maximum undercooling of 276 K was achieved in their study. The examples of microstructures reveal the tendency of a weakly segregated twined α-Ni microstructures at high undercooling compared to a dendritic structure at low or no undercooling (Fig.

43). This example clearly exhibits the enhancement of metastable microstructures due to an implement of undercooling before rapid solidification takes place.

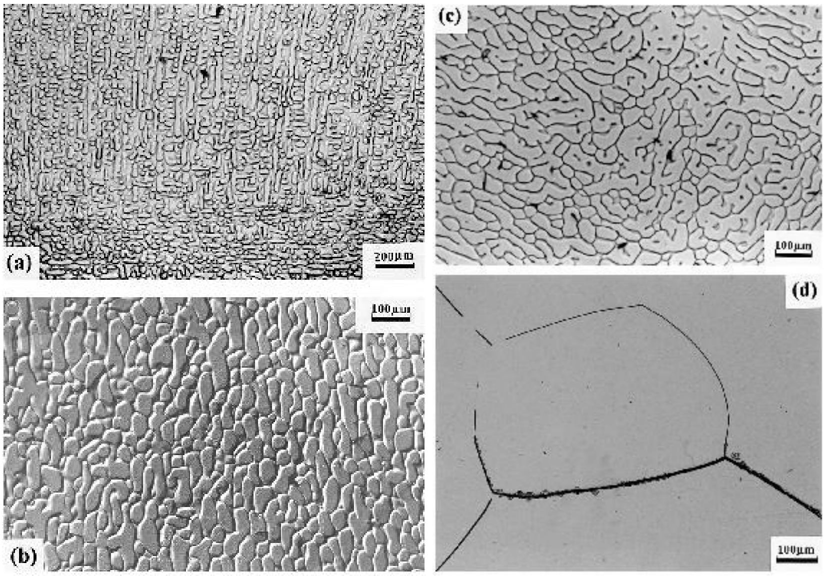

Fig. 42. Microstructure of Fe-10Cr alloy solidified at different undercoolings. (a) $\Delta T = 125$ K, dendritic microstructure; (b) $\Delta T = 200$ K, cellular microstructure; (c) $\Delta T = 230$ K, cellular microstructure; (d) $\Delta T = 315$ K microsegregation-free microstructure [133].

Kral *et al.* [135] compared their EML experiments on Ti + rare earth elements with other rapid solidification techniques. It was found that the EML technique allowed large bulk liquid undercoolings of 200 K in Ti-1.4 at% Ce, Ti-1.7 at% Er and Ti-1.5 at% La prior to rapid solidification by splat quenching. The resulting microstructures were found to be different from those obtained directly by melt spinning, laser surface melting and splat quenching without prior undercooling. The microstructures of the alloys in their study exhibited a distribution of elemental rare earth nanosize-precipitates within regularly-spaced planar or curved sheets throughout and equiaxed α-Ti matrix (Fig. 44).

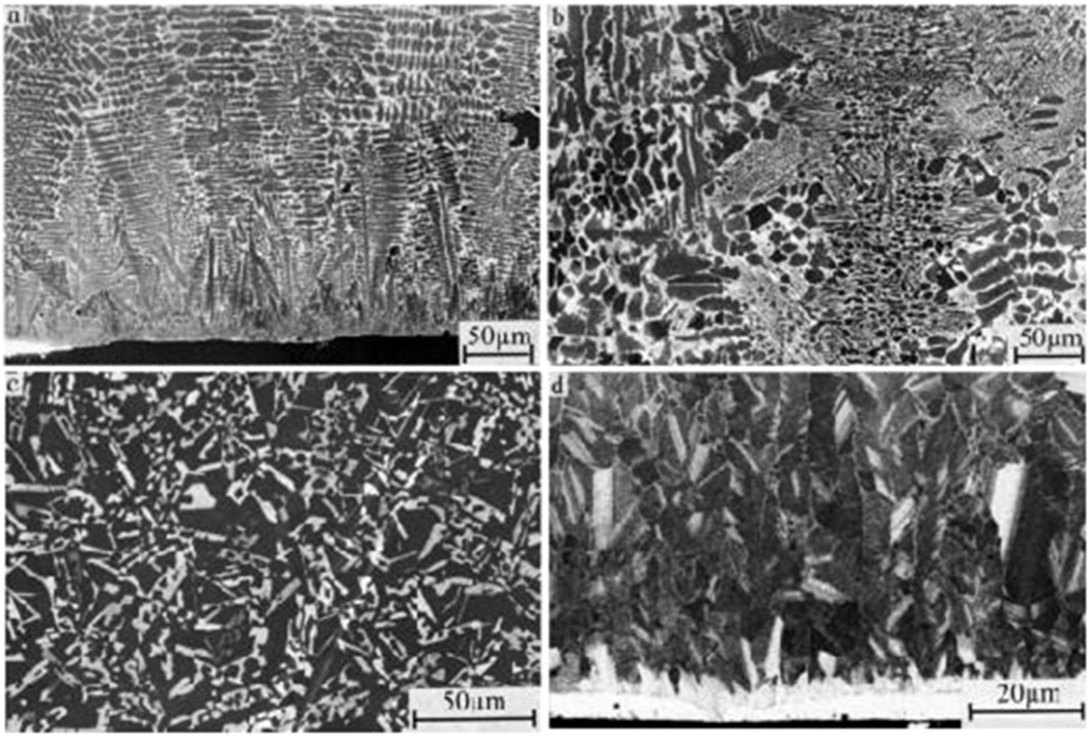

Fig. 43. Cross-sectional SEM micrograph of as-solidified Ni 84 Nb 16 samples for different undercooling levels prior to solidification and post-solidification cooling, respectively: (a) ΔT ‹ 70 K, quenched on a Cu substrate (bottom): metastable α-Ni dendrites (dark); (b) ΔT ‹ 70 K, central part of the sample quenched on a Cu substrate: dendritic microstructure along with lamellar eutectic [α-Ni (dark) +Ni 3 Nb (bright)] cells in interdendritic regions; (c) ΔT ‹ 160 K, gas cooled: anomalous eutectic α-Ni+Ni 3 Nb microstructure; (d) ΔT ‹ 240 K, quenched on a Sn-coated substrate: Ni Nb phase layer (bright) near the chill substrate interface (bottom) succeeded by a weakly segregated twinned α-Ni microstructure (greyish) [134].

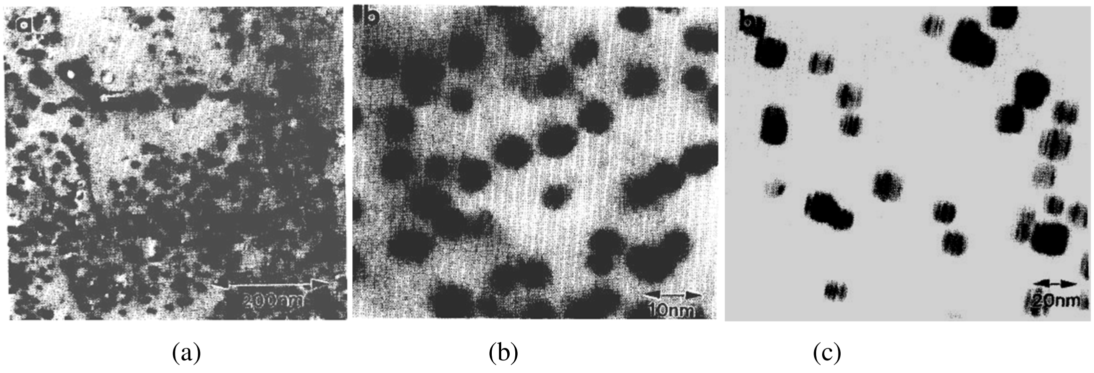

(a) (b) (c)

Fig. 44. TEM micrographs of (a) Ti-1.4Er (b) Ti-1.7Ce and (c) Ti-1.5La undercooled about 200 K before splat quenching [135]

According to undercooling studies in several alloy systems, it can be seen that EML technique is very promising for exploring the undercooling effect on Co-Ni-Ga FSMAs. It is also expectable that undercooling would result in desirable microstructural evolution and hence the improvement in FSM behavior in such alloys.

1.3. Co-Ni-Ga Ternary System

1.3.1. Crystal Structures of Co-Ni-Ga

Back in 2001, the Co-Ni-Ga FSMA with the stoichiometry in the vicinity of Co_2NiGa was first discovered by Wuttig *et al*. [16], and later developed by Oikawa *et al* [12, 99]. Nevertheless, there is no complete information on this ternary system. However, one could explore the Co-Ni-Ga system by investigating Co-Ni, Co-Ga, and Ni-Ga binary diagrams [136, 137] The Co-Ni alloys are well known as ferromagnetic materials. For Co-Ni alloys at all compositions, the alloys will form a solid solution (αCo, Ni) with A1 structure (face-centered cubic (cF4, Fm3m)) (Fig. 45).

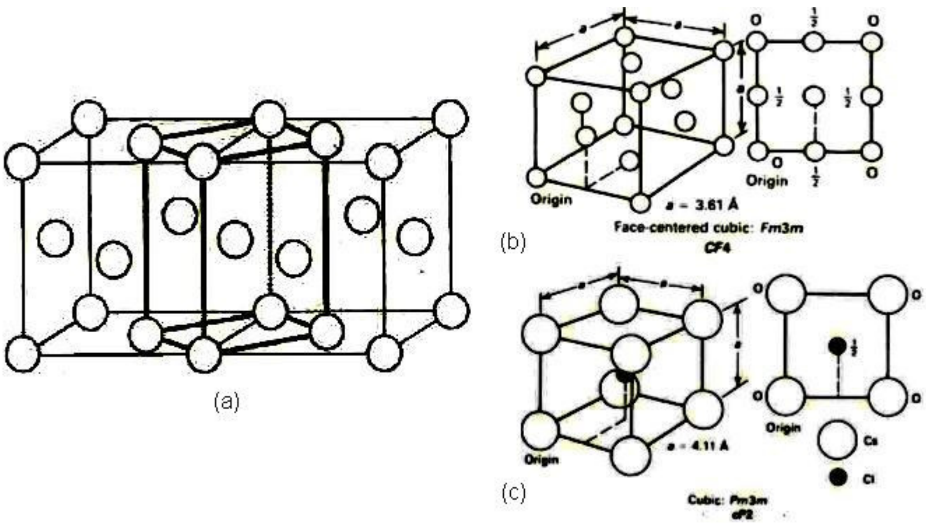

Fig. 45. (a) BCC in FCC structure [59] (b) cF4 (FCC structure) [138] (c) cP2 (BCC structure) [138]

Upon introducing Gallium of a certain amount into either Co or Ni, it can stabilize β-phase with B2 structure (Fig. 46).

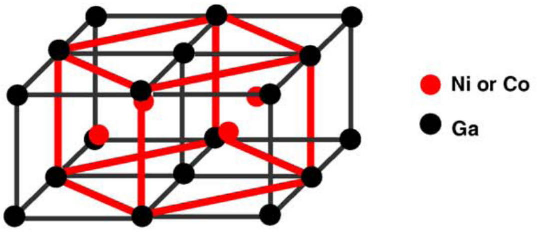

Sketch of transformation from β (B2) to Martensite ($L1_0$)

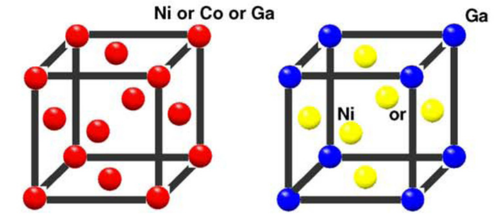

Crystal structure of γ (A1)   Crystal structure of γ′ ($L1_2$)

Fig. 46. The bcc parent phase undergoes to the fct martensite based on Bain model [137]

The compositional ranges for β-phase formation in Co-Ga and Ni-Ga binary systems are 33 to 66.7 wt% Ga and 34.2 to 62 wt% Gab, accordingly (Fig. 4747). Craciunescu *et al.* [17] suggested that the β-phase solid solution of Co-Ni-Ga alloys with $L2_1$ crystal structure (Fig. 47) could be obtained from the compositional range in each binary phase diagram of Co-Ga and Ni-Ga. After that, a conjectural ternary phase diagram at room temperature, which is made out of the Co-Ni, Co-Ga and Ni-Ga binary diagrams (Fig. 47), introduced by Liu *et al.* [137]. The β phase region in this ternary phase diagramat room temperature has been shown in Fig. 47. They also developed this ternary phase diagram based on their experimental results for isotherms near Co_2NiGa at 1150 and 800°C.

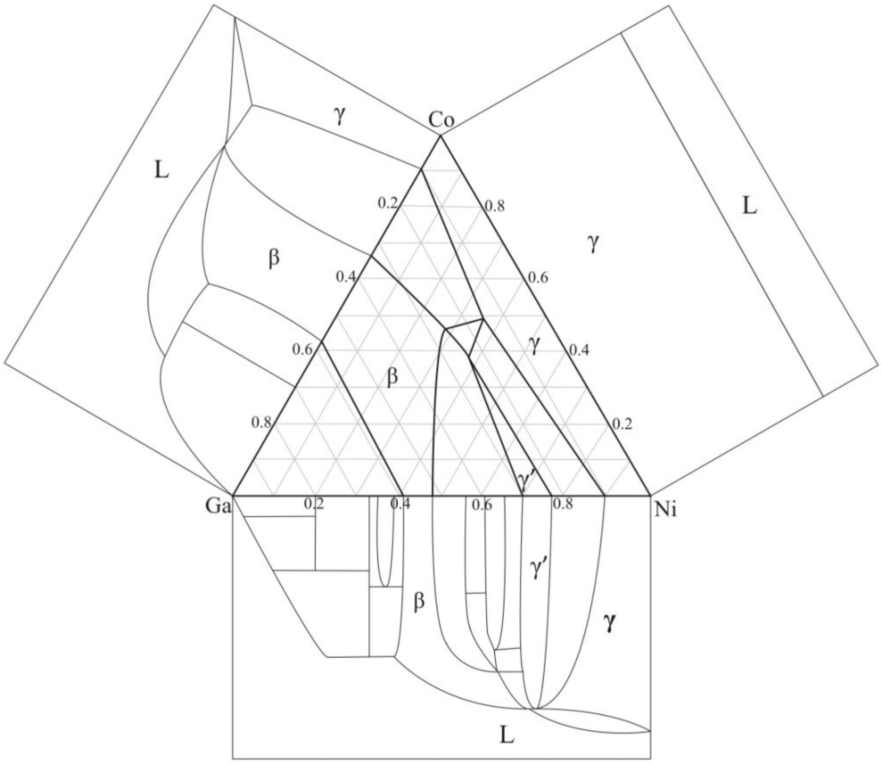

Fig. 47. (a) A β-phase region and two-phase area in Co-Ni-Ga ternary system at room temperature projected from binary diagrams [137-139].

Similar to the Ni-Mn-Ga alloy system, Co-Ni-Ga with a *Heusler-type* composition of Co_2NiGa or approximately 32.18 wt% Co-31 wt% Ni-36.82 wt% Ga would give a β-phase with B2 structure upon a proper heat treatment. The B2 structure consists of two different occupied sublattices with the sites of the first sublattice being positioned in the center of the unit cell of the second one (Fig. 46) and vice versa [140].

The extrapolation of the stability regions of bcc-type B2 phases of the binary Co-Ga and Ni-Ga alloys suggests that ternary compositions with a bcc lattice structure, which may transform martensitically, might exist in the vicinity of the stoichiometric composition [17, 141]. Fig. 48 indicates the Co-Ni-Ga phase diagram showing the martensitic phase at room temperature with the isothermal room-temperature martensite start temperature *Ms* (T_R) represented in the isothermal section of 1000°C, constructed from the data in Ref. [142]. The isothermal section shows the equilibrium fcc- and bcc-like phases, γ (A1), γ' ($L1_2$), and β (B2), respectively, as well as the two-phase field $\gamma+\beta$ region. Tetragonal β' ($L1_0$) corresponds to the martensitic structure. The extrapolated B2 phases (dashed triangle) show the favorable overlapping regions at 0°C for the formation of the Ferromagnetic Shape Memory (FSM) $L2_1$-like *Heusler* structures [17]. The yellow (gray in black and white version) dot marks the perfect $L2_1$ Co_2NiGa compound on the dashed line of constant e/a= 7.75. The second dashed line of constant e/a= 7.42 goes through the white square corresponding to completely disordered β-phase $Co_{48}Ni_{22}Ga_{30}$ ($Co_{1.92}Ni_{0.88}Ga_{1.2}$). First principles phonon calculations were done by Siewert *et al.* [141] for $L2_1Co_2NiGa$, $Co_2Ni_{0.75}Ga_{1.25}$ and $Co_{1.75}NiGa_{1.25}$. The latter are represented by white circles. The regions with Curie temperatures, T_c, larger or smaller than the martensite transformation temperatures, *Ms*, are separated by the thick blue line (thick black dashed line in black and white version) [99].

Experimental characterization reveals, however, that in order to obtain pure β (bcc) phases, a Ga content of at least 30 at% is required, while at the stoichiometric composition, a rather mixture of segregated β (B2-bcc) and γ (A1-fcc) phases is found. This narrows the range of martensitically transforming compositions since with increasing Ga content (and thus decreasing e/a) the martensitic transformation temperatures decrease. A similar behavior is obtained if Ni is replaced by Co. As a limit for nonvanishing martensite transition temperatures $e/a\approx$ 7.3 was proposed in the past

[17]. On the other hand, the Curie temperatures show the opposite trend with increasing Co content, which means that a sufficient amount of Co is necessary to stabilize the ferromagnetism at appropriate operating temperatures. This dramatically narrows the range of compositions in which alloys with suitable FSM properties can be found.

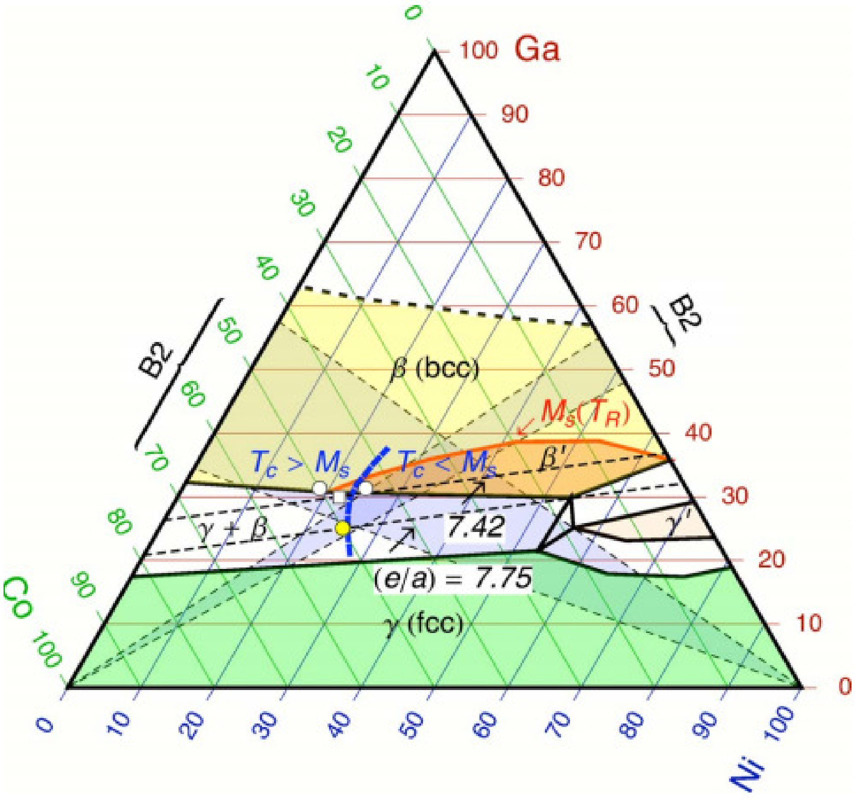

Fig. 48. The Ga-Co-Ni phase diagram for the martensitic phase at room temperature with the isothermal room-temperature martensite start temperature *Ms* (T_R) represented in the isothermal section of 1000°C [141].

Apart from the composition, the distribution of the atoms on the sublattices can play an important role for phase stability. While first studies considered a $L2_1$ full *Heusler* ordering for Ni2MnGa (Fig. 49) [143], later experimental studies reported Co-Ni-Ga alloys with a disordered B2 structure.

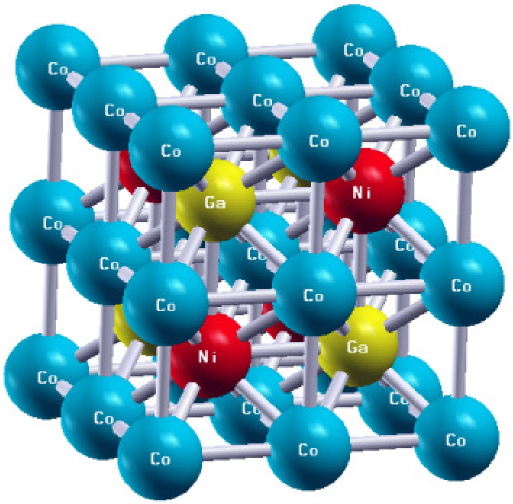

Fig. 49. The Co_2NiGa cubic crystal structure $L2_1$ with four interpenetrating face-centered cubic sub-lattices [141].

As mentioned earlier, the B2 structure consists of two interpenetrating disordered sublattices, which are occupied with different elemental ratios. This may delicately depend on the preparation conditions, which vary in order to avoid $\beta+\gamma$ phase separation.

1.3.2. Solidification and Microstructure of Co-Ni-Ga

In general, the solidification route of a ternary alloy could be predicted if the liquidus surface contour of the ternary phase diagram is known. The liquidus surface contour of a Co-Ni-Ga alloy (Fig. 47) can be visualized using the binary diagrams. There are three possible paths for conventional solidification depending on the curvature of the surface contour and composition, as schematically shown in Fig. 50. One path, although less likely, would lead directly to the formation of a Ga-rich liquid at the end of solidification, while the two others paths lead first towards Ni- or Co-rich regions, and then towards the Ga-rich liquid. Because of either of these solidification paths, conventional solidification techniques of the alloy cannot only lead to severe chemical segregation, but also grain boundary embrittlement. Such microsegregation and non-homogeneity strongly influence the martensitic transformation. As such, it is generally necessary to homogenize the alloy, which requires long time and high temperatures.

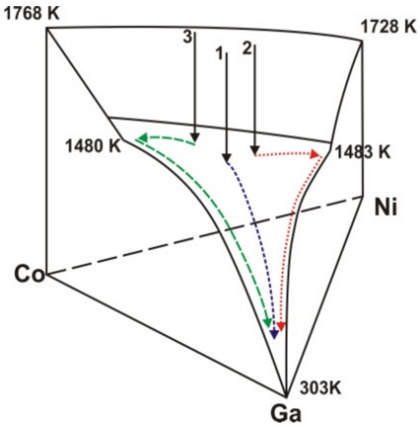

Fig. 50. Three possible solidification routes; toward (1) Ga-rich, (2) Ni-rich and or (3) Co-rich regimes for Co-Ni-Ga alloys with compositions in the β-phase region.

According to the Co-Ga and Ni-Ga phase diagrams, the solidification routes for the starting liquids (L_0) with the compositions projected from the *Heusler* regime can be shown as follow.

Co-Ga:

$$L_0 \xrightarrow{T} \beta + L_1 \xrightarrow{838 \pm 10\,^{\circ}C} \beta + CoGa_3 + L_2 \xrightarrow{29.7741\,^{\circ}C} \beta + CoGa_3 + Ga$$

Ni-Ga:

$$L_0 \xrightarrow{T} \beta + L_1 \xrightarrow{895\,^{\circ}C} \beta + Ni_2Ga_3 + L_2 \xrightarrow{252\,^{\circ}C} \beta + Ni_2Ga_3 + NiGa_4 + L_3$$
$$\xrightarrow{29.7441\,^{\circ}C} \beta + Ni_2Ga_3 + NiGa_4 + Ga$$

It can be seen that such solidification routes will result in significant chemical segregation in an ingot grown by a single crystal growth technique.

FSMAs are synthesized using an arc-melting process [1, 7-18]. The specimen prepared by the arc-melting is then heat treated to obtain martensitic structure. Recently, Kishi *et al*. [18] attempted to synthesize the Co-Ni-Ga FSMAs using melt-spinning technique. It was found that the FSM behavior is improved in melt-spun Co-Ni-Ga FSMAs compared to a bulk counterpart. The rapidly solidified samples indicate the saturation magnetization at less than 70 KOe compared to 5 KOe in bulk samples. This reveals the improved sensitivity of FSM behavior due to the implementation of rapid solidification process. In addition, the FSM behavior was obtained in as-received melt-spun Co-Ni-Ga without a further heat treatment. On the other hand, if the liquid alloys with the compositions in the regime described previously are undercooled below the solidus temperature, it is possible to obtain a homogeneous β-phase alloy due to partitionless solidification without an extensive homogenization. Normally, to obtain a martensitic (β') phase, the β-phase solid solution is quenched from a homogenizing temperature. This step could be eliminated if the undercooled liquid is rapidly solidified in a selected quenching medium. Quenching of an undercooled liquid in the electromagnetic levitation system is possible by using a special quenching system proposed in this study.

Another significant improvement of ductility in FSMAs, especially in Co-Ni-Ga system is due to the presence of γ-phase in β' matrix (Fig. 51) at some compositional range within a *Heusler-type* regime [12]. The improved ductility because of the γ-phase might be due to the fact that the γ-phase possesses A1 structure (cF4, Face-centered cubic); a ductile phase. The aspect of improved ductility in Co-Ni-Ga are also investigated in the present study.

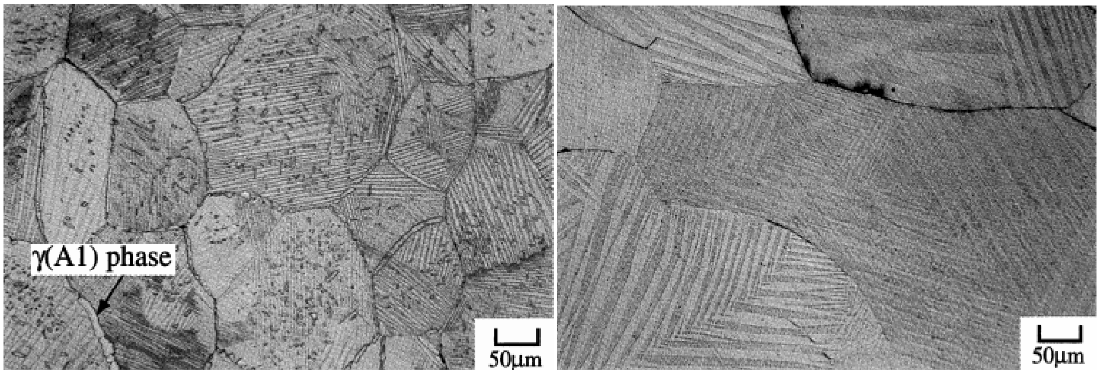

(a) (b)

Fig. 51. Precipitation of γ-phase in β'-matrix (a) results in improved ductility in Co-Ni-Ga FSMAs [12] (b).

The microstructure of Co-Ni-Ga alloys is important to see the range of β and/or γ equilibrium phase at room temperature. As mentioned before, the morphology and volume fraction for each phase strongly depend on the composition and cooling rate.

1.4. Characterization of FSMAs

1.4.1. Vibrating Sample Magnetometer (VSM) Systems for Magnetic Characterization

Vibrating Sample Magnetometer (VSM) systems are used to measure the magnetic properties of materials as a function of the magnetic field, temperature, and time. They are ideally suited for research and development, production testing, quality and process control. Powders, solids, liquids, single crystals, and thin films are all readily accommodated in a VSM. If a material is placed within a uniform magnetic field H, a magnetic moment M will be induced in the sample. In a VSM, a sample is placed within suitably placed sensing coils, and is made to undergo sinusoidal motion, i.e., mechanically vibrated. The resulting magnetic flux changes induce a voltage in the sensing coils that is proportional to the magnetic moment of the sample. Variable temperatures may be achieved using either cryostats or furnace assemblies.

In the case of a typical FSMA, the hysteresis loop gives the relation between the magnetization M and the applied field H. A hysteresis loop of a magnetic medium is illustrated schematically in Fig. 52.

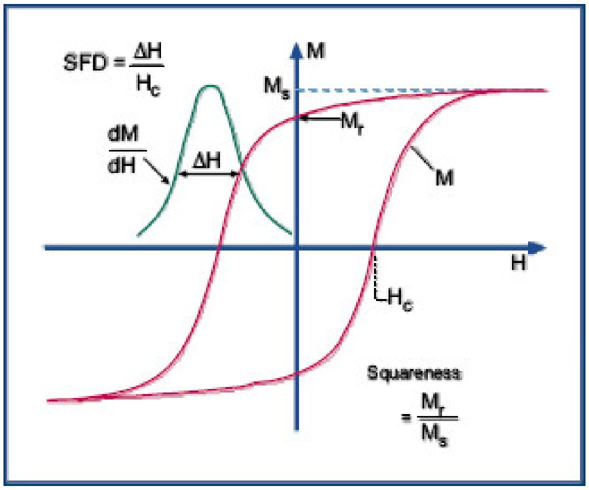

Fig. 52. The parameters in hysteresis loop that characterize the magnetic properties of FSMA [144]

The parameters extracted from the hysteresis loop that are most often used to characterize the magnetic properties of magnetic media include: the saturation magnetization (*Ms*), the remanence (*Mr*), the coercivity (*Hc*), the Squareness Ratio (SQR), *S**, which is related to the slope at *Hc*, and the Switching Field Distribution (SF). The loop illustrated in Fig. 52 shows the behavior for the easy axis of magnetization (i.e., in the anisotropy direction) [144]. The loop has a rectangular shape, and exhibits irreversible changes of the magnetization. The hard axis loop, where the hard axis is at right angles to the easy axis, is more or less linear, and generally hysteresis free, i.e., the magnetization is reversible.

Magnetic materials that show a preferential direction for the alignment of magnetization are said to be magnetically anisotropic. When a material has a single easy and hard axis, it is considered as uniaxially anisotropic.

The intrinsic saturation is approached at high H, and the remanence is reached at zero-field. The SQR is given by the ratio of (Mr/Ms), and is essentially a measure of how square the hysteresis loop is. In general, large SQR values are desired usually for recording medium. The formal definition of the coercivity, Hc, is the field required to reduce the magnetization to zero after saturation. The physical meaning of Hc is dependent on the magnetization process, and may be the nucleation field, domain wall coercive field, or anisotropy field. Hc is a very complicated parameter for magnetic films, and is related to the reversal mechanism and the magnetic microstructure, i.e., shape and dimensions of the crystallites, nature of the boundaries, and the surface and initial layer properties [146]. Magnetization hystersis loops for different Co-Ni-Ga alloy in both bulk and rapid solidified samples have been determined with a VSM system. These magnetization hystersis loops were reported in different directions to find direction dependence of magnetization at room temperature. This evaluation have been done just for a few Co-Ni-Ga alloys in forms of polycrystal, spun ribbon and single crystal [12, 16, 18, 58, 99, 105, 145-147].

The angle θ between the magnetic field and the plane of the thin film or ribbon has been adjusted to investigate the effect of texture and or shape anisotropy by Kishi *et al.* as shown in Fig. 53 [18, 58]. They have also shown that the anisotropy of the coercive force in the bulk and ribbon samples are remarkably different, and depends considerably on the direction (Fig. 54).

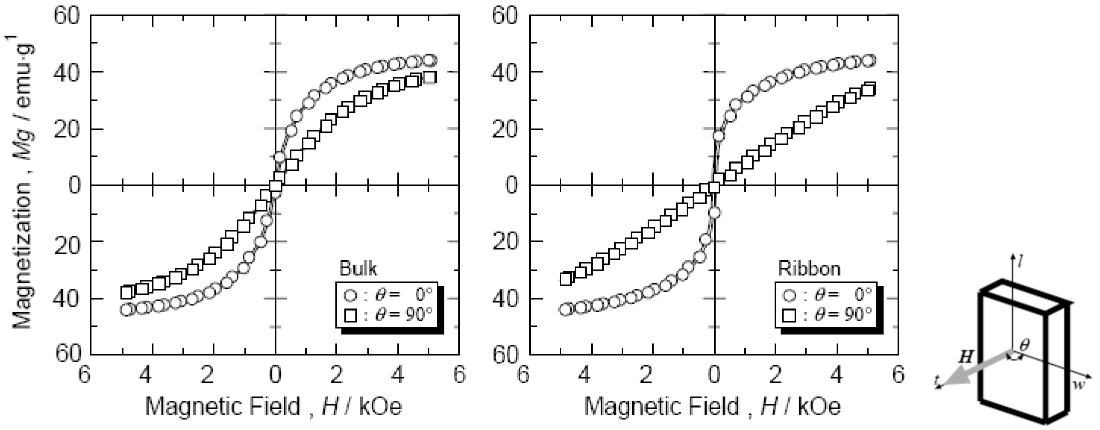

Fig. 53. Direction dependence of magnetization at room temperature in Co2Ni0.85Ga1.15 bulk and as-spun ribbon samples. The coordinates l, t and w denote the longitudinal, thickness and width directions, respectively [18, 58].

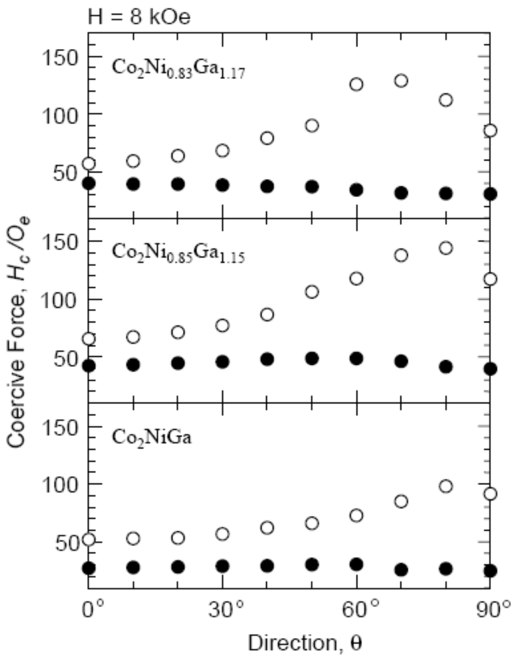

Fig. 54. Relation between coercive force and direction of as spun Co-Ni-Ga ribbons. Open and closed symbols denote data taken from ribbon and bulk samples, respectively. All data were observed at 8 KOe and 293K (room temperature) [18, 58].

1.4.2. Differential Scanning Calorimeter (DSC) and Thermo-Magnetization Curves

The endothermic and exothermic reactions relating to the martensitic transitions can be observed upon heating and cooling, respectively, by a Differential Scanning Calorimeter (DSC) apparatus. Temperatures characterized as the martensitic and austenite transitions, (M_s, M_f, A_s, and A_f) are defined as the cross points of the baseline and the tangent of the maximum or minimum inclination in the DSC curves. A sample of this investigation has been done by Oikawa *et al.* [99], and their result has been shown in Fig. 14 (a). The thermo-magnetization curves has also been evaluated by Oikawa *et al.* [99] for Co-22.5 at% Ni-30 at% Ga alloy in a magnetic field of 500 Oe that show steps corresponding to the martensitic and austenite transition temperatures in Fig. 14 (b) [99].

1.5. Summary

Based on the reported magnetic properties, magnetostriction results and microstructural observations in different chemical compositions of Co-Ni-Ga FSMAs, it seems that the possibility of finding a proper candidate, which can be controlled by a bias magnetic field in a maximum amount of induced strain, is higher in alloys with composition near to Co_2NiGa stoichiometric composition. These alloy series has a high Curie temperature and good magnetization parameters due to their *Heusler-type* structure, and can show large magnetically driven anisotropic properties. These alloys, however, have a dual-phase microstructure because of their chemical composition in normal solidification conditions. The first step in the current study will be a focus on near stoichiometric composition alloys to develop their microstructures as well as their physical and mechanical properties, such as ductility under non-equilibrium and rapid solidification. Then, we will expand our investigation by observing the effect of solidification processing parameters and rapid solidification on two different $Co_{50}Ni_{50-x}Ga_{x}$ (at%) with x ranging up to 50, and $Co_{100-2y}Ni_{y}Ga_{y}$ (at%) with y ranging from 15 to 35 series in searching an appropriate range of alloys illustrating the potential as promising FSMA candidates.

Chapter II

Technical Approach

2.1. Specimen Preparation

According to the design of the levitation coil used in this study, an appropriate specimen was a 7-mm diameter sphere with the weight of approximately 1 to 1.5 grams. Several specimens of Co-Ni-Ga alloy were prepared from high purity Ga (99.999%) and Co (99.99%) as well as Ni (99.99%) plate of 15-mm thickness by Alfa AESAR™ using a Centorr™ arc-melting furnace (Fig. 55). The raw materials were weighted using a Sartorius™ electronic balance with a precision of ±0.005 grams. The raw materials and titanium getter were placed in a bell-jar, and flushed 4 to 5 times with high-purity Argon gas to minimize oxidation during the arc-melting process and to enhance the possibility of the supercooling process. Prior to each arc-melting process, titanium getter was first melted to minimize the oxygen level as low as possible.

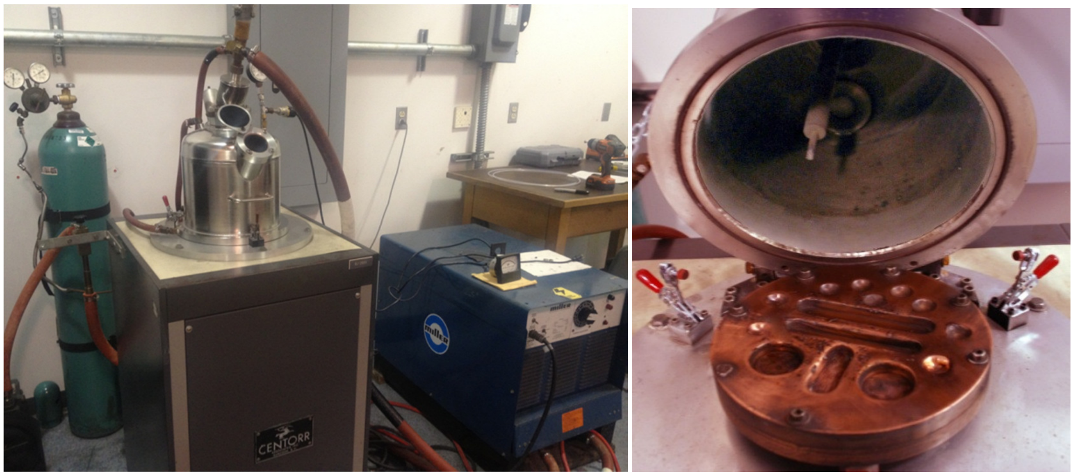

Fig. 55. An arc-melting furnace for specimen preparation

2.2. Electromagnetic Levitation (EML)

The electromagnetic levitation station shown in Fig. 56 was composed of 11 basic units: 1) high-power supplying units, 2) step transformer, 3) processing gas supplier, 4) Cu-chill/Cu slope apparatus, 5) a data acquisition system, 6) a levitation coil, 7) a quartz tube, 8) a processing gas inlet/outlet, 9) a protective gas inlet/outlet, 10) a two-color pyrometer, and 11) a specimen positioning mechanism.

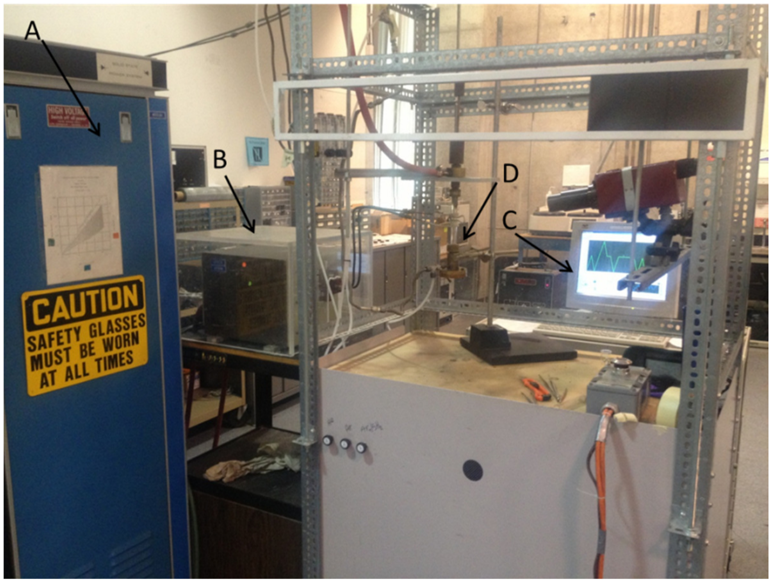

Fig. 56. The levitation station; A) high-power supplying units, B) step transformer, C) data acquisition system and D) electromagnetic levitation coil set up and Cu-chill.

The levitation coil was made of a dehydrated soft copper refrigeration tube of 1.8-inch O.D. × 0.030-inch wall thickness sleeved with insulating fiberglass. The sleeved coil with a desirable length was cut, and both ends were drilled to ensure decent cooling water flow through the coil. The coil was then shaped into a configuration of 2 ups and 4 downs (Fig. 57 (A)) around a 16-mm quartz tube (Fig. 57 (B)). The quartz glass tube provided a protective gas environment in which the specimen was levitated. It was important to minimize the spacing between each round to ensure the uniformity of the magnetic field generated by this coil.

The levitation coil was connected to a step-down transformer powered by a 20kW high frequency (8 MHz) generator. Ar and He gases were delivered through an inlet (Fig. 57 (c)) which was first used to provide an inert atmosphere, and later to supply cooling when needed. Additional Ar with 5% H_2 gas was delivered through the separate inlet directly to the quartz tube to provide a reducing atmosphere during melting process. The Cu-chill was at the bottom of the levitation system (Fig. 57 (D)); therefore, turning off the levitation power resulted in quenching of the liquid droplet on the surface of the Cu-chill.

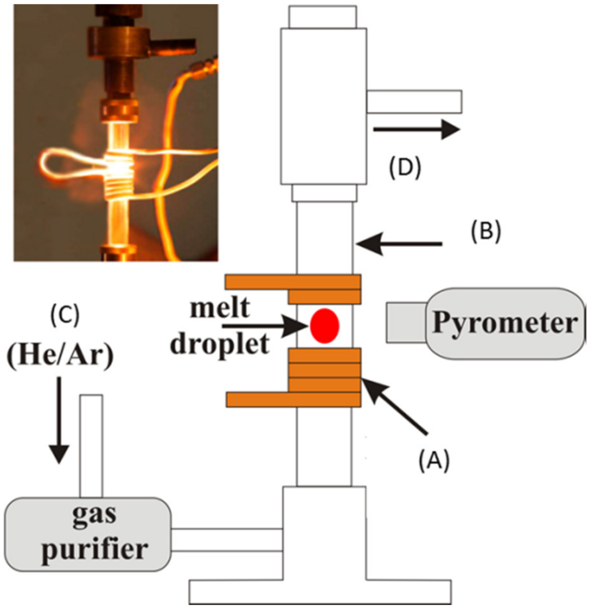

Fig. 57. The details of the electromagnetic levitation apparatus used for containerless melting processes; A) levitation coil, B) quartz glass, C) processing gas inlet (He and Ar/Ar+5%H_2), D) specimen positioning mechanism and protective gas outlet [148]

In order to produce specimens with other geometries, a slope Cu-chill with a desirable 45-60° degree slope could be used (Fig. 58). Various types of materials such as steel, ceramics, or copper could be used as mold materials depending on a thermal diffusivity needed as well as different quenchant liquids. In this study, copper was primarily used in order to provide a high heat extraction rate.

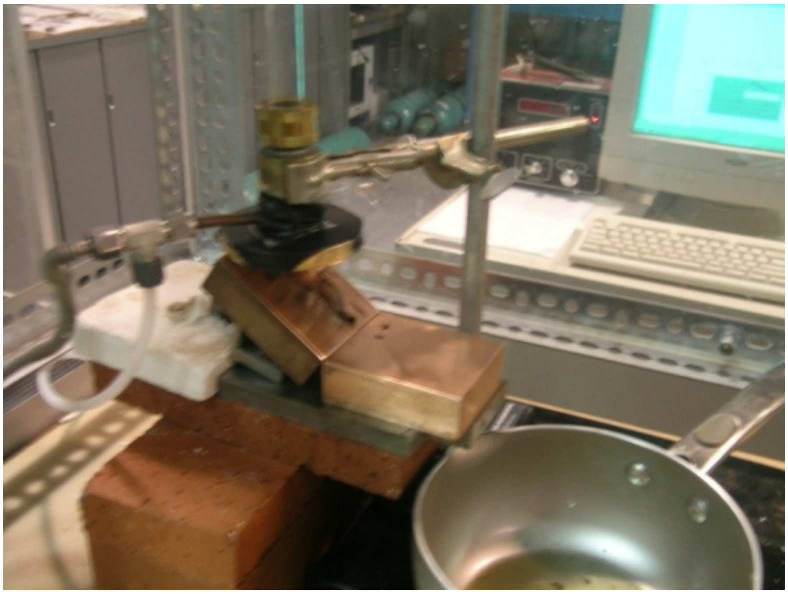

Fig. 58. The slope Cu-chill

2.3. Induction Melting

For induction melting, the same power supply and gas delivery system of EML apparatus were used. The metal shots were then placed inside a Boron Nitride or graphite crucible for the melting process. The configuration of the induction melting process has been shown in Fig. 59. As mentioned before, in order to prevent melt oxidization and cooling, a quartz tube with 16 mm diameter and 0.5 mm thickness was inserted inside the coil through which inert gases of Ar and He flowed. Both Ar and He gases were purified prior to entering the system using a gas purifier with a titanium getter at 800°C.

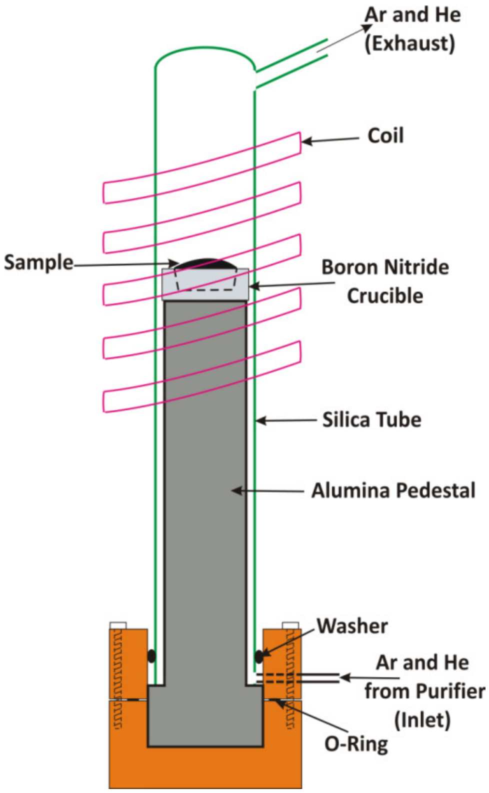

Fig. 59. The configuration of the induction melting process [149]

2.4. Experimental Procedure

Two main procedures are used for producing samples. For the first procedure, the quenched specimens with or without supercooling are allowed to drop on the surface of the slope Cu-chill. However, in the second procedure, which was mostly employed in the current study, the levitated specimens were let to drop on the Cu-chill without slope. For each levitation experiment using the slope Cu-chill, a plastic membrane was inserted between the quartz tube and the slope Cu-chill in order to prevent the downward flow of the He from the quartz tube and to avoid oxygen contamination from environment.

During the levitation state, the thermal history of the specimen was monitored and recorded using a computerized two-color pyrometer equipped with a 10-Hz data acquisition system. By monitoring an online real time-temperature graph, the levitation power could be turned off at any desirable temperature, and the specimen could be solidified through different conditions.

2.5. Specimen Characterization

The as-solidified specimens were mounted using a SAMPLE-KWICK fast cure acrylic by Buehler™, and sectioned using a South Bay Technology™ diamond saw. The specimens were then grinded using 400, 600, 2400 and 4000-grinding papers for a rough surface finishing. The polishing solutions for a fine surface finishing were the water-based alumina (α-Al_2O_3) solutions of 5, 1 and 0.3 micron. To reveal the microstructure, the specimens were etched using an aqueous $FeCl_3$ solution and/or a solution of H_2O15ml, HCl (32%) 60 ml, CH_3COOH (Glacial) 15 ml, HNO_3 (65%) 15 ml for 1 to 5 minutes. The microstructure of each specimen was then mapped using a Nikon™ Optiphot equipped with a digital imaging system with a Nikon™ Coolpix 5000 digital camera. The electron micrographs of the samples were captured using a XL30 FEG scanning electron microscope. The chemical composition of different phases were determined by the Energy Dispersive Spectroscopy (EDS) system at 20 kV using a standard ''ZAF'' (Z-atomic number, A-absorption, and F-fluorescence, plus background and dead time corrections) technique.

The Curie temperature (T_C) and the magnetization (M) were measured using a Vibrating Sample Magnetometer (VSM). In order to distinguish between ferromagnetic and paramagnetic status of the samples, a small magnet was used at room temperature. Those samples that were attracted by the magnet were considered as magnetic. The martensitic and austenitic transformation temperatures were determined by a Differential Scanning Calorimeter (DSC) at cooling and heating rates of 1, 10 and 20°C/min up to 550°C. Exothermic and endothermic peaks can happen during cooling and heating cycles, respectively. These peaks correspond to the martensitic and austenitic transformation for the alloy at 10 or 20ºC/min cooling/heating rate. The austenite and martensite phase transformation temperatures (A_s, A_f, M_s, M_f) were determined by the cross point of the tangent line of the peaks inclination and baseline in the DSC curves.

2.6. Thermal Information

During the levitation stage, the time-temperature profiles of the specimens were recorded as follows. An increase or decrease in the output voltage signal of the pyrometer indicates that the specimen temperature is heating up or cooling down, respectively. Theses output voltage signals are sent from a data acquisition system (DAQ board by National Instrument) to a connected PC, and are converted to the continuous time-temperature graphs using the LabView® software. Prior to measuring heating/cooling cycles for different alloys, the melting point of a pure Ni at 1455°C and/or a pure Cu at 1085°C was checked to accurate the calibration of the pyrometer readings and output voltage signal conversions. An example of such time-temperature profiles has been provided in Fig. 60, which represents the temperature history of a specimen (J1-$Co_{60}Ni_{20}Ga_{20}$) during heating and cooling cycles of the levitation stage. In this figure, the repeated inflection points corresponding to the liquidus temperature ($T_{Liquidus}$) of the sample at 1298°C can be observed.

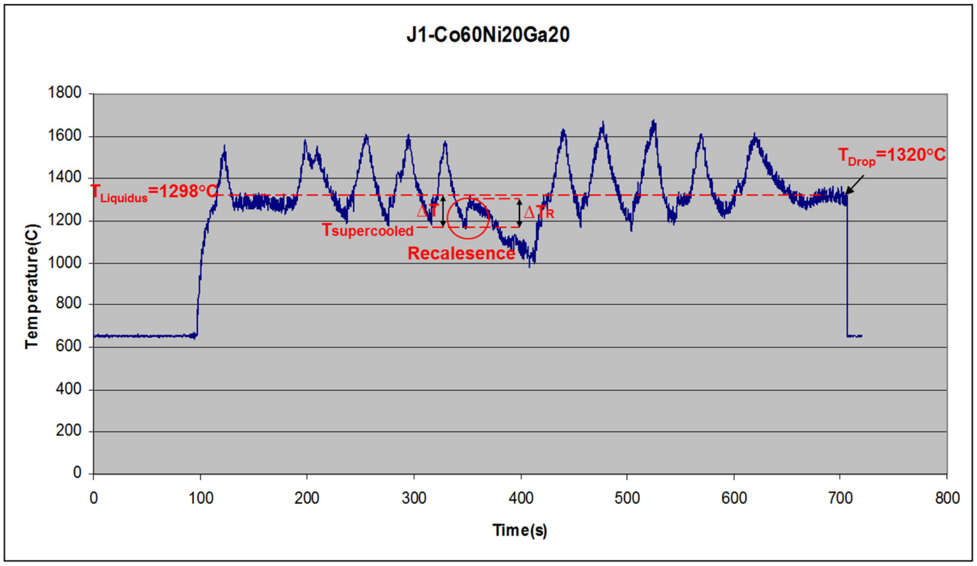

Fig. 60. Time-Temperature profile of a levitated specimen (J1-$Co_{60}Ni_{20}Ga_{20}$) with bulk-supercooling and recalesence phonemenon (circled).

Fig. 61 (a) shows that during the cooling cycle of a levitated specimen that was solidified without bulk supercooling, the inflection point was at the same temperature level as that of the $T_{Liquidus}$ was observed. In contrast, the specimens experiencing bulk supercooling during the cooling cycle indicated no inflection point at the $T_{Liquidus}$, and the cooling curve continued until the thermal recalescence occurred as shown in Fig. 61 (b). In the latter case, the maximum bulk supercooled noted as ΔT is the difference between the $T_{Liquidus}$ and the inflection point immediately before the thermal recalescence. If the magnitude of the thermal recalescence is equal to the maximum supercooling (ΔT=ΔT_R), the solidification process is known as an adiabatic solidification, which was hardly experienced in the current study for all different samples. During the levitation and supercooling process, however, it is more likely to happen that the magnitude of the thermal recalescence is less than the maximum supercooling ($\Delta T < \Delta T_R$). The latter case is detected in the time-temperature profile of the specimen in Fig. 60. The specimens with their processing conditions and thermal information during the levitation processing are summarized in Tables 3, 4 and 5 in the following chapter.

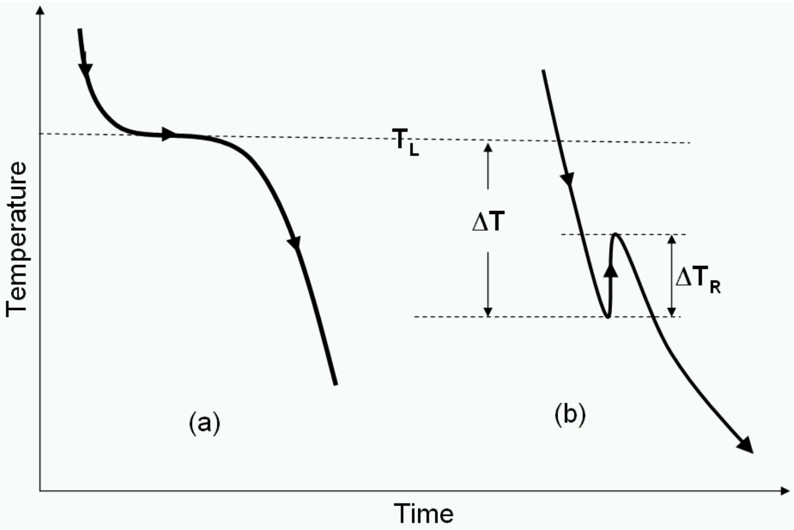

Fig. 61. (a) Normal solidification (b) Bulk supercooling prior to solidification [119]

Chapter III

Results and Discussion

3.1. Effects of Bulk Supercooling and Rapid Solidification on Near *Heusler* Co-Ni-Ga FSMAs

For this part of investigation, EML technique was utilized to explore the effects of bulk supercooling and rapid solidification on a near Co_2NiGa *Heusler-type* alloy and one of its off-stoichiometric alloys. Microstructure evolution in $Co_{46}Ni_{27}Ga_{27}$ (at%) and $Co_{48}Ni_{22}Ga_{30}$ (at%) alloy samples in different thermal conditions was also studied. The purpose was to show how bulk supercooling and rapid solidification processcan form a metastable single β phase which can transform to a martensite phase with different properties at room temperature. The effects of $\gamma+\beta$ on the martensitic and austenitic transformation temperatures and magnetic properties were assessed.

3.1.1. Microstructures

To investigate the effects of rapid solidification on microstructure and phase evolution, two different compositions, $Co_{46}Ni_{27}Ga_{27}$ (at%) and $Co_{48}Ni_{22}Ga_{30}$ (at%), were solidified under different conditions. For the first alloy, specimens of approximately 7-mm diameter were levitated and solidified with three different conditions: 1) rapid quenching of superheated melt against a copper chill, 2) superheating and slow cooling in the levitation state using Helium gas, and 3) bulk supercooling and rapid quenching against the copper. The $Co_{48}Ni_{22}Ga_{30}$ (at%) specimen was also levitated and solidified with superheating and rapid solidification. The processing conditions and nominal composition of the alloys as well as the liquidus (T_L), and drop temperatures (T_{drop}, the temperature at which the levitated samples were dropped) are given in Table 3.

Table 3. Nominal composition and condition of alloys in this study

Samples	Composition (at%)	$T_{liquidus}$ (ºC)	T_{drop} (ºC)	Quenching	Observed Microstructure
D1	$Co_{48}Ni_{22}Ga_{30}$	1210 $T_{S.H}$= 1326	1326	Dropped on Cu-chill (brittle)	Single phase
C2	$Co_{46}Ni_{27}Ga_{27}$	1254 $T_{S.H}$= 1400	1400	Dropped on Cu-chill	Dual Phases
C6	$Co_{46}Ni_{27}Ga_{27}$	1240	≈1000 (soild)	Cooled during levitation	Dual Phases
C11	$Co_{46}Ni_{27}Ga_{27}$	1265 $T_{S.C}$= 1122 (ΔT= 143)	1122	Dropped on Cu-chill	Single+Dual Phases (2 Zones)

$T_{S.H}$: Superheating Temperature; $T_{S.C}$: Supercooling Temperature

The cross sectional microstructures of a sample with $Co_{48}Ni_{22}Ga_{30}$ (at%) composition at a location near the copper chill have been shown in Fig. 62 (a). The figure demonstrates martensite laths within the grains whose boundaries are decorated with a Co-rich phase. The SEM examination of the sample, Fig. 62 (b), illustrates deep cracks along grain boundaries of martensitic matrix phase. The spot EDS analysis on the wall of a removed grain revealed high amount of Ni and Co at the boundary. Although exact compositional determination could not be made due to the relatively large beam diameter of EDS, the approximate chemical composition at the boundary surface was determined as 52%Co-36%Ni-12%Ga. The β' martensite phase had an average composition close to the nominal composition of the alloy (parental phase).

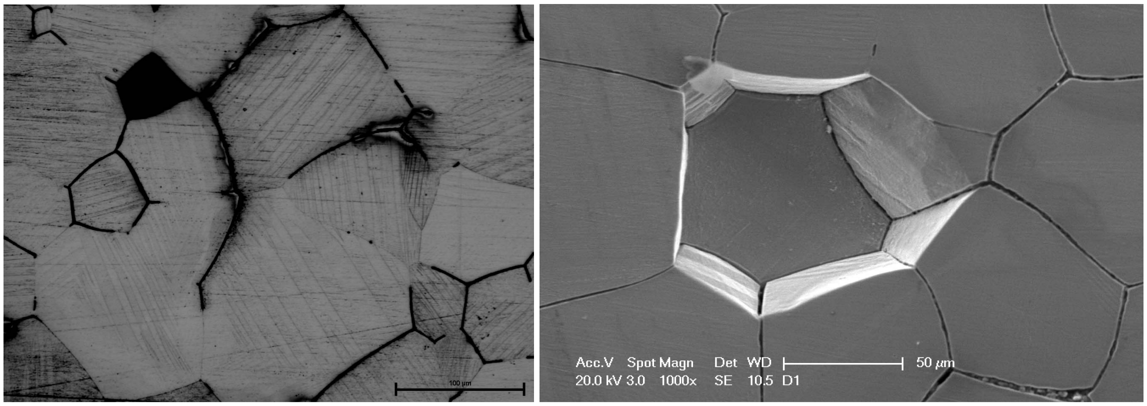

(a) (b)

Fig. 62. (a) Microstructures of a $Co_{48}Ni_{22}Ga_{30}$ (at%) sample quenchedfromsuperheated melt. The grain boundaries contain cobalt-rich phase. (b) SEM micrograph (sample D1) shows severe grain boundaries embrittlement that caused detached grains and one fallen off grain.

The microstructure of the superheated and quenched $Co_{46}Ni_{27}Ga_{27}$ (at%) sample, depicted in Fig. 63 (a), consisted of primary γ dendrites embedded in β matrix. It can be observed that some of the defragmented γ dendrites form curved bands due to melt shearing flow by electromagnetic stirring. The core of the dendrites had composition of 53%Co-26%Ni-21%Ga whereas the β phase just surrounding the dendrite tip (dark area in Fig. 63 (b)) had a composition of 42%Co-28.5%Ni-29.5%Ga.

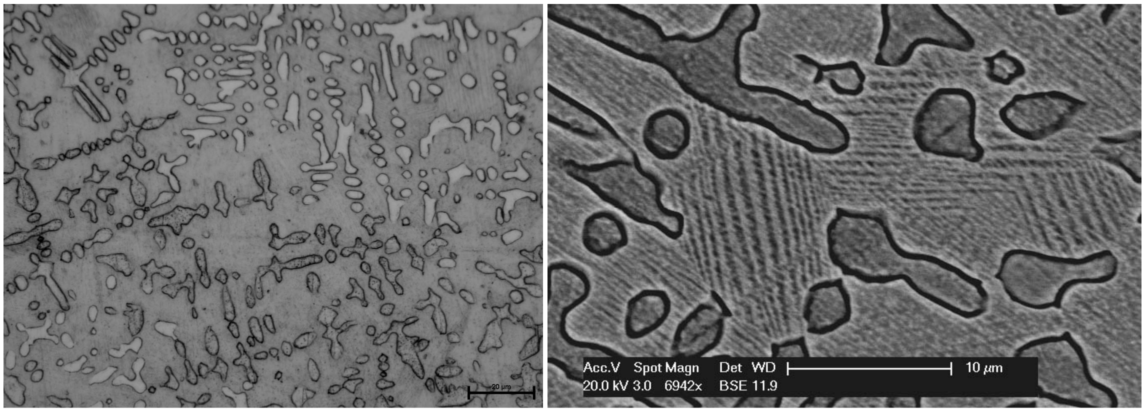

(a) (b)

Fig. 63. (a) Dendritic microstructure of primary γ phase of $Co_{46}Ni_{27}Ga_{27}$ (at%) sample quenched from the superheated melt. (b) BSE micrograph (sample C2); martensite matrix has been shown.

The microstructure and measurements are indicative of the peritectic transformation for the alloy, similar to the one shown in the quasi-binary diagram in Fig. 64.

Away from this peritectic interface, the martensite matrix had an average composition of 43%Co-28% Ni-29%Ga. Other works have also shown that Co-Ni-Ga alloys with composition near to *Heusler-alloy* solidify through a peritectic reaction, $L+\gamma \longrightarrow \beta$ [150, 151]. In Fig. 64 (a), a pseudo binary diagram for Co≈ 47 at% in terms of Ga content was used to show the peritectic reaction [152].

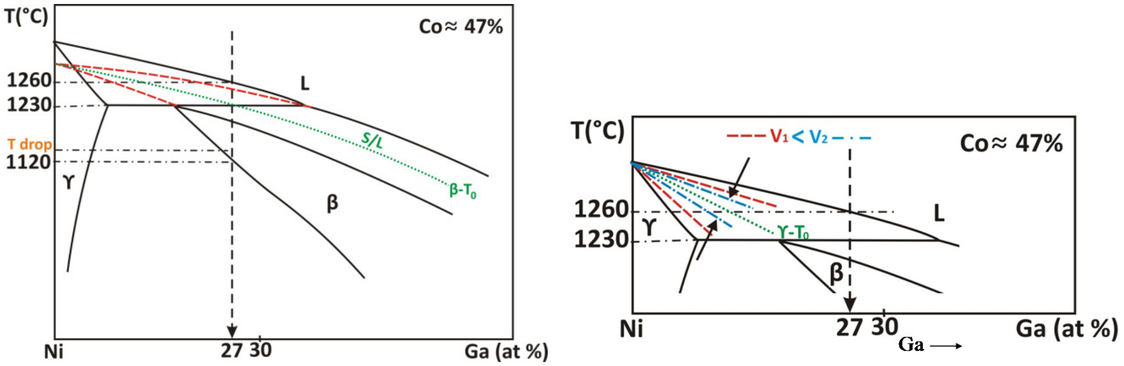

(a) (b)

Fig. 64. (a) A pseudo binary diagram for Co-Ni-Ga alloys containing 47 at% Co [137, 152]. The metastable extension of the liquidus and solidus lines and T_0 line for the β phase are also shown. The dashed arrow shows the composition of the supercooled sample as described in the text. (b) The interface velocity effect on the solute distribution at the moving S/L interface.

The microstructure of another $Co_{46}Ni_{27}Ga_{27}$ sample with the same composition as the previous one (sample C6) but cooled slowly was also found to consist of primary γ dendrite embedded in martensite matrix, as shown in Fig. 65. The dendritic γ phase had a core composition of 55%Co-24%Ni-21%Ga with the martensitic matrix with average composition of 44%Co-27% Ni-29%Ga.

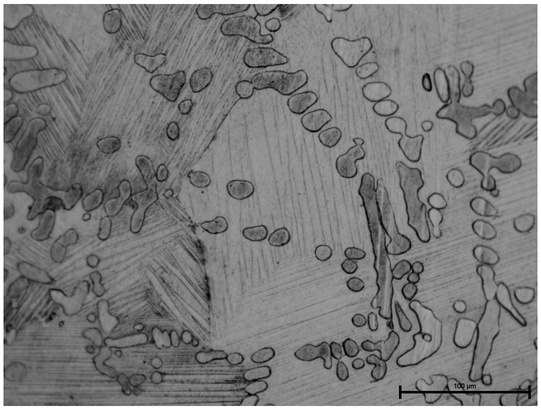

Fig. 65. Microstructure of $Co_{46}Ni_{27}Ga_{27}$ (at%) sample slowly cooled during levitation (sample C6), consisting of fragmented dendrites and interdendritic martensite matrix.

Fig. 66 shows the microstructure of a $Co_{46}Ni_{27}Ga_{27}$alloy which was supercooled by 143°C before being quenched against the copper chill. This sample, which had a disc shape, consisted of two distinct microstructures as shown in the figure. The region next to the chill consisted of 100% martensitic structure. The second region, away from the chilled surface, consisted of γ dendrites surrounded by martensite. The martensite in the first region (zone I), designated as "off-composition martensite", was formed from metastable β phase. It had a composition of 46%Co-27%Ni-27%Ga, similar to the parent alloy. The two-phaseregion far from the quenched surface (zone II), on the other hand, contained γ dendrite of 54%Co-25%Ni-21%Ga and martensite with 43%Co-29%Ni-28%Ga composition. In contrast with the sample D1 indicated in Fig. 62 (a), no cracks or intergranular precipitations were observed in zone I. The zone II microstructure was similar to those in Fig. 63 and Fig. 65, but at a much finer scale.

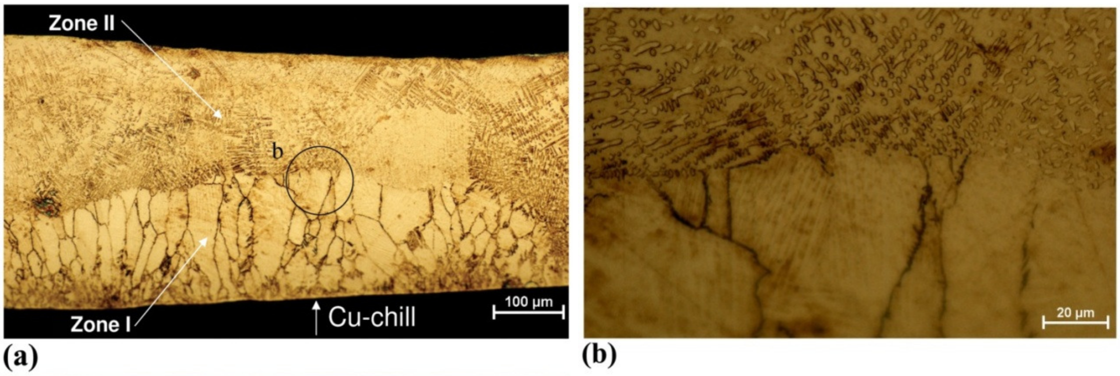

Fig. 66. Microstructure of $Co_{46}Ni_{27}Ga_{27}$ (at%) sample solidified with $\Delta T = 143°C$ supercooling (sample C11). (a) The lower portion (zone I), solidified near the chill surface, consists of non-equilibrium, off-composition, martensite. The upper portion (zone II) contains primary γ dendrite and interdendritic β' (martensitic β). (b) Shows a higher magnification of interface between two different zones.

3.1.2. Metastable Phase Formation in Supercooled and Rapid Solidified Samples

The off-composition martensitic phase formation in the zone I indicates the influence of supercooling and rapid solidification on the microstructure. This can be surmised with the aid of metastable extension of the liquidus and solidus line for β and T_0 curve, as shown in Fig. 64 (a). When the supercooled contacts copper chill, the first solid nucleates and forms at a temperature designated by T_{drop}. Since this temperature is below the T_0 for β, it will form without partitioning, and will have the same composition as the parent phase. As recalescence raises the temperature above peritectic and β-LT_0, partitioning then takes place with the liquid solidified, the same way as those in Fig. 63 and Fig. 65.

It should be noted that beside the formation of metastable composition, the supercooling also strongly increases the interface velocity. It has been shown that as the interface velocity increases, the partitioning coefficient (k_v) becomes large and approaches unity with complete solute entrapment [115, 153-156]. The influence of supercooling on the interface velocity can be described considering the thermal condition at a moving solid-liquid (S/L) as given by the Stefan's equation:

$$v_i = \frac{K_{S,i}G_{S,i} - K_{L,i}G_{L,i}}{\rho_S H_f} \qquad \text{Eq. 17}$$

Where $K_{S,i}$ and $K_{L,i}$ are thermal conductivity on the solid and liquid side at the interface, ρ_S is the density of solid, H_f is the heat of fusion of solid, and $G_{S,i}$ and $G_{L,i}$ are the temperature gradients at the interface on the solid and liquid side, respectively. For the supercooled liquid, the $G_{L,i}$ term is negative, and it enhances the interface velocity. However, as solidification proceeds, the heat of recalescence alters the magnitude of the temperature gradients on both sides of the interface, and consequently, reduces the interface velocity. In addition, the recalescence could raise the liquid temperature above T_0, where partitioning (segregation) takes place. To avoid the recalescence above T_0 for a supercooled melt, the supercooling needed is approximately $\Delta T = H_f/C_{p,L}$, where $C_{P,L}$ is the heat capacity of the liquid. Since achieving that high supercooling is almost impossible in practice, we dropped the supercooled sample well below the T_0 (T_{drop} in Fig. 64 (a)) before the occurrence of the recalescence. Another approach would be to combine supercooling with rapid heat removal by quenching against a conductive substrate, which is the case for this work. It is believed that solute entrapment or partitionless solidification of the supercooled sample shown in Fig. 66 was led to the formation of the single β phase from the hyperperitectic alloy. Subsequently, the β (BCC) has transformed to the off-composition β' (BCT). Therefore, the composition of martensitic phase (β') is the same as that of the parent liquid.

3.1.3. Martensitic Transformation

The DSC curves for sample D1 have been shown in Fig. 67 (a) and (b) for two different heating/cooling rates of 10 and 1ºC/min. Exothermic and endothermic peaks are observed during cooling and heating cycles, respectively, in Fig. 67 (a). These peaks correspond to the martensitic and reverse transformation for the alloy at 10ºC/min cooling/heating rate. The A_s, A_f, M_s and M_f were determined as 60, 95, 37.5 and 6ºC, respectively for the first heating/cooling cycle. Small downward shift of the martensitic transformation temperatures (M_s and M_f), about 5ºC for each cycle, were observed during subsequent cooling cycles. The reverse transformation to austenite (A_s and A_f) also shifted downward but with a much larger degree. For example, A_s changed from 60 to 50, 42, and eventually to 30.5ºC between the first and the fourth cycle.

The DSC curves of the same sample as above but at a slower heating/cooling rate of 1ºC/min are shown in Fig. 67 (b). During the first heating cycle, the reverse martensite transformation peak was observed near the same temperatures as in the first cycle of the curves shown in Fig. 67 (a). However, no martensitic transformation was observed during the cooling cycle even through thesample was cooled to-15ºC. The subsequent cycles were also devoid of martensitic or austenitic transformations. The comparison of the two DSC curves may indicate decomposition and/or change of austenite composition during slow heating process (1ºC/min).

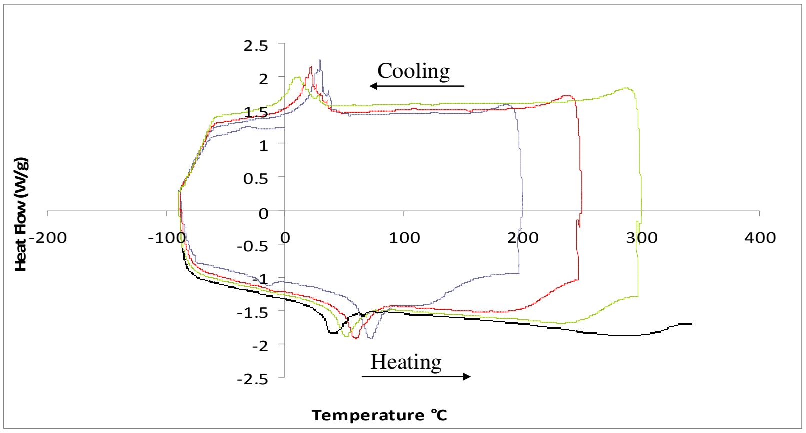

(a) 10 °C/min

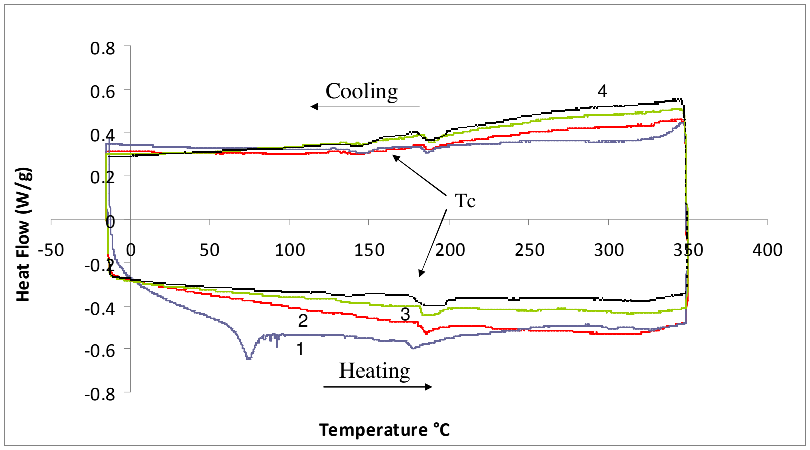

(b) 1 °C/min

Fig. 67. DSC graphs of four heating/cooling cycles for $Co_{48}Ni_{22}Ga_{30}$ (at%) sample quenched from the superheated melt (sample D1) with cooling/heating rates: (a) 10ºC/min and (b) 1ºC/min.

Such compositional and phase change could conceivably suppress the martensite transformation temperature to well below -15ºC. A similar influence of heat treatment on the martensitic transformation temperature has been reported by other investigators for both heat treated single phase β (B2-type) and a single crystalof $Co_{48}Ni_{22}Ga_{30}$ alloy [99, 150]. It should be noted that two other peaks are also observed in Fig. 67 (b) around

180ºC during heating and cooling of this sample. These peaks are believed to indicate the Curie temperature (T_C) of the sample.

The typical DSC curve for sample C2 is shown in Fig. 68 (a). In contrast with the sample shown in Fig. 67 (a), pronounced exothermic martensitic and endothermic austenite transformation peaks around 30 to 60ºC were not observed in this sample. However, there were small peaks in cooling and heating cycles that respectively show M_s and A_f to be around -21ºC and -4ºC. It should be noted that these transformation temperatures are below those reported in Ref [152] for the same alloy composition. The difference in these two observations is believed to be due to the fact that the sample in the present work consisted of two phases where those of the previous studies were for heat treated single phase.

Similarly, Fig. 68 (b) shows the DSC curve for sample C6, which consisted of two phases, γ and β. The M_s and A_f temperatures during the first cycle were around -20ºC and -2ºC, respectively. However, for the latter sample, the peaks were more pronounced since the martensite matrix had higher percentage in comparison with sample C2.

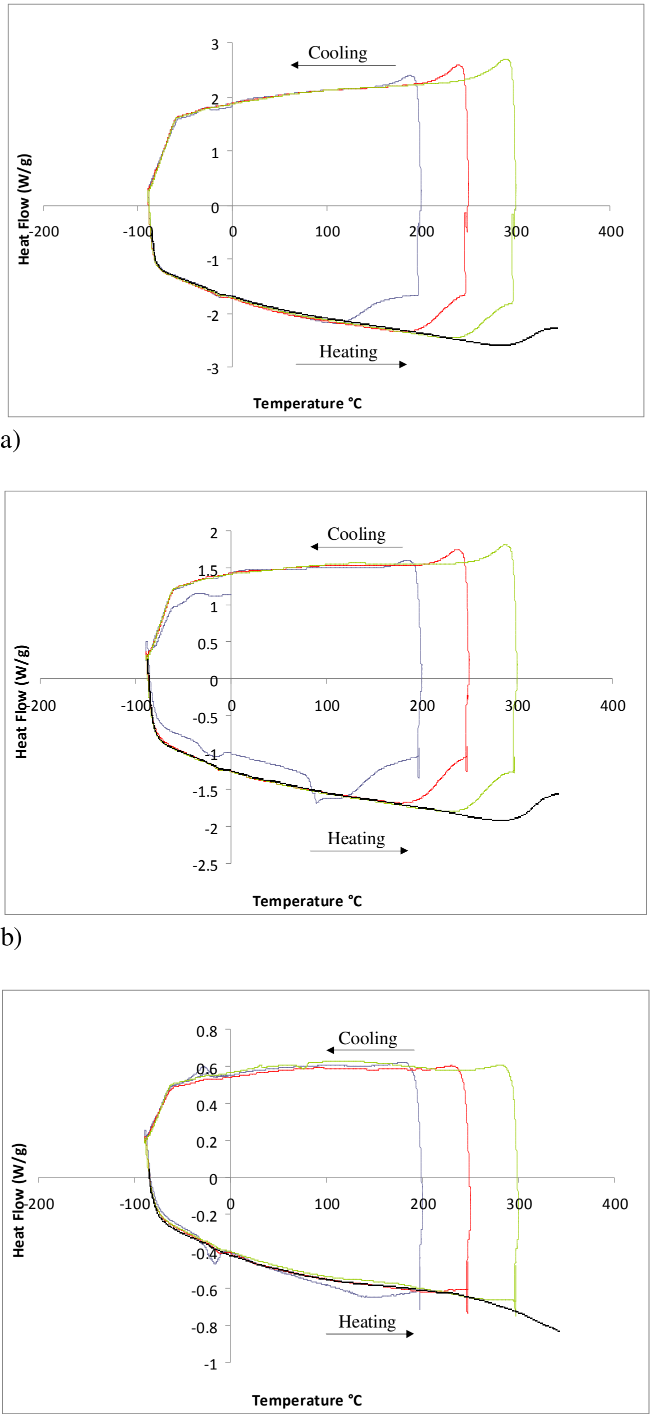

(a)

(b)

(c)

Fig. 68. DSC graphs of four heating/cooling cycles with 10ºC/minheating/cooling rate of $Co_{46}Ni_{27}Ga_{27}$ (at%) samples (a) C2 , (b) C6 and (c) C11 (with ΔT= 143ºC supercooling).

The DSC curves for sample C11 are shown in Fig. 68 (c), where both endothermic and exothermic peaks in the first cycle can be seen. Martensitic starting and reverse finishing transformation temperatures, M_s and A_f are -15ºC and -6ºC, respectively. Although the M_s temperature has increased by about 6ºC, the martensitic and reverse transformation temperatures are still suppressed to temperatures quite below room temperature due to presence of γ (dendrite)+ β' phases in this sample (zone II) along with pure martensite microstructure, β'(zone I). As the heating and cooling cycle continued to higher temperature ranges, these two peaks become weak and finally disappear. The other broad peak occurred around 150ºC in the second heating cycle that may indicate some form of solid state transformation. It is conceivable this correlate with the decomposition of the off-composition phase in zone I.

3.2. Magnetic Properties

3.2.1. Magnetization Hysteresis Loops

The magnetization hysteresis loops (M vs. H) at different temperature for the $Co_{48}Ni_{22}Ga_{30}$ (at%) β single-phase alloy, sample D1, is shown in Fig. 69. The “in-plane” magnetization (θ= 0º) in the figure refers to the plane of the sample which was parallel to the quenched surface and the “out-of-plane” magnetization (θ= 90º) refers to the direction perpendicular to the chill surface. The magnetic saturation for both in-plane and out-of-plane magnetization directions decreased from about 45 to 40 emu/g with increasing temperature from 65 to 150 K, and then fell to 32.6 emu/g at room temperature (295K). Similarly, the coercive forces (inserted graphs in Fig. 69) decreased with increasing temperature from 50 Oe at 65 K to 10 Oe at room temperature for both in- and out-of-plane magnetization directions. The in-plane magnetization curves were found to be more easily saturated (at 5 kOe) than out-of-plane magnetization curves (at 10 kOe) at all temperatures.

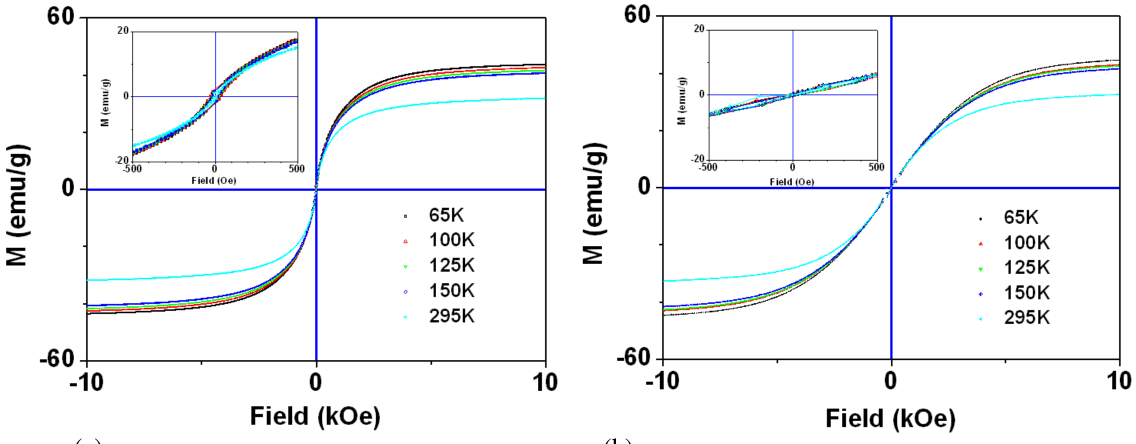

(a) (b)

Fig. 69. Magnetic properties of $Co_{48}Ni_{22}Ga_{30}$ (at%) alloy quenchedfromthesuperheated melt (D1sample), the inserted graphs at low scale (500 Oe and 20 emu/g) also show coercive forces (a) in-plane (θ= 0º) (b) out-of-plane (θ= 90º).

For sample C2 (Fig. 70), the magnetic saturation for both in-and out-of-plane magnetization directions decreased from 52 to 48 emu/g with increasing temperature from 65 to 150 K, respectively, and dropped to 38 emu/g at room temperature. The coercive force for this sample also decreased with increasing temperature from 100 Oe at 100 K to 10 Oe at room temperature for in- plane magnetization direction, and from 75 Oe at 100 K to 10 Oe at room temperature for out-of-plane magnetization direction.

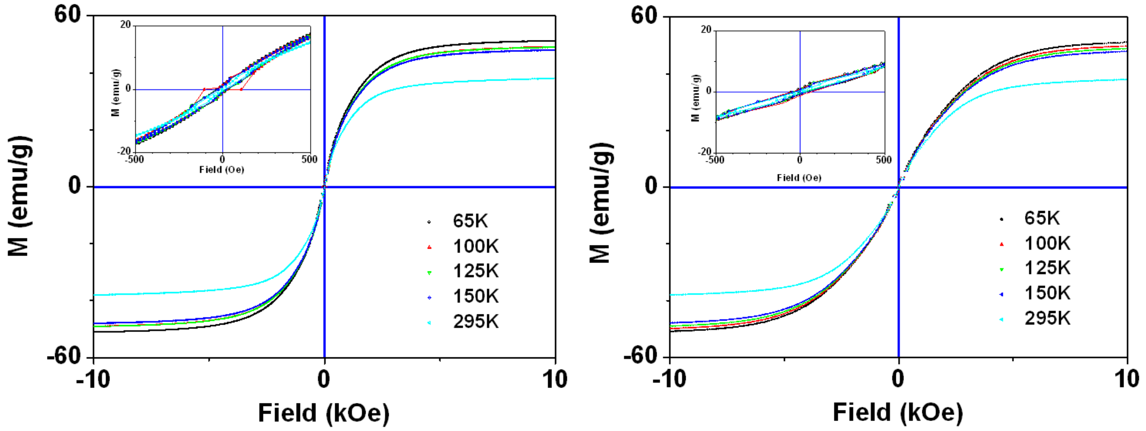

(a) (b)

Fig. 70. Magnetic properties of $Co_{46}Ni_{27}Ga_{27}$ (at%) alloy quenchedfromthesuperheated melt (C2 sample), the inserted graphs at low scale (500 Oe and 20 emu/g) also show coercive forces (a) in-plane (θ= 0º) (b) out-of-plane (θ= 90º).

The magnetic properties of C6 sample has been shown in Fig. 71. The hysteresis loops for in- and out-of-plane directions in different temperatures were displayed. Similarly, the magnetic saturation for both in- and out-of-plane magnetization directions of sample decreased from 52 to near 48 emu/g with increasing temperature from 65 to 150 K, respectively, and then to 38.2 emu/g at room temperature. The coercive forces also decreased with increasing temperature from 25 Oe at 65 K to 5 Oe at room temperature for both in- and out-of-plane magnetization directions.

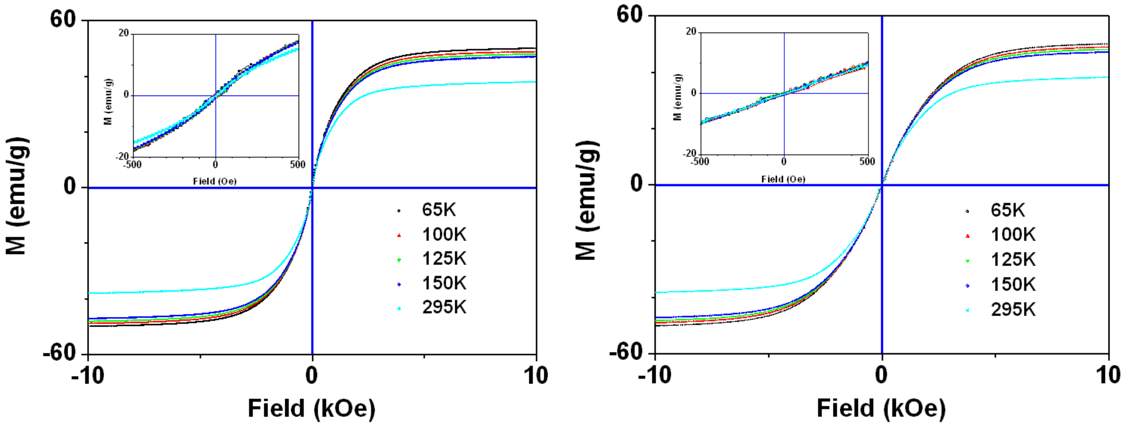

(a) (b)

Fig. 71. Magnetic properties of $Co_{46}Ni_{27}Ga_{27}$ (at%) alloys cooled during levitation (C6 sample), the inserted graphs at low scale (500 Oe and 20 emu/g) also show coercive forces (a) in-plane (θ= 0º) (b) out-of-plane (θ= 90º).

The magnetization moment (M) versus applied magnetic field (H) in different temperatures for measuring coercivity and saturated magnetization of C11 sample has been given in Fig. 72. For this sample, which was supercooled and quenched, the magnetic saturation for both in- and out-of-plane magnetization directions decreased from 52 to 48 emu/g with increasing temperature from 65 to 150 K, respectively, and reduced to 38 emu/g at room temperature. The coercive forces decreased with increasing temperature from 30 Oe at 65 K to 10 Oe at room temperature for in-plane magnetization direction and from 80 emu/g at 65 K to about 30 emu/g at room temperature for out-of-plane magnetization direction.

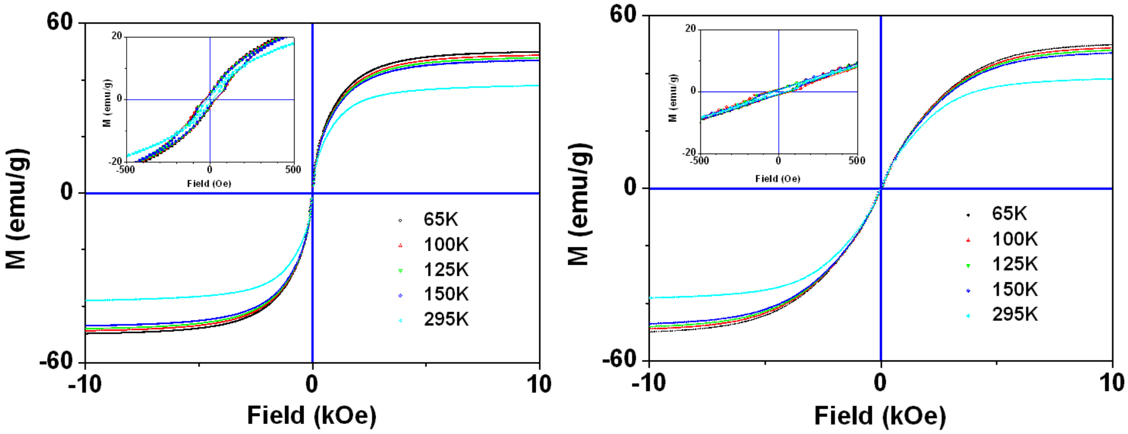

(a) (b)

Fig. 72. Magnetic properties of $Co_{46}Ni_{27}Ga_{27}$ (at.%) alloys with ΔT= 143°C supercooling (C11 sample), the inserted graphs at low scale (500 Oe and 20 emu/g) also show coercive forces (a) in-plane (θ= 0º) (b) out-of-plane (θ= 90º).

For comparison, Fig. 73 illustrates M-H curves for both in- and out-of-plane magnetization directions at room temperature for $Co_{48}Ni_{22}Ga_{30}$ and $Co_{46}Ni_{27}Ga_{27}$ samples (C2, C6 and C11). In Fig. 73 (a), the difference in magnetic moment of both in- and out-of-plane directions reflects the anisotropic texture and directional properties of purely martensitic phase of sample D1 at room temperature. It has been shown in Fig. 73 (b) that the magnetic properties of sample C2 also changed through different orientations in the same way mentioned earlier. However, the difference between magnetization curves in two main directions was less than the one in sample D1. The directional magnetic property decreased because of martensite matrix and γ ($\beta' + \gamma$) phase forms instead of purely martensite phase of sample D1. The magnetic saturation increased from 32.6 emu/g for sample D1 to 38 emu/g at room temperature in this sample owing to its near *Huesler* composition. Magnetic moment of sample C6 (Fig. 73(c)) had different amounts along both directions. Nevertheless, the directional magnetic property in this sample had the lowest amount between other samples due to forming of martensite matrix and γ ($\beta'+\gamma$) phases as well as differentsample shape from others (not completely flat). The saturation magnetization at room temperature had the same amount of sample C2 (38 emu/g).

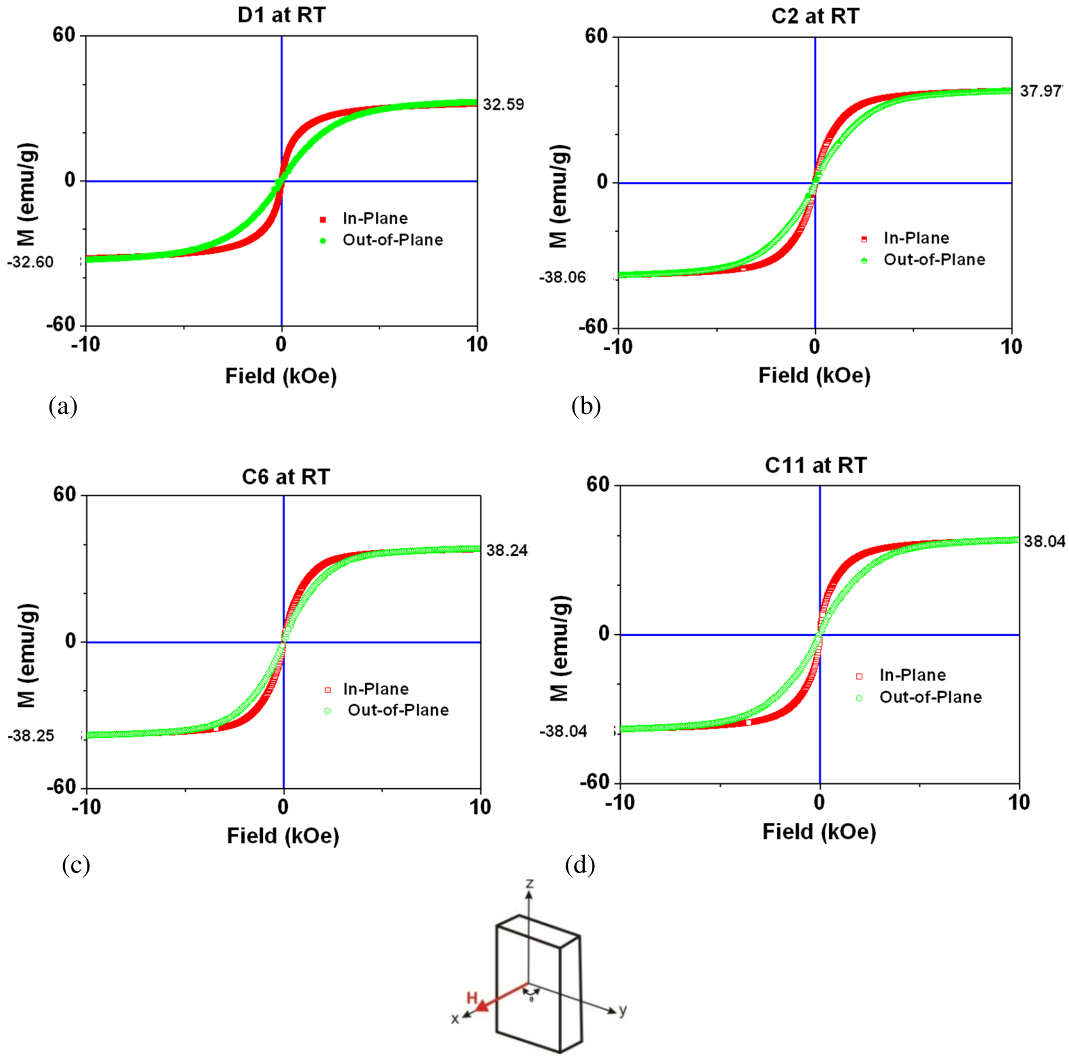

Fig. 73. M-H curves at room temperature of (a) $Co_{48}Ni_{22}Ga_{30}$ (at%) (D1sample) and different $Co_{46}Ni_{27}Ga_{27}$ (at%) alloy samples (b) C2, (c) C6 and (d) C11 samples.

For sample C11 in Fig. 73 (d), the magnetic properties also changed through different orientations as discussed earlier but the difference is even higher than that of purely martensite phase in sample D1. The saturation magnetization of this sample at room temperatures also had higher amount (38 emu/g) than sample D1 (32.6 emu/g) because of its near *Huesler* composition. Moreover, it is approximately equal to other $Co_{46}Ni_{27}Ga_{27}$ (at%) samples regardless of their different microstructures.

3.2.2. Magnetization Saturation

To investigate the Curie temperature, the saturation magnetization (Msat) at different temperatures for $Co_{48}Ni_{22}Ga_{30}$ (at%) (sample D1) and $Co_{46}Ni_{27}Ga_{27}$ alloys (samples C2,C6 and C11) have been plotted in Fig. 74. All of $Co_{46}Ni_{27}Ga_{27}$ samples had well above room temperature Curie temperatures around 400 K as a point of slope change in magnetization curves. However, this was not very accurate due to measurement limitations above 400 K. For $Co_{48}Ni_{22}Ga_{30}$ alloy (sample D1) as an off stoichiometric alloy of *Heusler-type* composition, the Curie temperature was about 350 K and was not sensitive to compositional changes.

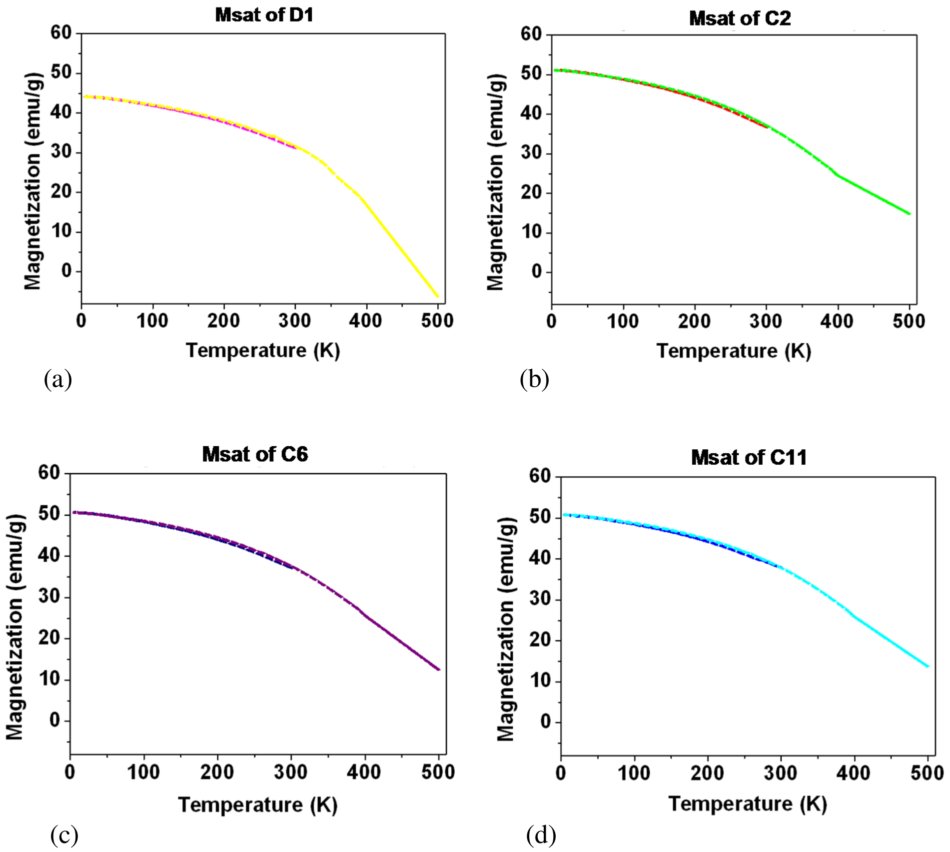

(a) (b)

(c) (d)

Fig. 74. Magnetization saturation (Msat) in different temperatures (dashed lines are related to cooling cycles) of (a) $Co_{48}Ni_{22}Ga_{30}$ (D1sample) and different $Co_{46}Ni_{27}Ga_{27}$ (at%) alloy samples (b) C2, (c) C6 and (d) C11.

3.2.3. Coercivity

Fig. 75 shows coercive force in different directions at room temperature for $Co_{48}Ni_{22}Ga_{30}$ (at%) (D1sample) and different $Co_{46}Ni_{27}Ga_{27}$ (at%) alloy samples (C2, C6 and C11). It has been found that the supercooled and rapidly solidified $Co_{46}Ni_{27}Ga_{27}$alloy (sample C11) had the highest directional coercivity among these samples. The minimum and maximum coercive forces were obtained around 14 Oe at $\theta = 0^\circ$ and 45 Oe at $\theta \approx 50^\circ$, respectively. The coercive forces in samples C2, C6 and D1 were not dependent to direction.

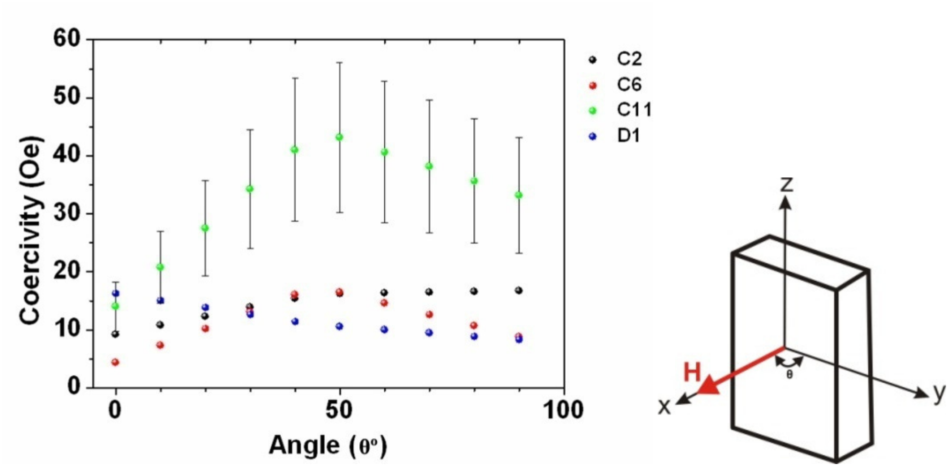

Fig. 75. Coercive force in different directions at room temperature for $Co_{48}Ni_{22}Ga_{30}$ (at%) (D1sample) and different $Co_{46}Ni_{27}Ga_{27}$ alloy samples (C2, C6 and C11 samples).

3.3. Solidification and Microstructural Evolution of Co-Ni-Ga Alloys

In this part of investigation, the effects of solidification parameters and different cooling rates on the microstructure of a series of Co-Ni-Ga alloys were assessed. Different microstructures of various alloys in and out of β single-phase composition range, which can potentially form martensitic transformation were evaluated. The role of the solidification variables and chemical composition in the microstructure and phase transformation in the ternary alloys $Co_{50}Ni_{50-x}Ga_x$ (at%) with x ranging up to 50, and $Co_{100-2y}Ni_yGa_y$ (at%) with y ranging from 15 to 35 was studied.

3.3.1 Investigation of Solidification Parameters and Microstructure of $Co_{50}Ni_{50-x}Ga_x$ (at%) Alloys

In searching for potential ductile FSMA candidates among these alloys, it is necessary to have a good knowledge of the γ and β phase formation in both equilibrium and non-equilibrium conditions. Although a few isothermal sections of the Co-Ni-Ga ternary phase diagram are availableat some temperatures between 600 and 1150°C in Co-Ni-Ga system as shown in Fig. 76 [12, 99, 137, 152], a general knowledge of the solidification process in both conventional and rapid (non-equilibrium) conditions is lacking. To fill this gap, the current study aims to assess the solidification processing parameters.

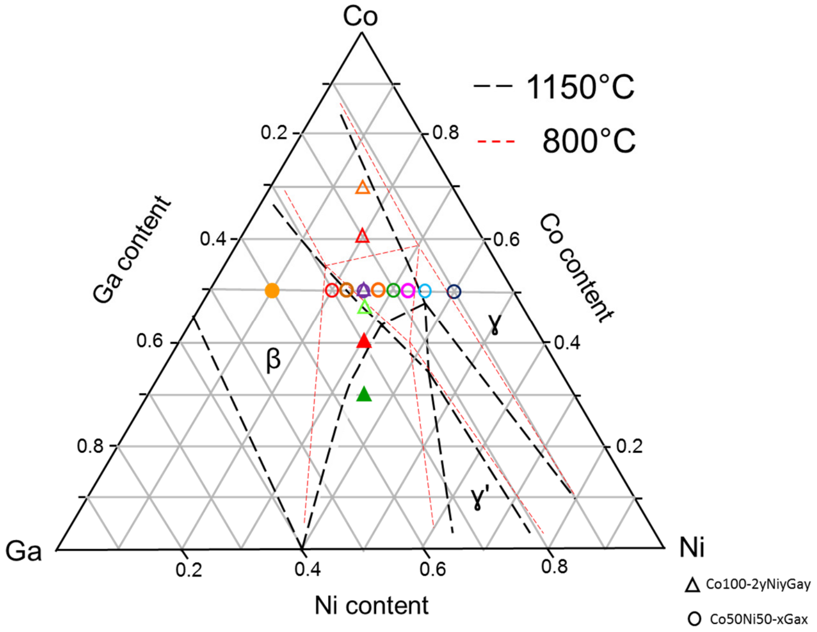

Fig. 76. Isothermal section schematic phase diagram of the Co-Ni-Ga system at 800 and 1150°C [137, 152]. The designed two composition series, the circles denote Co$_{50}$Ni$_{50-x}$Ga$_x$ and the triangles denote Co$_{100-2y}$Ni$_y$Ga$_y$ have shown. The solid shapes show the alloys with the Curie temperature lower than room temperature and hallow ones represent the alloys with the Curie temperature higher than room temperature.

The processing conditions and nominal composition of the alloys in the investigated series are given in Table 4. For the sample names, the letters were assigned for different amount of Ga (x), and the numbers show samples of the same group, which were solidfied from different thermal conditions and cooling rates. The table also shows the liquidus temperature and the temperature at which the levitated samples were dropped.

The cross sectional microstructures of a sample with $Co_{50}Ni_{40}Ga_{10}$ (at%) composition (G1) in Fig. 77 (a) consists of almost γ single phase with well-developed dendrites and β phase in matrix structure when it cooled down with Helium gas from its T_L in levitation mode, and quenched from solid and liquid region (S+L) on a copper chill surface. Fig. 77 (b) shows the same composition sample, $Co_{50}Ni_{40}Ga_{10}$ (at%) (G2), which dropped from the T_L on a copper chill. The single γ phase is starting to form in a region very close to the chill surface. This can be explained with the aid of a metastable extension of the liquidus and solidus line for γ and T_0 curve, as shown in Fig. 79. When the melt drops about liquidus temperature in levitating position, its temperature can decreases about 50°C below the liquidus temperature during falling down before hits the copper chill surface. As this dynamic supercooling phenomenon happens, and supercooled melt contacts copper chill, the first solid nucleates, and forms at a temperature about 50°C below T_L. In this sample, the dynamic supercooling was about 30°C (less than 50°C), and about 1370°C designated by T_{drop} in Table 4. Since this temperature is near γ-T_0 for forming metastable γ phase in this alloy, it seems that the γ phase is starting to form in a very thin layer close to the Cu-chill without partitioning (metastable single γ), and will have the same composition as the parent phase. As the latent heat of solidification of the single metastable γ phase rose after hitting the Cu-chill, the temperature of the remaining liquid phase increased to above 1370°C and γ-L T_0; Partitioning then took place and the liquid solidified in the same way as shown on top of that thin γ layer in Fig. 77 (b).

Table 4. Nominal composition and solidification condition of alloys in $Co_{50}Ni_{50-x}Ga_x$ (at%) series

Sample	**Composition (at%)**	$T_{liquidus}$ **(°C)**	T_{drop} **(°C)**	**Quenching**	**Observed Microstructure**
G1	$Co_{50}Ni_{40}Ga_{10}$	1398	1280 Dropped from (S+L)	Dropped on Cu-chill	Dual phases
G2	$Co_{50}Ni_{40}Ga_{10}$	1398	1368 (Dynamic Supercooling)	Dropped on Cu-chill	Dual Phases
S	$Co_{50}Ni_{35}Ga_{15}$	1350	1300 (Dynamic Supercooling)	Dropped on Cu-chill	Single+Dual Phases (2 zones)
R	$Co_{50}Ni_{32.5}Ga_{17.5}$	1340	≈1000 (solid)	Cooled during levitation	Dual Phases
H1	$Co_{50}Ni_{30}Ga_{20}$	1305	1305	Dropped on Cu-chill	Dual Phases
H2	$Co_{50}Ni_{30}Ga_{20}$	1305 $T_{S.C}$=1245 (ΔT=60)	1245	Dropped on Cu-chill	Single+Dual Phases (2 zones)
H3	$Co_{50}Ni_{30}Ga_{20}$	1305	1222 (from S+L)	Dropped on Cu-chill	Dual Phases
H4	$Co_{50}Ni_{30}Ga_{20}$	1305 $T_{S.C}$=1260 (ΔT=45)	1260	Dropped on Cu-chill	Single+Dual Phases (2 zones)
P	$Co_{50}Ni_{27.5}Ga_{22.5}$	1282	1298	Dropped on Cu-chill	Dual Phases
A1	$Co_{50}Ni_{25}Ga_{25}$	1276	1276	Dropped on Cu-chill	Dual Phases
A2	$Co_{50}Ni_{25}Ga_{25}$	1276	1200 (from S+L)	Dropped on Cu-chill	Dual Phases
A3	$Co_{50}Ni_{25}Ga_{25}$	1276 $T_{S.C}$=1200 (ΔT=76)	1200	Dropped on Cu-chill	Single Phase
O	$Co_{50}Ni_{22.5}Ga_{27.5}$	1260 $T_{S.C}$=1103 (ΔT=147)	1103	Dropped on Cu-chill	Dual Phases
E1	$Co_{50}Ni_{20}Ga_{30}$	1248	1248	Dropped on Cu-chill	Single Phase
E2	$Co_{50}Ni_{20}Ga_{30}$	1248 $T_{S.C}$=1194 (ΔT=54)	1194	Dropped on Cu-chill	Single Phase
F1	$Co_{50}N_{10}Ga_{40}$	1216 $T_{S.C}$=1190 (ΔT=26)	1190	Dropped on Cu-chill	Single Phase

$T_{S.C}$: Supercooled Temperature

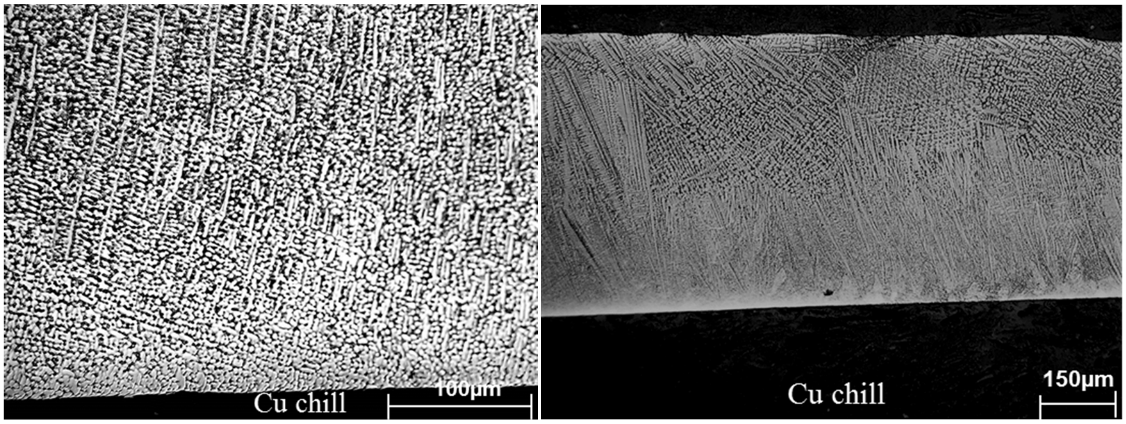

(a) (b)

Fig. 77. Microstructures of $Co_{50}Ni_{40}Ga_{10}$ (at%) samples quenched from (a) S+L region (G1) and (b) liquidus temperature (G2). The well-developed γ dendrites in β matrix in both microstructures and forming single metastable γ phase in a very thin layer near to the Cu-chill surface in (b) have been shown.

The microstructure of $Co_{50}Ni_{35}Ga_{15}$ (at%) alloy (S) which was quenched form the liquidus temperature consisted of two distinct microstructures (Fig. 78). The region close to the copper chill consisted of a single metastable γ phase (Fig. 78 (b)). The second region, away from the chilled surface, consisted of γ dendrites surrounded by β phase (Fig. 78 (a)). The single γ phase in the first region (zone 1) designated as matastable γ phase as it was mentioned before for the sample G2. It had a composition of 50%Co-35%Ni-15%Ga, similar to the parent alloy. The two phase area far from the quenched surface (zone 2), on the other hand, contained γ dendrite of 53%Co-35%Ni-12%Ga and β matrix with 42%Co-38%Ni-20%Ga average composition. The zone 2 microstructure in Fig. 78 (a) was similar to that in Fig. 77 (a).

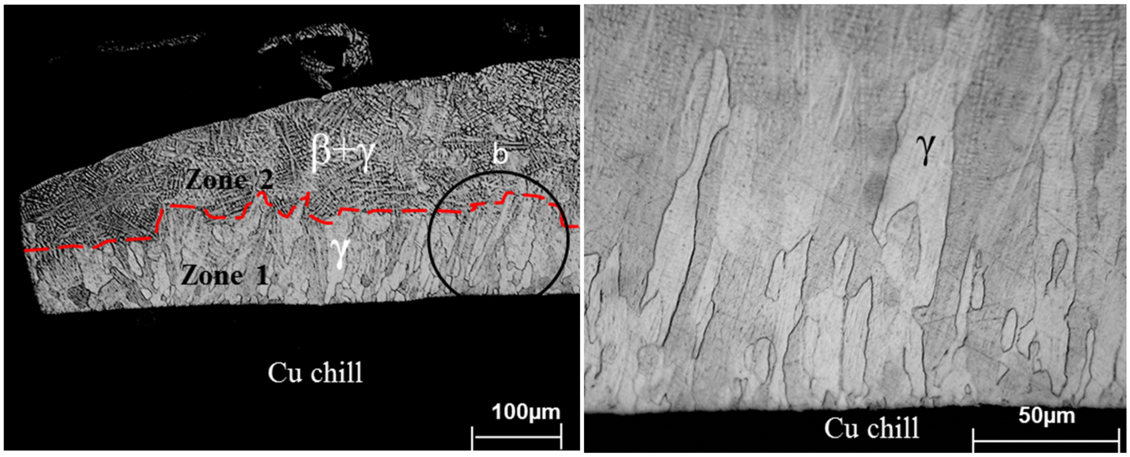

(a) (b)

Fig. 78. Microstructure of $Co_{50}Ni_{35}Ga_{15}$ (at%) sample (S) quenched from liquidus temperature. (a) The lower portion (zone 1), solidified near the chill surface, consist of metastable single γ phase. The upper portion (zone2) contains primary γ dendrite and interdenderitic β phase. (b) A higher magnification of metastable γ phase and interface between two different zones

The metastable single γ phase formation in the zone 1 indicates the influence of supercooling and rapid solidification on the microstructure (Fig. 78). Again, this happens due to a dynamic supercooling at about 50ºC. Here, the first solid nucleates and forms at about 1300°C (= T_{drop}) which is well below the γ-T_0 for forming a metastable γ phase in this alloy. The metastable single γ phase formed as shown in the zone I in Fig. 78. With increasing the temperature following solidification of a single metastable γ phase after hitting the Cu-chill, the temperature of the remaining liquid phase increased to above 1300°C and γ-T_0; Partitioning then occurred and the liquid solidified the same as what was shown in the region 2 of Fig. 77 (a).

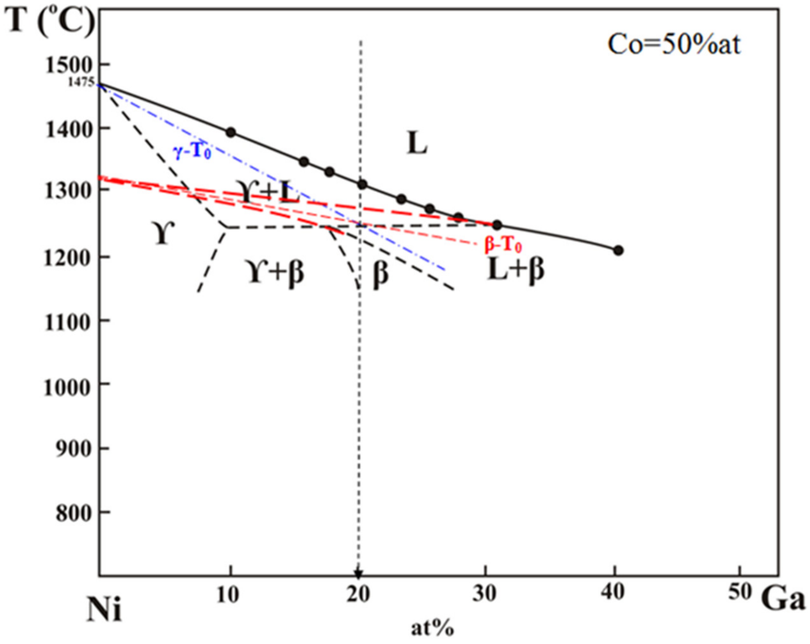

Fig. 79. A pseudo binary diagram for Co-Ni-Ga alloys containing 50 at% Co. The metastable extension of the liquidus and solidus lines and T_0 lines for the γ and β phases are alos shown. The dashed arrow shows the estimated critical composition, Ga= 20 at% , for partitionless solidification and solute entrapment due to supercooling effect during RS to form metastable single γ phase (below γ-T_0) in about Ga<20 (at%) and metastable single βphase (below β-T_0) in Ga>20 (at%) as described in the text.

Fig. 80 shows the microstructure of Co$_{50}$Ni$_{32.5}$Ga$_{17.5}$ (at%) alloy (R) which was slowly cooled with He+Ar gas flow during levitation. The sample consisted of primary γ dendrite and β interdendritic phase as the matrix phase. Likewise, in this sample, γ phase dendrite formed first and the interdendritic β phase developed from the liquid phase through a peritectic reaction $L+\gamma\rightarrow \beta$. The dark areas in the microstructure are related to pores forming due to lack of the liquid access through the interdendritic arms spacing.

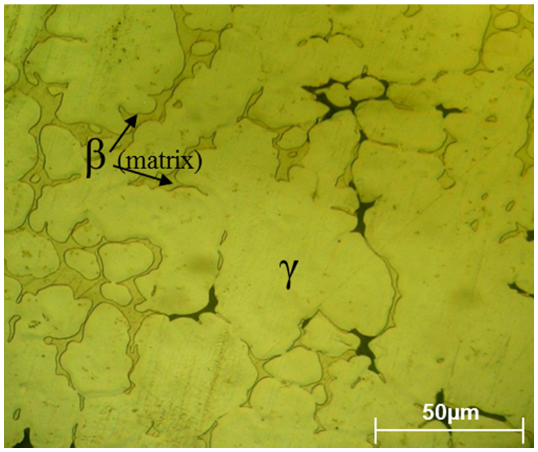

Fig. 80. Optical micrograph of $Co_{50}Ni_{32.5}Ga_{17.5}$ alloy (R) with γ phase (dendrites) and β (matrix) phases in slow cooled and solidified with Ar+He in levitation. The dark areas in the microstructure are related to the pores (see text).

Two different microstructures for $Co_{50}Ni_{30}Ga_{20}$ (at%) alloy (H) have been shown in Fig. 81. Microstructure of the sample quenched from T_L (H1) consisted of γ dendrite embedded in β, which was transformed to martensite (β'), as shown in Fig. 81 (a). On the other hand, single metastable γ phase formation during rapid solidification in the supercooled (ΔT= 60°C) $Co_{50}Ni_{30}Ga_{20}$ (at%) sample (H2) (Fig. 81 (b)) was similar to that for the $Co_{50}Ni_{35}Ga_{15}$ (at%) sample (S) (Fig. 78 (b)). It is worth noting that the single metastable β phase can also form thermodynamically in this supercooling degree based on β-T_0 line in Fig. 79, but kinetically the single metastable γ phase forms first.

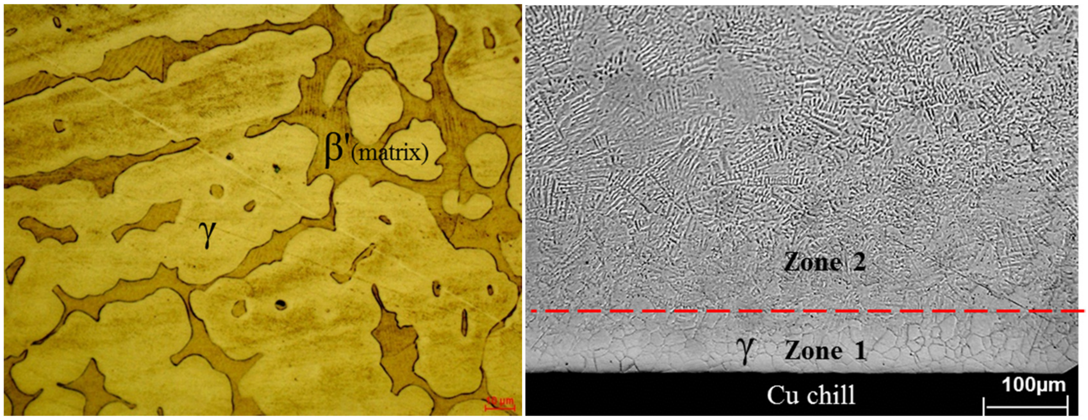

(a) (b)

Fig. 81. Optical micrographs of $Co_{50}Ni_{30}Ga_{20}$ (H) samples (a) β' (martensite)+ γ (dendrites) phases in quenched sample from T_L (H1) (b) two zones area in the supercooled and quecnched sample (H2), zone 1- single metastable γ phase forming on near Cu-chill region from 60°C supercooled liquid, zone 2- $\gamma+\beta$ phase region.

For further investigation of the solidification parameters and microstructural observation of $Co_{50}Ni_{30}Ga_{20}$ (at%) series alloy (H), two samples in different thermal conditions have been shown in Fig. 82. $\beta+\gamma$ phase micorstructure with coarser primary γ denderites in the sample dropped from S+L region (H3) can be observed in Fig. 82 (a). Similar to the sample with 60°C supercooling (H2), the micorostructure of $Co_{50}Ni_{30}Ga_{20}$ (at%) alloy with the lower supercooling (H4) also had two zones. As indicated in Fig. 82 (b), zone 1 consisited of a metastable γ phase forming close to the Cu-chill region from 45°C supercooled liquid and zone 2 contained $\beta+\gamma$ phase region. In this sample with lower supercooling (45°C) the single metastable γ phase with the same composition as the parent phase can still form near the contact area with the Cu-chill due to rapid solidification (as explained earlier in this chapter). $\beta+\ \gamma$ phase region built up on the top of that single metastable γ phase after sample hitting the Cu-chill and releasing the laten heat ofthe first solidfied part. This latent heat rises the temperature well above the peritectic temperature and γ-L T_0, and partitioning takes place with the solidifying liquid, the same way as shown in Fig. 82 (a).

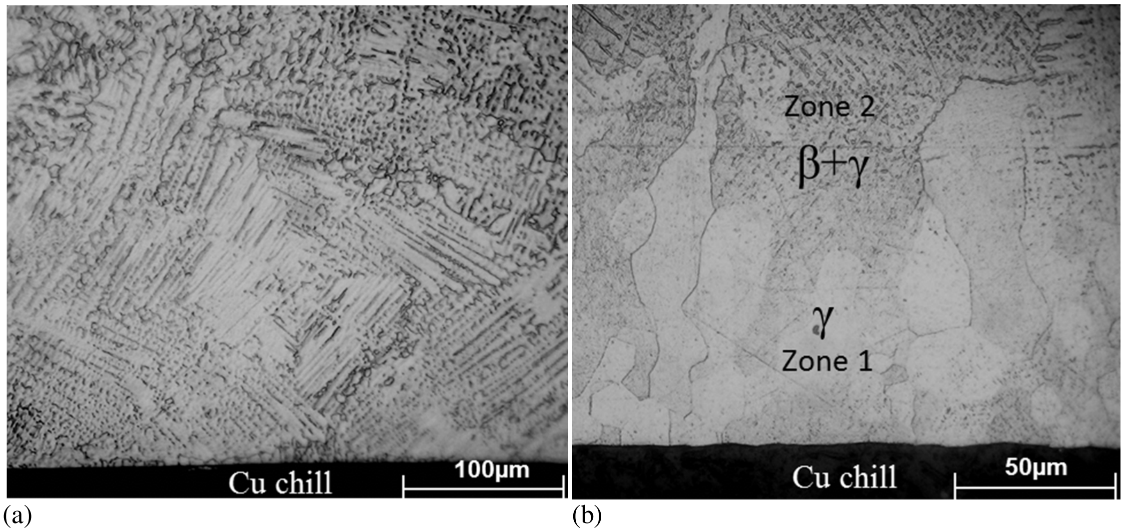

(a) (b)

Fig. 82. Optical micrographs of $Co_{50}Ni_{30}Ga_{20}$ (H) samples in two different thermal conditions. (a) β+γ phase micorstructure with well dvloped primary γ denderites in dropped sample from S+L (H3) (b) Two zones, zone 1- single metastable γ phase forming on Cu-chill from 45°C supercooled liquid, zone 2- β+ γ phase region (H4).

The microstructure of $Co_{50}Ni_{27.5}Ga_{22.5}$ (P) alloy quenched from the liquidus temperature (T_L) for near and far distances from the Cu-chill which are manifesting different cooling rates in the sample have been shown in Fig. 83. Microstructure of fine β+γ phase (with primary γ denderites) close to the Cu-chill (faster cooling rate) in Fig. 83 (a) might sugesst a precursor phenomenon before martensitic transformation which has also been reported by other researchers [157, 158], however, no sign of forming martensitic microstructure was detected in the entire sample. Fig. 83 (b) displays the coarse γ dendrites as well as the β matrix that was formed through the peritectic reaction in this sample.

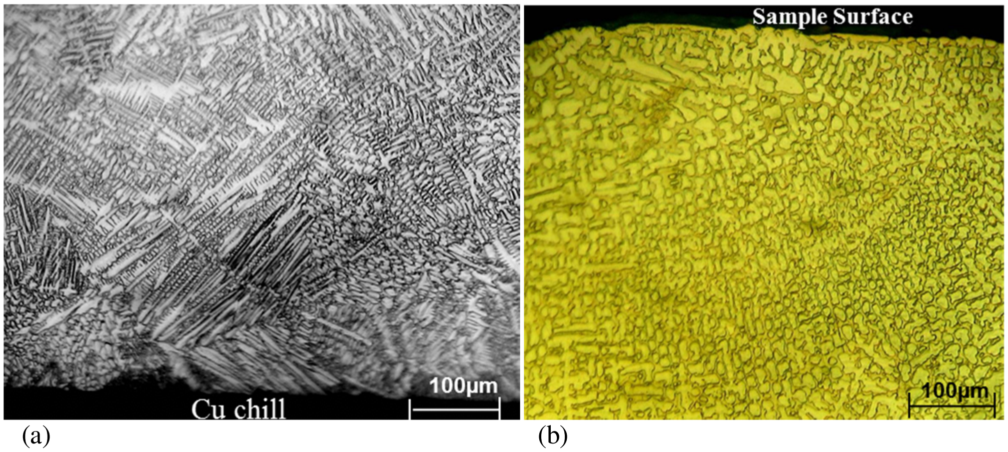

(a) (b)

Fig. 83. Microstructure of $Co_{50}Ni_{27.5}Ga_{22.5}$ (P) alloy quenched from about T_L has shown here in different distance from Cu-chill (manifesting different cooling rates). (a) fine lamellar $\beta+\gamma$ phase micorstructure (with primary γ denderites) near to Cu-chill (faster cooling rate). (b) coarse $\beta+\gamma$ phase region near to the sample surface (slower cooling rate).

Optical micrographs of the stoichiometric composition of a series of $Co_{50}Ni_{25}Ga_{25}$ *Heusler* alloys (A) quenched from different thermal conditions are shown through Fig. 82 to Fig. 86. Fig. 84 (a-d) shows different microstructures in a $Co_{50}Ni_{25}Ga_{25}$ alloy (A1) quenched from about T_L, appeared in different distances from the Cu-chill manifesting different cooling rates. The lower portion in Fig. 84 (a) solidified near the chill surface, consisting of β single parent phase matrix with the precipitates of the secondory γ phase while the upper portion contains primary γ denderites and interdendritic β phase. Microstrucure of the lower portion in the Fig. 84 (a) consists of γ precipitates in fully decorated-shape grain boundraies as well as small dispersed γ particles whithin the parent phase (β) matrix. This microstructure progressively develops during a solid state transformation after the first single β phase (metastable) has forrned on the contact surface of the Cu-chill, and heated up as the latent heat is released from the solidfied part and annealed metastable single β phase. A higher magnification of the interface between two different lower and upper regions is shown in Fig. 84 (b). Fine equiaxed γ grains and β' (marrtensitic β) matrix phase microstructue near to the top of the two-region interface demonstrated in Fig. 84 (c) formed during the rapid soildifiication (after latent heat was released from the first solidified part) of the liquid on top of the single metastable β phase. Fig. 84 (d) shows primary dendrite γ phase embeded in β' (marrtensitic β) matrix for the reamined part farther from Cu-chill which agrees well with the results of the previous part. Both β and β' (mertensitic β) phases in this microstructure were ductile and there were no sign of any severe cracking on the grain boundaries.

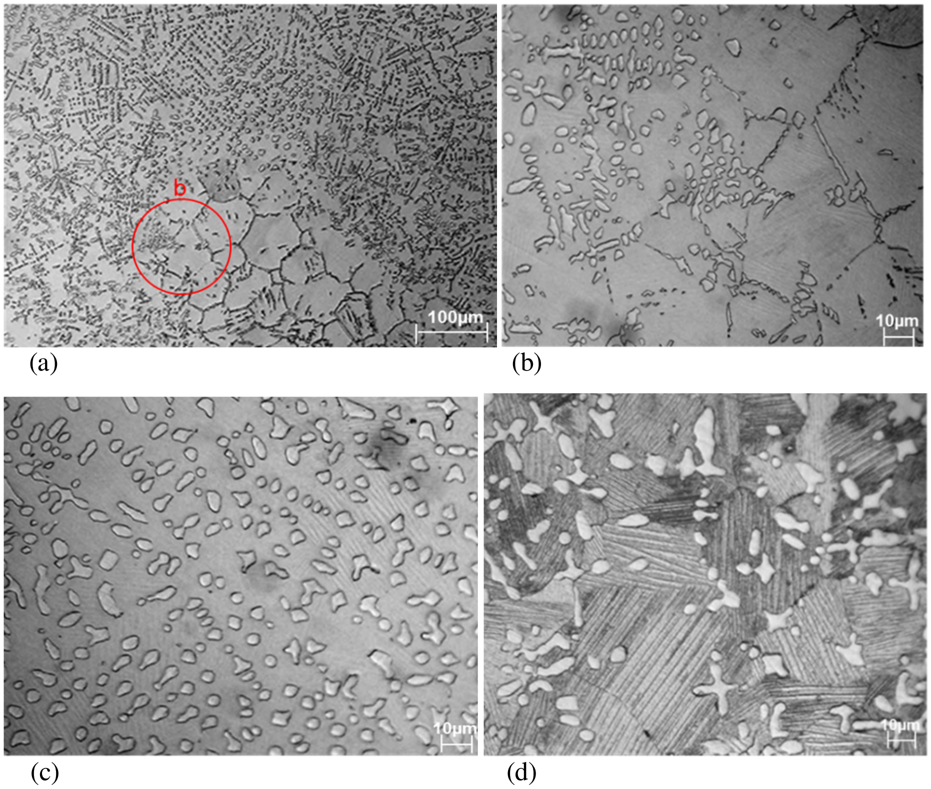

(a) (b)

(c) (d)

Fig. 84. Optical micrographs of Co$_{50}$Ni$_{25}$Ga$_{25}$(A1) alloy quenched from about $T_L$at different distances from Cu-chill (manifesting different cooling rates)(a) The lower portion solidified near the chill surface, consists of single β parent phase matrix with the precipitates of the secondory γ phase. The upper portion contains primary γ denderites and interdendritic β phase (b) A higher magnification of interface between two different regions (c) Fine equiaxed γ grains and β'(marrtensitic β) matrix near to the top of two-region interface (d) Primary dendrite γ phase embeded in β'(marrtensitic β) matrix in well farther part from Cu-chill.

Dendritic microstructure of primary *γ* phase and interdendritic *β* matrix of $Co_{50}Ni_{25}Ga_{25}$ alloy quenched from S+L region at 1200°C (A2) is shown in Fig. 85. As mentioned before, Co-Ni-Ga alloys with Ga contents less than 30 at% Ga solidfy through a peritectic reaction L+γ→ β in which *γ* is the primary phase and *β* is the matrix phase.

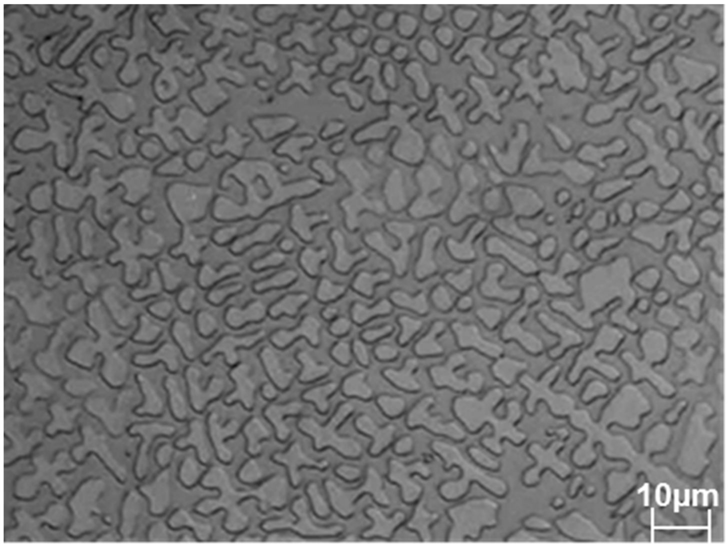

Fig. 85. Dendritic microstructure of primary *γ* phase and interdendritic *β* matrix of $Co_{50}Ni_{25}Ga_{25}$ alloy dropped from *S*+*L* (A2).

Optical micrographs of the $Co_{50}Ni_{25}Ga_{25}$ alloy solidified near the chill with Δ*T*= 76°C supercooling (A3) is shown in Fig. 86. Metastable single *β* phase forms on the surface of the Cu-chill from the supercooled liquid. This metastable single *β* phase has formed with the same composition as the parental phase i.e. 50%Co-25%Ni-25%Co. In contrast with the single *β* (or *β*') phase with higher than 30 at% Ga content in the results of the privious part, no cracks or intergranular precipitations were observed in the microstructure of the metaastable single *β* phase in this supercooled and quenched $Co_{50}Ni_{25}Ga_{25}$ sample (A3). This is the minimum Ga content metastable single *β* phase (or *β*') among all *Heusler*

(Co_2NiGa) compounds or colse compositions, which has been never reported before by other research groups working on Co-Ni-Ga FSMAs.

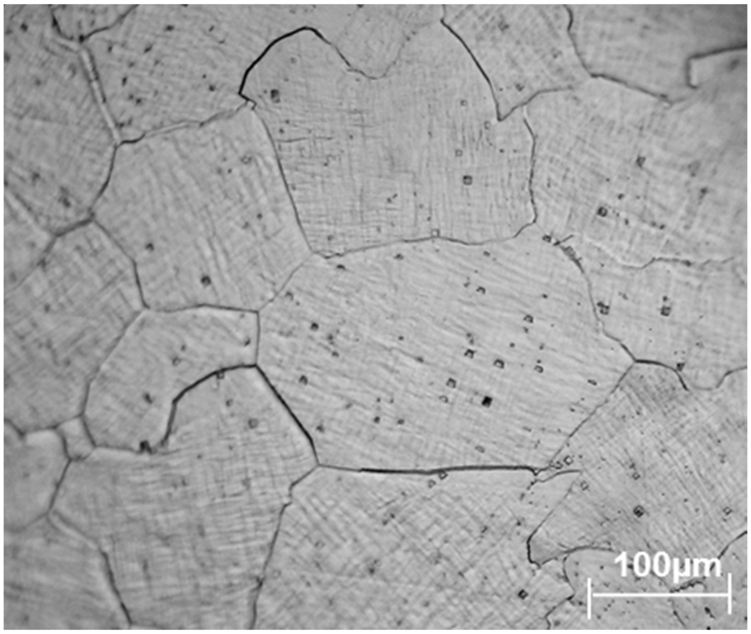

Fig. 86. Optical micrographs of $Co_{50}Ni_{25}Ga_{25}$ (A3) alloy solidified near the chill with ΔT= 76°C supercooling, single metastable β phase forming on the surface of Cu-chill from supercooled liquid.

It is imortant to note that in the microstructure of single metastable β phase in Fig. 86, some blocky precipitates dispersed in the matrix. Based on Liu *et al.* report [137] for $Co_{50}Ni_{20}Ga_{30}$ alloy after solution treated at 800°C for 4h and quenched in water, there were also some blocky particles with cubic or tetrahedran morphologies. They indexed these blocky particles as minor Ni_3Ga(or Co_3Ga) peaks realted to γ' phase in their X-ray diffraction results and claimed the ordering of γ phase can happen upon annealing in the composition far from the Co corner in the Co-Ni-Ga ternary phase diagram. Here, after the metastable single β phase formation from the supercooled liquid on the Cu-chill surface, these blocky particles in the microstructure were formed during a solid state transformation, which occurs after the first single β phase (metastable) has forrned on the contact surface of the Cu-chill and heated up as the latent heat is released from the solidfied part and anneals the metastable single β phase. Metastable single β phase formation in supercooled (ΔT= 147°C) $Co_{50}Ni_{22.5}Ga_{27.5}$ sample (O) near to the Cu-chill surface and β (matrix)+ γ (dendrite) phases microstructure (farther to the Cu-chill) are shown in Fig. 87. This supercooled $Co_{50}Ni_{22.5}Ga_{27.5}$ alloy include two different microstructural zones as shown in Fig. 87 (a) to (c). A metastable single β phase (Fig. 87 (b)) has developed widely and sufficiently due to a bulk supercooling (ΔT= 147°C) before solidification, and no grain boundaries crack were observed in the microstructure. As it was previously mentioned, when the supercooled liquid hits the Cu-chill surface, the first solid nucleates and forms at a temperature designated by T_{drop} (Table 4). Since this temperature is well below the T_0 for β, it will form partitionless, and in a solute entrapped form which has the same composition as the parent phase. After latent heat release rises the temperature above β-L T_0 and peritectic tempaeratures, the partitioning takes place with the liquid solidifies (Fig. 87(c)) in the same way as shown in Fig. 85 and Fig. 81 (a).

By increasing the Ga content from 10 up to 30 at%, the volume fraction of γ primary dendrites decrease gradually based on the proposed pseudo binary diagram in this study (Fig. 79), and eventually a single β phase with equiaxed grains is formed in the $Co_{50}Ni_{20}Ga_{30}$ (E series) samples (Fig. 88). Microstructure of the sample without any supercooling and quenched directly from its liquidus temperature (T_L) on a copper chill surface has a single *β* phase through the entire of cross section of the sample as shown in Fig. 88 (a).

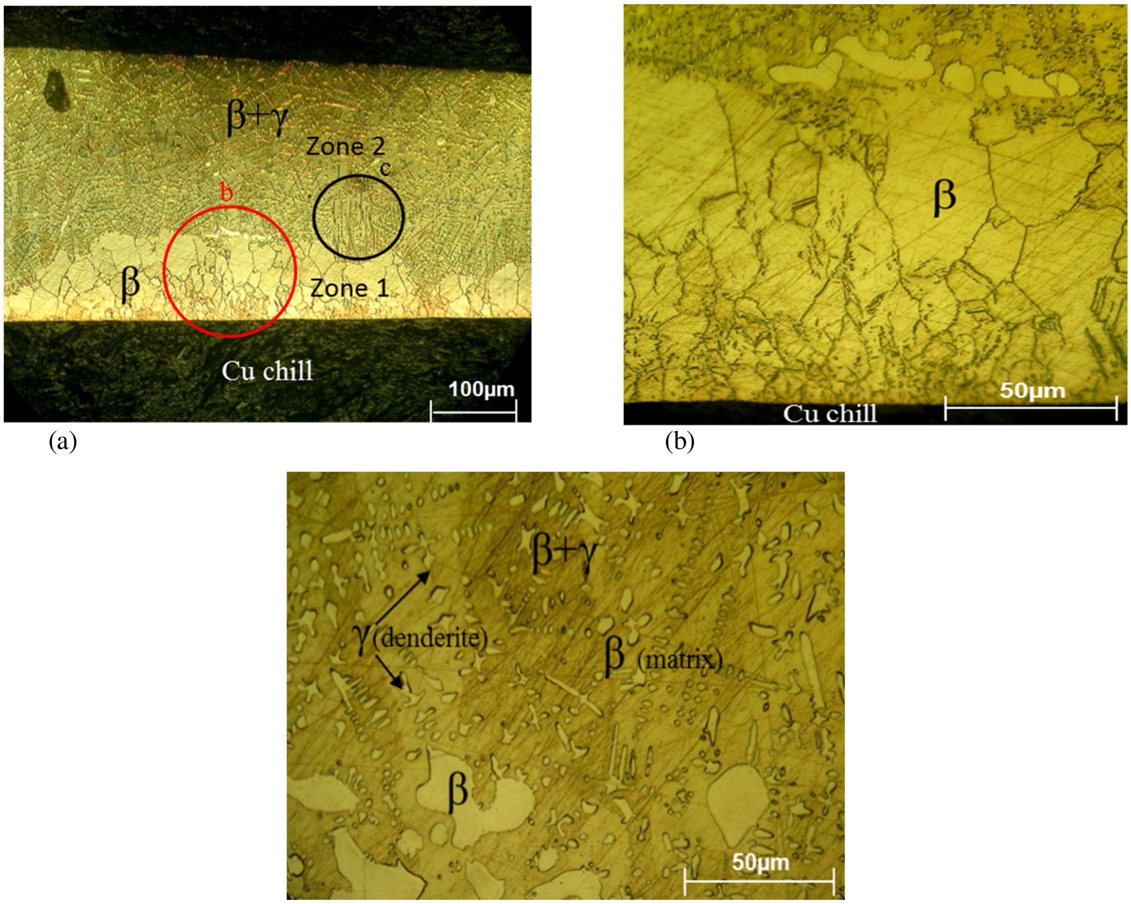

(a) (b)

(c)

Fig. 87. Metastable single β phase formation in ΔT=147°C supercooled $Co_{50}Ni_{22.5}Ga_{27.5}$ (O) sample. This supercooled $Co_{50}Ni_{22.5}Ga_{27.5}$ sample has a single *β* phase. (a) Two zones (b) single metastable β phase (near to the Cu-chill) and (c) *β* (matrix) +*γ* (dendrite) phases (farther to the Cu-chill).

The sample with ΔT= 54°C supercooling before quenching (E2) had the martensitic microstructure (*β*' phase) at room temperature. It seems that the martensitic microstructure forms due to a large internal stress induced by supercooling and high cooling rate during quenching sample on the surface of the Cu-chill. This effect can directly cause the martenstic transformation temperature to change in this sample that will be discussed later in martensitic transformation part.

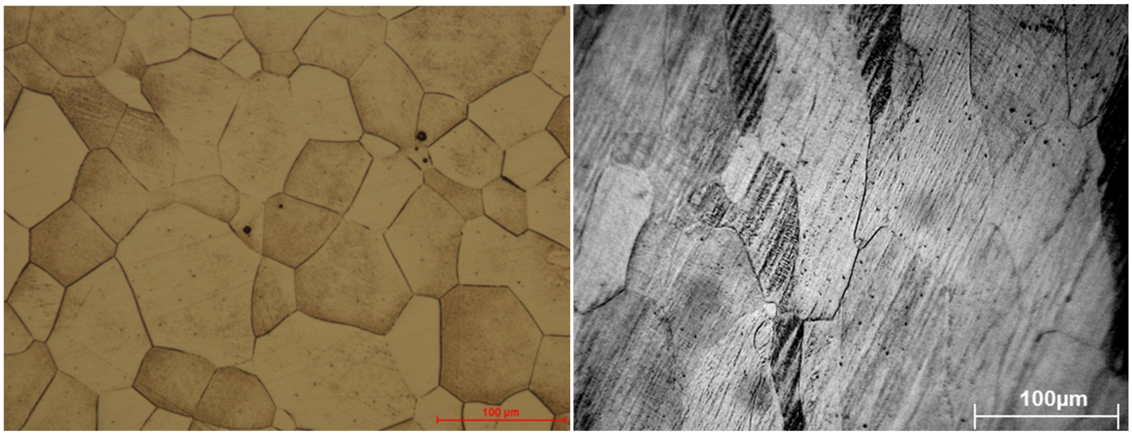

(a) (b)

Fig. 88. Single β phase formation through the entire cross section of $Co_{50}Ni_{20}Ga_{30}$ samples (E). (a) Quenched directly from T_L (E1) and (b) with ΔT= 54°C degree of supercooling before quenching (E2). The supercooled sample has the martensitic microstructure (β' phase) at room temperature.

The microstructure of the $Co_{50}Ni_{10}Ga_{40}$ alloy sample with 23°C degree supercooling before quenching the sample on a copper chill surface (F1) consists of a single β phase through the entire cross section of the sample as shown in Fig. 89. No severe grain boundaries microsegregation was observed in this sample. However, it was brittle with severe intergranular cracking and falling out grains at room temperature. In order to observe better grain boundaries microsegregation in this series, a sample which solidified during slow cooling at the levitation (with He+Ar gas flow), cooled to a temperature below of its liquidus (*S*+*L*), and solidified before hitting the Cu-chill surface was investigated. However, even in this sample with slow cooling rate, no severe grain boundaries microsegregation was detected, and the sample microstructure was simiar to the sample F1 as shown in Fig. 89.

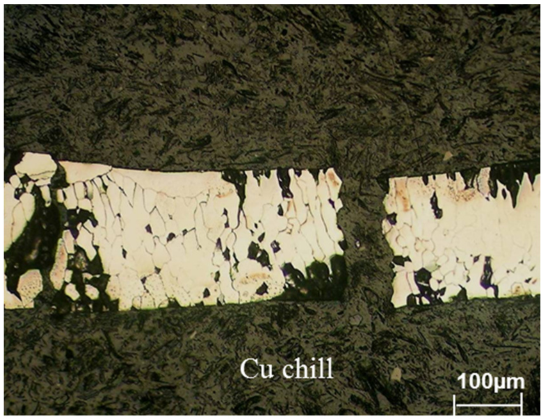

Fig. 89. Microstructure of $Co_{50}Ni_{10}Ga_{40}$ sample with ΔT= 26°C supercooling quenched on the Cu-chill (F1). Single β phase with sever intergranular cracking through the entire cross section of sample are shown.

3.4. Solidification Parameters and Microstructure of $Co_{100-2y}Ni_yGa_y$ (at%) Alloys

For investigating the effect of phase formation on microstructure of Co-Ni-Ga ternary alloys while the Ni and Ga amounts are the same (Ni/Ga ratio is one), $Co_{100-2y}Ni_yGa_y$ (y= 15, 20, 25, 27, 30 and 35) series of alloys were selected. By applying quenching temperatures (T_{Drop}) near to the liquidus temperatures ranges (T_L), different microstructures for this type of alloys have been studied. Table 5 shows all phase and thermal information for all samples in the $Co_{100-2y}Ni_yGa_y$ series. Here, in this series of Co-Ni-Ga alloys, a wide range of single γ, β and dual β+γ phases were observed as described below.

Fig. 91 shows $Co_{60}Ni_{15}Ga_{15}$ alloy with 15 at% Ga content quenched from T_L. Metastable γ phase can easily start to form in a very close area to the Cu-chill without any bulk supercooling before quenching (Fig. 91 (a)). In this alloy, the well-developed γ dendrite in β matrix phase can be seen in near distance to the Cu-chill (faster cooling rate) as well as coarse β+γ phase region near to the sample surface (slower cooling rate) (Fig. 91 (b)). Microstructue of $Co_{60}Ni_{20}Ga_{20}$ alloy (J) quenched from above T_L is shown in Fig. 90. Fig. 91 (a) shows the lower portion (zone1), solidified near the chill surface, which consists of metastable single γ phase similar to the $Co_{60}Ni_{15}Ga_{15}$ alloy microstructure in Fig. 90. The upper portion (zone 2) contains primary γ dendrite and interdenderitic β phase. Fine lamellar β (matrix)+ γ (dendrites) phases in micorstructure fartehr from the Cu-chill (slower cooling rate) is also exhibited in Fig. 91 (b). For both $Co_{60}Ni_{15}Ga_{15}$ and $Co_{60}Ni_{20}Ga_{20}$ alloys, the microstructures included γ and β phases.

Table 5. Nominal composition and condition of alloys in $Co_{100-2y}Ni_yGa_y$ (at%) series

Sample	**Composition (at%)**	**$T_{liquidus}$ (ºC)**	**T_{drop} (ºC)**	**Quenching**	**Observed Microstructure**
I	$Co_{70}Ni_{15}Ga_{15}$	1410	1410	Dropped on Cu-chill	Dual phases
J	$Co_{60}Ni_{20}Ga_{20}$	1298	1320	Dropped on Cu-chill	Single+Dual Phases (2 zones)
K	$Co_{40}Ni_{30}Ga_{30}$	1202	1211	Dropped on Cu-chill	Single Phase
L	$Co_{30}Ni_{35}Ga_{35}$	1196	1196	Dropped on Cu-chill	Dual Phases

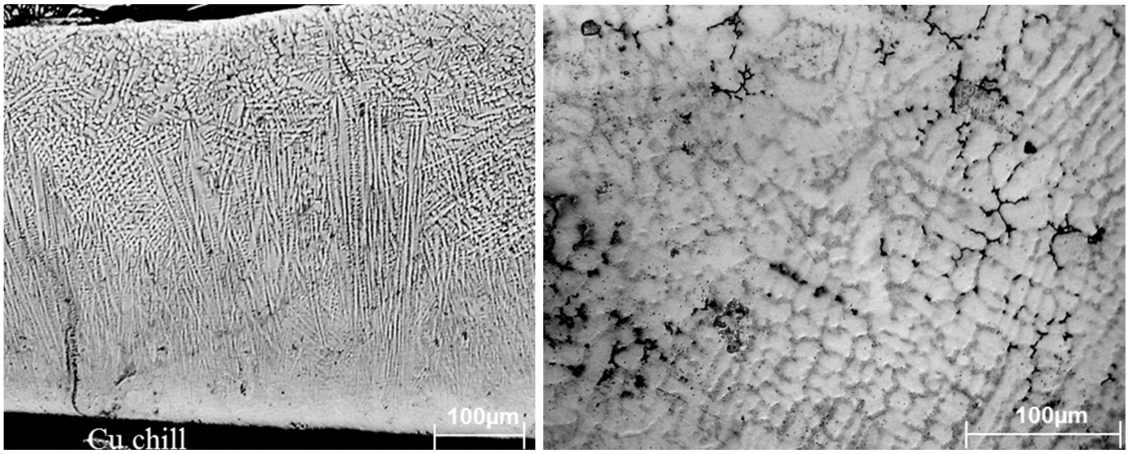

(a) (b)

Fig. 90. Optical micrographs of $Co_{70}Ni_{15}Ga_{15}$ alloy (I) quenched from T_L(a) fine lamellar β (matrix)+ γ (dendrites) phases in micorstructure near to the Cu-chill (faster cooling rate). (b) coarse β+ γ phase region near to the sample surface (slower cooling rate).

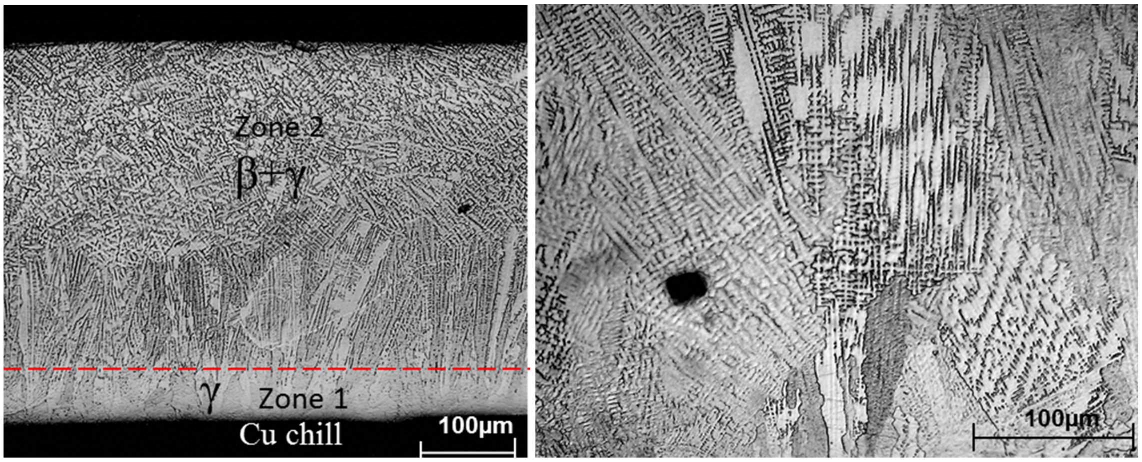

(a) (b)

Fig. 91. Optical micrographs of $Co_{60}Ni_{20}Ga_{20}$ alloy (J) quenched from above T_L. (a) The lower portion (zone 1), solidified near the chill surface, consists of a single γ phase. The upper portion (zone 2) contains primary γ dendrite and interdenderitic β phase. (b) A higher magnification of fine lamellar β (matrix)+ γ (dendrites) phases in micorstructure fartehr from the Cu-chill (slower cooling rate).

However, by incresing the Ga at% amount up to 30 at% in this series i.e. $Co_{40}Ni_{30}Ga_{30}$ alloy (K) quenched from T_L, again a brittle single martensitic phase (β') forms through the entire sample cross sectional microstructure regardless of the different cooling rate effect (distance from the Cu-chill) as shown in Fig. 92. Microstructure of the $Co_{40}Ni_{30}Ga_{30}$ alloy

(K) shows fine and equiaxed grains which caused fallen-off grains (Fig. 92 (a)), and columnar grains (Fig. 92 (b)) of a paramagnetic brittle martensitic phase (single β' phase) at room temperature in close and far distances from the Cu-chill through the entire of its cross section, respectively.

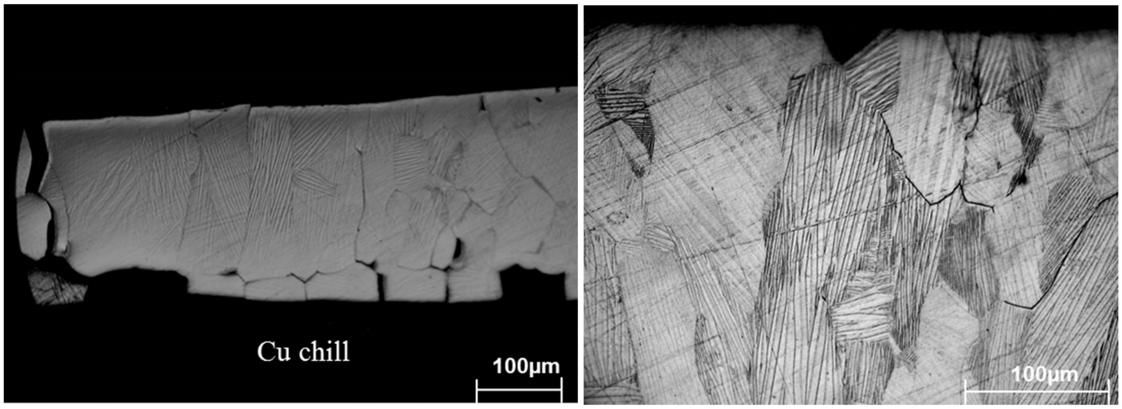

(a) (b)

Fig. 92. Optical micrographs of $Co_{40}Ni_{30}Ga_{30}$ alloy (K) quenched from T_L. (a) Developed a brittle martensitic microstructure (single β' phase) through the entire of the cross section. (b) A higher magnification of martensitic micorstructure

Microstructure of $Co_{30}Ni_{35}Ga_{35}$ (L), a quenched sample from T_L, is shown in Fig. 93. Fig. 93 (a) indicates fine and equiaxed grains of the single martensitic phase (β' phase) in close diatnce from the Cu-chil which caused fallen-off grains in the microstructure at RT. Fig. 92 (b) also exhibits columnar grains of the single martensitic phase (β' phase) through the entire sample cross section in far diatnce from the Cu-chill at RT, as well as a dark intergranular phase. The martenistic phase formed in this sample is in a paramagnetic state at RT, and aslo shows high brittleness. EDS analysis revealed that the chemical composition of this inetrgranular phase composed of 52%Ga-26%Ni-22%Co which probably forms a Ga_2NiCo intermetalic (Ga-rich) phase in the ternary Co-Ni-Ga system. SEM micrograph of the intergranular Ga-rich (Ga_2NiCo) in higher magnification has been illustrated in Fig. 92 (c).

The intergranular Ga-rich (Ga_2NiCo) phase can form in farther distance from the Cu-chill (Fig. 93 (b) and (c)) due to slower cooling rates from S+L region (showing microsegregation), and leaded directly to the formation of this Ga-rich phase through the conventional solidification path. However, this Ga-rich phase is also very brittle and forms intergranular cracking in the sample during microsegregation, and cannot improve the martensite phase brittleness like γ (Co-rich) phase.There was no sign of γ' phase existence in $Co_{30}Ni_{35}Ga_{35}$ (L) alloy.

The morphology and volume fraction for each phase in this series not only strongly depended to the alloy composition, but also was closely related to the solidification process and subsequent treatment. The volume fraction of primary γ decreased gradually by increasing the Ga content, and eventually metastable single β (or β') phase was found in the $Co_{50}Ni_{25}Ga_{25}$ and $Co_{46}Ni_{27}Ga_{27}$ with ΔT= 76°C and ΔT= 143°C bulk supercooling, respectively. In this series of Ni/Ga equal ratio, the single β phase which goes to a martensitic phase (β') can form in the $Co_{40}Ni_{30}Ga_{30}$ alloy (K) samples quenched from T_L (without bulk supercooling) on the Cu-chill but this single β (or martensitic β') phase is in paramagnetic state at RT.

Here the cooling rate for the Cu-chill is about 800-900°C/s, therefore, high temperature phase structure in these alloys could be retained in quenched samples from T_L. As shown in Fig. 76, the ternary phase diagram, which proposed at 1150°C is good enough to predict microstructure for each alloy in rapid solidification conditions.

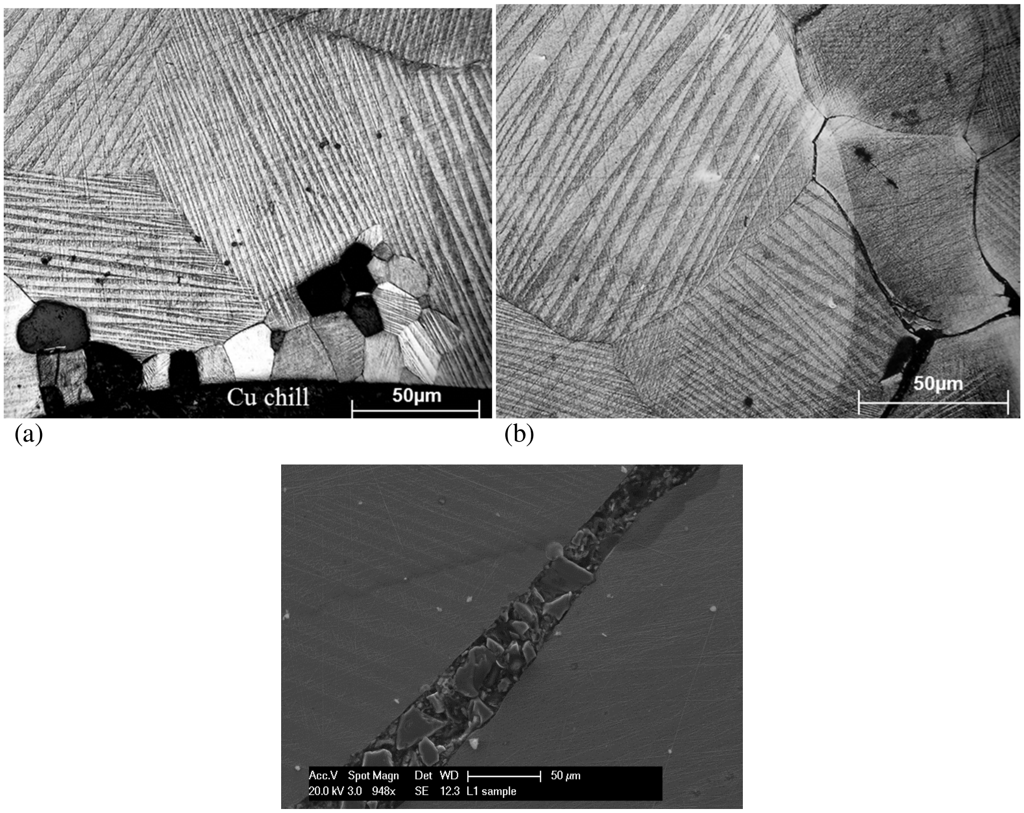

(a) (b)

(c)

Fig. 93. Optical micrographs of $Co_{30}Ni_{35}Ga_{35}$ alloy (L) sample dropped from about T_L, (a) martenstic microstructure (β') for contact surface with Cu-chill (b) β' (martensic phase) and dark intergranular Ga-rich(Ga_2NiCo) phase (farther to the Cu-chill) (c) SEM micrograph in higher magnification for intergranular Ga-rich (Ga_2NiCo) brittle phase in (b).

3.4.1. Martensitic Transformation in $Co_{50}Ni_{50-x}Ga_x$ (at%) Alloys

The DSC curves for $Co_{50}Ni_{35}Ga_{15}$ (S) and supercooled $Co_{50}Ni_3Ga_{20}$ (H4) samples are shown in Fig. 94 (a) and (b), respectively. There was no endothermic or exothermic peak presenting any phase transformation in both samples in 10°C/min continuous heating/ cooling (four cycles) cycling with progressively rising the maximum temperature on each cycle to 200, 250, 300 and 350°C (from -90 to 350°C on DSC graphs). Both $Co_{50}Ni_{35}Ga_{15}$ (S) and $Co_{50}Ni_{30}Ga_{20}$ (H4) had metastable γ single phase in their microstructure (zone 1 in two-zone samples).

Based on this observation and sample microstructures from the previous part, it seems that the metastable *γ* phase and *β* phase have no phase transformation in these series of alloys at this range of temperature (up to 350°C). In these samples, S and H4, with the dual phase (*β*+ *γ*) microstructures, as was shown in Fig. 78 and Fig. 82 (b), the martensitic phase was not observed in most of the microstructures at RT. As discussed before, due to the presence of single *γ* phase in their microstructures, the austenite to martensite and reverse phase transformation could not exist or would be suppressed to far below room temperatures. This phenomenon was also observed in the cyclic DSC curves in Fig. 94.

For the $Co_{50}Ni_{25}Ga_{25}$ alloy with metastable single *β* phase in the microstructure (A3), there were no clear signs of martensitic transformations in the continuous cycling from -90 to 350°C at sequential increasing of temperatures in the DSC graphs for maximum 200, 250, 300 and 350°C temperatures. Craciunescu *et al.*, also reported a very wide shift (-100 to 0°C) in the transition temperature range for a two-phase $Co_{50}Ni_{25}Ga_{25}$ single crystal in different heat treating conditions [17]. They reported only an increase in the martensitic transformation of annealed and water-quenched samples in comparison with those (at the same temperature) slow coolinged following annealing. However, there was no microstructural observation in their work.

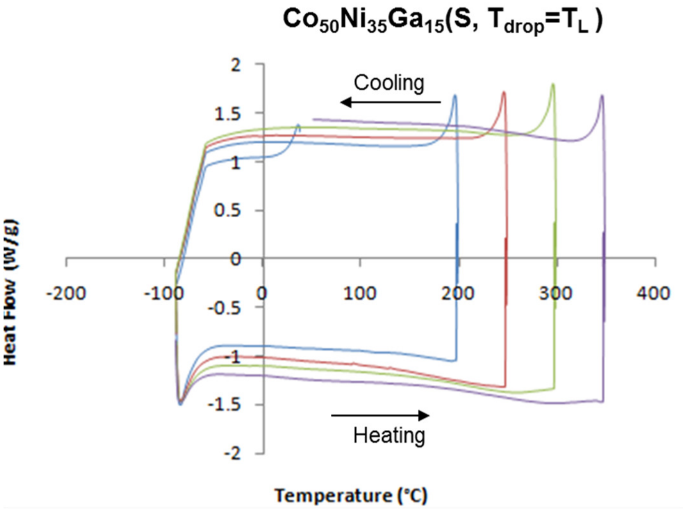

(a)

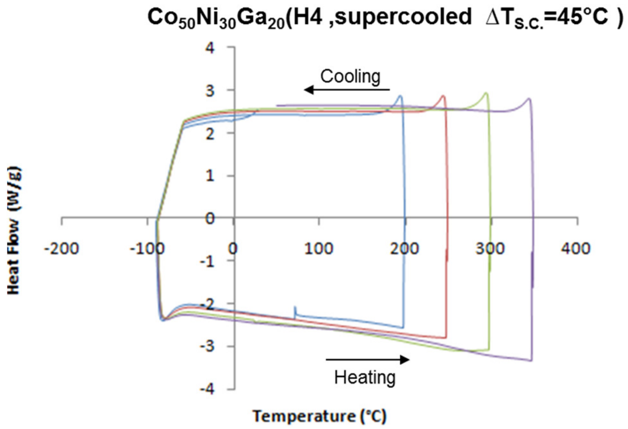

(b)

Fig. 94. DSC graphs of four heating/cooling cycles for (a) $Co_{50}Ni_{35}Ga_{15}$ (at%) sample quenched from the liquidus temperature (sample S) and (b) $Co_{50}N_{30}Ga_{20}$ (at%) sample quenched with Δ*T*= 45°C supercooling (sample H4).

Metastable single β phase, which can go to a martensitic transformation, was observed in the $Co_{50}Ni_{22.5}Ga_{27.5}$ sample quenched with 147°C supercooling (O) as shown in Fig. 87. Fig. 95 shows exothermic and endothermic peaks during cooling and heating cycles, respectively. It is believed that these peaks are corresponded to the martensitic and reverse transformation for the alloy at 10°C/min cooling/heating rate cycles. The austenite and martensite phase transformation temperatures. i.e. austenite starting transformation A_s, austenite finishing A_f, martensite starting M_s and martensite finishing M_f were determined by the cross point of the tangent line of the peaks inclination and baseline in the DSC curves at well above temperatures than RT as shown in Fig. 95 (arrows). The values were 110, 135, 65 and 40°C, respectively for the first heating/cooling cycle. Small downward shift of the martensitic transformation temperatures (M_{s1} and M_{f1}), about 5°C for each cycle, were observed during subsequent cooling cycles. The reverse transformation to austenite (A_{s1} and A_{f1}) also shifted downward with the same trend (about 5°C) for each cycle. Based on the DSC graphs in Fig. 95 for the supercooled $Co_{50}Ni_{22.5}Ga_{27.5}$ alloy (O) in the $Co_{50}Ni_{50-x}Ga_x$ series, the metastable single β phase in this sample, which undergoes a martensitic and reverse transformation during cyclic cooling and heating up to 350°C with a thermal hysteresis ΔT (A_f–M_s) about 70°C, has a proper thermal stability in this range of temperatures.

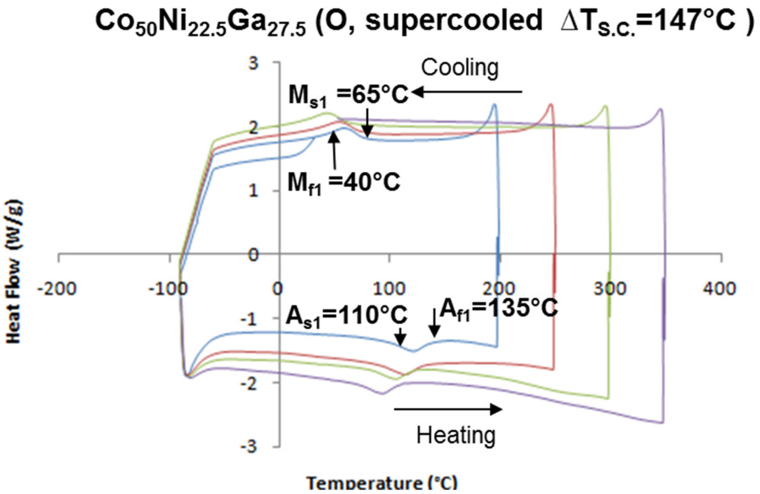

Fig. 95. DSC graphs of four heating/cooling cycles for $Co_{50}Ni_{22.5}Ga_{27.5}$ (at%) with ΔT= 147°C supercooling (sample O).

It is well known that there is a linear correlation between the valence electron concentration (*e*/*a*) ratio and martensitic starting temperature (M_s), which has been reffered as a key role in determining the martensitic transformation and parent phase formation in FSMAs. This concept has been widely used to describe approaching a propr marrtenstic transformation temperatures based on alloy chemical compositions in both single and dual-phase Co-Ni-Ga FSMAs, specifically in Cracinescue [17], Okiawa [12, 99] and Lie [152] works. In all of those reports, it was claimed that the M_s temperature increases with *e*/*a* ratio regardless of Ga content and the microstructure of alloys in both single and dual-phase Co-Ni-Ga FSMAs

In this sample with *e*/*a*= 7.575 in which the numbers of electron per atoms for Co, Ni and Ga are 9, 10 and 3 respectively, the M_s (= 65°C) does not accord with all of those previous findings. According to a recently released report [159, 161], however, there are other important factors related to the formation and thermal stability of parent phase, such as the Ga content and size factor [147] that need to be considered. They proposed a plot for M_s temperature as a function of both the *e*/*a* ratio and Ga content which shows higher M_s temperature for alloys with the same *e*/*a* ratio but higher Ga content. There is a good agreement between the measured M_s temperature for the metastable β phase in this sample (O) and their proposed plot.

The typical DSC curve for the sample $Co_{50}Ni_{20}Ga_{30}$ alloy dropped from T_L (E1) is shown in Fig. 96 (a). In contrast with the sample shown in Fig. 95, pronounced exothermic martensitic and endothermic austenite transformation peaks were not observed in this sample. However, there were small peaks in cooling and heating cycles that respectively show M_s (M_f) and A_f (A_s) to be around -55°C and -50°C. It should be noted that these transformation temperatures are close to those reported in Ref. [99] since there is only a single *β* phase in the microstructure for the same alloy composition as shown in Fig. 88(a). On the other hand, the $Co_{50}Ni_{20}Ga_{30}$ alloy with 54°C supercooling before quenching (E2) and martensitic (*β*') microstructure at RT (Fig. 88 (b)), had a very higher A_s(15°C) and A_f (about 55°C) as shown in Fig. 96 (b) than the sample without supercooling in a single cycle heating/cooling (10°C/m) for -90 up to 200°C. This phenomenon was also observed by Li *et al.* at their recent work [160]. This phenomenon is believed to be related to the internal stress induced by supercooling. Supercooling can cuases large internal stress introduced by rapid solidification, and when it rises large enough, induces martensitic transformation in the alloy as ab external stress does. The mentioned phenomenon caused an increase in A_f to about 55°C which made it possible to observe martenstic microstructure at RT (Fig. 96 (b)).

The DSC curves of the same sample (E1) in sequential heating/cooling cycles for maximum temperatures of 200, 250, 300, 350°C are shown in Fig. 96 (c). During the first cooling/heating cycle, the martensite and reverse martensite transformation peaks were observed near the same temperatures as in the Ref [99]. However, no martensitic transformation was observed during the cooling cycle even through the sample was cooled to -90°C. The subsequent cycles were also devoid of martensitic or austenitic transformations. This may occur since the martensitic transformation did not exist anymore at this composition or because of the suppression of the martensite transformation temperature in well below -90°C.

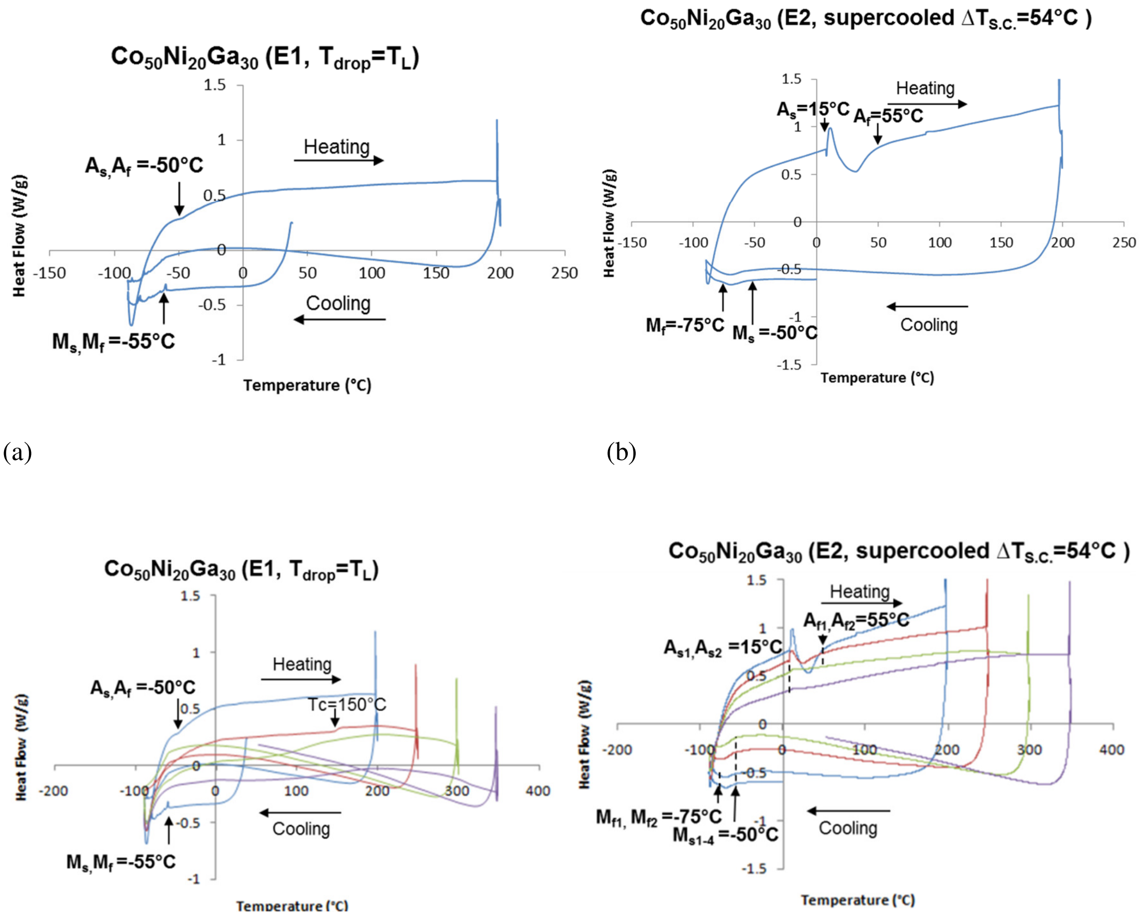

(a) (b)

(c) (d)

Fig. 96. DSC graphs of (a) single heating/cooling cycle for $Co_{50}Ni_{20}Ga_{30}$ (at%) sample quenched from the liquidus temperature (sample E1), (b) single heating/cooling cycle for $Co_{50}Ni_{20}Ga_{30}$ (at%) sample with ΔT= 45°C supercooling (sample E2), (c) fourheating/cooling cycles for sample E1 and (d) four heating/cooling cycles for sample E2.

Likewise, the typical DSC curves for sample E2 in sequential heating/cooling cycles for maximum temperatures of 200, 250, 300, 350°C are shown in Fig. 96 (d). In contrast with the sample E1 depicted in Fig. 96 (c), pronounced endothermic austenite transformation peaks, A_s and A_f, around 15 to 55°C were observed in the first (up to 200°C) and second (up to 250°C) heating cycles in this supercooled sample. However, compared to the first cycle, less pronounced peaks for the reverse martensitic transformation temperatures (A_s and A_f) were observed in the second cycle. This endothermic peak for reverse martensitic transformation broadened in the third heating cycle up to 300°C and almost disappeared following the last heating cycle up to 350°C.

The heatin/cooling DSC curves for the $Co_{70}Ni_{15}Ga_{15}$ sample quenched from T_L (I) in sequential cycles for maximum temperatures of 200, 250, 300, 350°C are shown in Fig. 97. As shown in the figure, there were no endothermic or exothermic peak in the cycles. Based on this observation and dual phase (γ+ β) microstructure of this sample as shown in Fig. 90, there is no phase change or transformations detected by DSC graphs in none of γ (dendrites) or β (matrix) phase in this $Co_{70}Ni_{15}Ga_{15}$sample quecnched from the liquidus temperature.

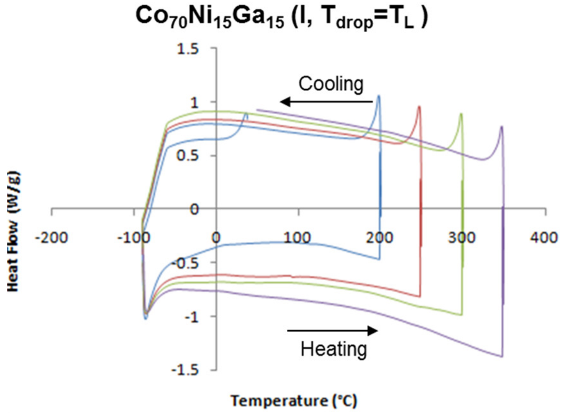

Fig. 97. DSC graphs of four heating/cooling cycles for $Co_{70}Ni_{15}Ga_{15}$ (at%) sample quenched from the liquidus temperature (sample I).

The DSC curves for $Co_{40}Ni_{30}Ga_{30}$ sample dropped from T_L (K) are shown in Fig. 98 (a) and (b) for two different heating/cooling rates of 10 and 20°C/min. Broad exothermic and sharp endothermic peaks are observed during cooling and heating cycle, respectively, for a range from -90°C to 550°C as demonstrated in Fig. 98 (a). Values of 470, 495 and

150°C, were obtained for A_s, A_f and M_s (= M_f), respectively, in the first heating/cooling cycle with 10°C/m rate. Based on this DSC curve (Fig. 98 (a)), the $Co_{40}Ni_{30}Ga_{30}$ alloy (K) with a single phase microstructure at RT (Fig. 92) had a very high reverse martensitic transformation temperatures (*As* and *Af*) showing a thermaly stable martensite phase in the sample at high temperature (about 500°C). Obvious downward shift in the pronounced exothermic peak of the martensitic transformation starting temperature (M_s), about 220°C from the first cycle (M_{s1}= 220°C) to second and third cycles ($M_{s2\text{-}3}$= 200°C) with 20°C/m rate were observed during subsequent cooling cycles (Fig. 98 (b)). The reverse transformation to austenite (A_s and A_f) also shifted downward but with a larger degree. For example, A_{s1} changed from 470°C in the first cycle to 420°C in the second cycle (A_{s2}), and disappeared in the third cycle. In the same way, A_{f1} in the first cycle (495°C) decreased about 45°C (A_{f2}= 450) in the second heating cycle, and eventually disappeared in the third cycle. It is believed that this phenomenon can happen due to the decomposition of single martensitic phase during continuous heating and annealing condition up to the 550°C.

The 10°C/m heating cycle suppressed the martensitic transformation temperatures to 150°C (shallow and broad peak in Fig. 98 (a)), however, it was suppressed less severely (Fig. 98 (b)) by increasing heating/cooling rate to 20°C/m for the first cycle (M_{s1}= 220°C, M_{f1}= 150°C) as well as for the following cycles ($M_{s2\text{-}3}$= 200°C, $M_{f2\text{-}3}$= 150°C). The reverse transformation to austenite temperatures in the first cycle in Fig. 98 (b) (A_{s1}=470°C and A_{f1}= 495°C) shifted downward, and continued with a larger degree of about 50°C in the second one (A_{s2}= 420°C and A_{f1}= 450°C), and eventually disappeared in last cycle due to decomposition of martensitic matrix phase. It can be seen in this alloy with 30 at% Ga content and constant Ni/Ga= 1 ratio which has *e*/*a* = 7.5, M_s (220°C) does not follow the linear dependency of martensitic transformation temperature to *e*/*a* based on previous reports [17].

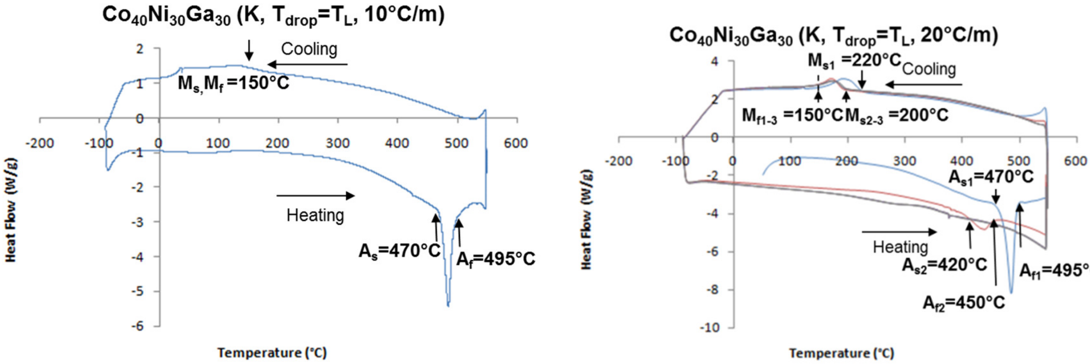

(a) (b)

Fig. 98. DSC graphs of (a) single heating/cooling cycle with 10°C/m rate for $Co_{40}Ni_{30}Ga_{30}$ (at%) sample quenched from the liquidus temperature (sample K) and (b) three heating/cooling cycles with 20°C/m rate for sample K.

Similar observation for Co-Ni-Ga with the same ratio of Ni/Ga (25/30) and different Co amount has been also reported by Liu *et al.* [147]. The M_s temperature dependency to *e*/*a* ratio and magnetic valence number plot for different Ga amount which is proposed in Ref [159, 161] again agrees with this result.

The $Co_{30}Ni_{35}Ga_{35}$ (L) sample quenched from the liquidus temperatue (T_L), has a brittle single martensitic phase (*β*') through the entire micortucture as shown in Fig. 93, however, it was too brittle to do sample preparing out of it for DSC test.

3.5. Summary

All the observations in this study have been summarized in Table 6 and 7. Table 6 shows a summary of results for $Co_{50}Ni_{50-x}Ga_x$ (at%) alloy series with x ranging from 10 to 50, and Table 7 presents the observations for $Co_{100-2y}Ni_yGa_y$ (at%) with y ranging from15 to 35 as well as near *Heusler-type* $Co_{46}Ni_{27}Ga_{27}$ and $Co_{48}Ni_{22}Ga_{30}$ (at%) compositions. The sample composition, martensitic transformation temperatures (for those that showed martensitic phase transformation), ductility (in general terms and in comparison to Ni-Mn-Ga alloys), magnetic state at room temperature (ferromagnetic or paramagnetic) as well as valance electron per atom ratios have been given. In addition, the influence of the electron/atom (*e*/*a*) ratio on the M_s temperature in Co-Ni-Ga alloys has been demonstrated in Fig. 99. Obvious difference with the previous work's results were observed for the martensitic starting temperatures of the $Co_{40}Ni_{30}Ga_{30}$ sample K (M_s= 7.5 *e*/*a*) and the $Co_{50}Ni_{22.5}Ga_{27.5}$ sample O (M_s= 7.75 *e*/*a*).

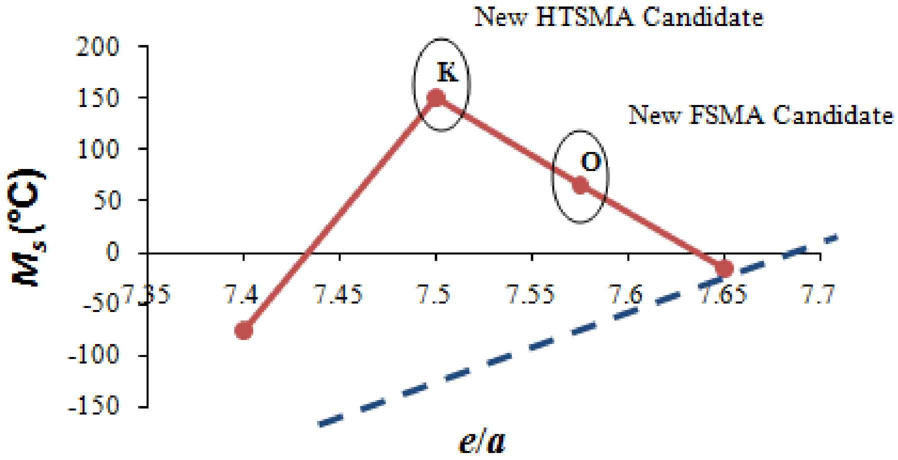

Fig. 99. The influence of the electron/atom (*e*/*a*) ratio on the *Ms* temperature in Co-Ni-Ga alloys. The solid line displays the observations of the current study, and the dashed line shows findings of other works (*e*/*a*: 7.4-8.2) [17].

Table 6. Results for $Co_{100-2y}Ni_yGa_y$ (at%) with y ranging from15 to 35 and near *Heusler-type* $Co_{46}Ni_{27}Ga_{27}$ and $Co_{48}Ni_{22}Ga_{30}$ (at%) compositions

Sample	**Composition (at%)**	M_s (°C)	M_f (°C)	A_s (°C)	A_f (°C)	**Microstructure (RT)**	**Ductility**	**Magnetic Status (RT)**	***e/a***
I	$Co_{70}Ni_{15}Ga_{15}$ (y= 15)	-	-	-	-	Dual phases ($\gamma+\beta$)	DD	F	8.25
J	$Co_{60}Ni_{20}Ga_{20}$ (y= 20)	-	-	-	-	Singleγ+Dual Phases ($\gamma+\beta$)	DD	F	8.00
C11	$Co_{46}Ni_{27}Ga_{27}$ (y= 27)	-15	-15	-6	-6	Singleβ+Dual Phases ($\gamma+\beta$)	D	F	7.65
K	$Co_{40}Ni_{30}Ga_{30}$ (y= 30)	150	150	470	495	Single β' Phase	B	F/P	7.50
D1	$Co_{46}Ni_{27}Ga_{27}$ (Ga=30)	37.5	6	60	95	Single β' Phase	B	F/P	7.42
L	$Co_{30}Ni_{35}Ga_{35}$ (y= 35)	-	-	-	-	Dual Phases (β'+Ga_2NiCo)	BB	P	7.25

DD: Very ductile; D: Ductile; DB: Ductile-Brittle; B: Brittle; BB: Very brittle, *e/a* : Ni= 10, Co= 9, Ga= 3

Table 7. Results for $Co_{50}Ni_{50-x}Ga_x$ (at%) alloys serieswith x ranging up to 50

Sample	**Composition (at%)**	M_s (°C)	M_f (°C)	A_s (°C)	A_f (°C)	**Microstructure (RT)**	**Ductility**	**Magnetic Status (RT)**	*e/a*
G1	$Co_{50}Ni_{40}Ga_{10}$ (x= 10)	-	-	-	-	Dual phases (γ+β)	DD	F	8.8
G2	$Co_{50}Ni_{40}Ga_{10}$ (x = 10)	-	-	-	-	Dual Phases (γ+β)	DD	F	8.8
S	$Co_{50}Ni_{35}Ga_{15}$ (x = 15)	-	-	-	-	Single γ+Dual Phases(γ+β)	DD	F	8.45
R	$Co_{50}Ni_{32.5}Ga_{17.5}$ (x = 17.5)	-	-	-	-	Dual Phases (γ+β)	DD	F	8.2
H1	$Co_{50}Ni_{30}Ga_{20}$ (x= 20)	-	-	-	-	Dual Phases (γ+β)	DD	F	8.1
H2	$Co_{50}Ni_{30}Ga_{20}$ (x= 20)	-	-	-	-	Single γ+Dual Phases (γ+β)	DD	F	8.1
H3	$Co_{50}Ni_{30}Ga_{20}$ (x= 20)	-	-	-	-	Dual Phases (γ+β)	DD	F	8.1
H4	$Co_{50}Ni_{30}Ga_{20}$ (x= 20)	-	-	-	-	Single γ+Dual Phases(γ+β)	DD	F	8.1
P	$Co_{50}Ni_{27.5}Ga_{22.5}$ (x= 22.5)	-	-	-	-	Dual Phases (γ+β)	D	F	7.92
A1	$Co_{50}Ni_{25}Ga_{25}$ (x= 25)	-	-	-	-	Dual Phases (γ+β)	D	F	7.75
A2	$Co_{50}Ni_{25}Ga_{25}$ (x= 25)	-	-	-	-	Dual Phases (γ+β)	D	F	7.75
A3	$Co_{50}Ni_{25}Ga_{25}$ (x= 25)	-	-	-	-	Single β Phase	D	F	7.75
O	$Co_{50}Ni_{22.5}Ga_{27.5}$ (x= 27.5)	65	40	110	135	Single β'+Dual Phases(γ+β)	D	F	7.57
E1	$Co_{50}Ni_{20}Ga_{30}$ (x= 30)	-55	-55	-50	-50	Single β Phase	DB	F	7.40
E2	$Co_{50}Ni_{20}Ga_{30}$ (x= 30)	-75	-50	15	55	Single β' Phase	B	F	7.40
F1	$Co_{50}N_{10}Ga_{40}$ (x= 40)	-	-	-	-	Single β Phase	BB	P	6.7

DD: Very ductile; D: Ductile; DB: Ductile-Brittle B: Brittle; BB: Very brittle; F: Ferromagnetic; Paramagnetic, *e/a* : Ni= 10, Co= 9, Ga= 3

Chapter IV

Conclusions

The effect of bulk supercooling and rapid solidification using Electromagnetic Levitation (EML) on the near *Heusler-type* alloys with dual-phase ($Co_{46}Ni_{27}Ga_{27}$at%) and single-phase ($Co_{48}Ni_{22}Ga_{30}$at%) compositions assessed at part I of this study. Quenching $Co_{48}Ni_{22}Ga_{30}$ alloy against the copper chill led to the formation of martensite phase (β') with deep cracks along grain boundaries. DSC experiments conducted at 10°C/min gave M_s and A_s temperature of about 37.5°C and 60°C during the first heating and cooling cycle. However, slow heating/cooling at 1°C/min suppressed the martensitic and austenitic transformation temperatures to well below room temperature. Quenched microstructure of $Co_{46}Ni_{27}Ga_{27}$, on the other hand, consisted of γ dendrites surrounded by β (β') matrix. The presence of γ phase in these samples was found to decrease the M_s and A_f to less than -20°C and -2°C temperatures, respectively. The Curie temperature of $Co_{46}Ni_{27}Ga_{27}$ samples remained at about 127°C regardless of the presence of $\gamma+\beta$ phases. It was observed that:

- Bulk supercooling and rapid solidification can produce homogeneous single martensitic phase from the hyperperitectic $Co_{46}Ni_{27}Ga_{27}$ alloy, which under normal solidification form the dual $\gamma+\beta$ phases. In contrast to the martensite phase forming from $Co_{48}Ni_{22}Ga_{30}$, the off-composition martensitic phase in the supercooled $Co_{46}Ni_{27}Ga_{27}$ sample showed no grain boundaries microsegregation and embrittlement.
- The $Co_{46}Ni_{27}Ga_{27}$ sample with a high Curie temperature showed good directional magnetic properties, such as different coercivity from around 14 Oe for in-plane

direction to about 42 Oe at the 50° angle, and also different in- and out-of-plane magnetization up to saturation level.

The role of solidification variables and chemical composition in the microstructure evolution and phase transformation in the ternary alloys $Co_{50}Ni_{50-x}Ga_x$ (at%) with x ranging up to 50, and $Co_{100-2y}Ni_yGa_y$ (at%) alloys with y ranging from 15 to 35 was assessed in the part II of this study. Three main solidification paths were identified for Co-Ni-Ga different alloy systems; 1) solidification of $\beta+\gamma$ (dual-phase) via a peritectic reaction from the liquid in alloys with composition range of $10 \leq Ga \leq 30$ (at%), 2) rapid (partionless or massive) solidification of single metastable γ phase for alloys in $10 \leq Ga \leq 20$ (at%) composition range without any structural phase transformation, 3) rapid solidification (solute entrapment) of single metastable β or β' (martenstic β) phase for alloys in composition range of $25 \leq Ga \leq 30$ (at%). In some alloys with structural phase transformation, thermal stability of martensite in cyclic cooling and heating, and its transformation temperatures to austenite and reverse transformation were reported. The main findings and conclusion can be summarized as follows:

- Quenching Co-Ni-Ga alloys revealed that the β single phase microstructure in series having Ga content more than 30 at% can form but the material has deep cracks along grain boundaries. It was observed that bulk supecooling before quenching this sample series is not necessary for the formation of this single β phase. Moreover, a very low martensitic starting and finishing transformation temperatures (M_s and M_f) was obtained in both with and without supercooling samples.

- Co-Ni-Ga alloys near *Heusler* composition ($Co_{50}Ni_{25}Ga_{25}$) solidify through a peritectic reaction ($L+\gamma \rightarrow \beta$), with $\boldsymbol{\gamma}$ as the primary phase when solidified at slow cooling rates. However, metastable single β phase microstructure was observed in the supercooled samples near stoichiometric $Co_{50}Ni_{25}Ga_{25}$ composition, but with martensitic transformation temperatures below room temperature.
- $\gamma+\beta$ dual-phase microstructures enhances ductility, but the presence of the γ phase suppresses the martensitic transformation to below room temperatures.
- There is a narrow area in the ternary Co-Ni-Ga system with a single β phase that can form ferromagnetic martensite phase at room temperature or higher but most of them show deep cracks along grain boundaries. Using bulk supercooling and rapid solidification can produce a range of homogenized metastable single β phase, which transforms to the martensitic phase above room temperature without cracking.
- The supercooled $\mathbf{Co_{50}Ni_{22.5}Ga_{27.5}}$ sample ($\Delta T_{S.C.}$=147°C) in $Co_{50}Ni_{50-x}Ga_x$ series also had a metastable and non-cracked single β phase with a thermally stable martensitic transformation during cyclic cooling and heating (up to 350°C). This sample also possessed martensitic transformation and Curie temperatures well above room temperature, indicating its potential for FSMA.

  In the $Co_{100-2y}Ni_yGa_y$ series, on the other hand, paramagnetic $\mathbf{Co_{40}Ni_{30}Ga_{30}}$ alloy showed martensite to austenite transformation temperature higher than 470°C, indicating its potential as High Temperature Shape Memory Alloy (HTSMA). However, increasing the Ga amount to 35 at% in this Ni and Ga equal series caused a paramagnetic martensite with deep cracks along grain boundaries at room temperature in rapid solidification condition, and a severe grain boundaries microsegregation during normal solidification.

References:

[1] K. Ullakko, J.K. Huang, C. Kanter, R.C. O'Handley, V.V. Kokorin, Applied Physics Letter, 69 (1996) 1966-1968.

[2] V. Giurgiutiu, Smart Materials Bulletin, 2002 (2002) 7-12.

[3] Y. Liang, Y. Sutou, T. Wada, C.C. Lee, M. Taya, et.al., Scripta Materialia, 48 (2003) 1415-1419.

[4] M. Kohl, D. Brugger, M. Ohtsuka, B. Krevet, Sensors and Actuators A, 135 (2007) 92-98.

[5] I. Aaltio, O. Heczko, O. Soderberg, S.P. Hannula, Y. Bellouard, et al., Shape-Memory Alloys and Effects: Types, Functions, Modeling, and Application. In: Smart Materials, M. Schwartz (ed.), CRC Press, Florida, 2008, pp. 20-45.

[6] S.A. Wilson, R.P.J. Jourdain, Q. Zhang, R.A. Dorey, C.R. Brown, et al., Materials Science and Engineering R, 56 (2007) 1-129.

[7] R.D. James, M. Wuttig, Philosophical Magazine A, 77 (1998) 1273-1299.

[8] T. Kakeshita, T. Takeushi, T. Fukuda, T. Saburi, R. Oshima, et al., Materials Transactions, 41 (2000) 882-887.

[9] V.A. Chernenko, E. Cesari, J. pons, C. Segui, Journal of Materials Research, 15 (2000) 1496-1504.

[10] S.J. Murray, M.A. Marioni, A.M. Kukla, J. Robinson, R.C. O'Handley, S.M. Allen, Journal of Applied Physics, 87 (2000) 5774-5776.

[11] F. Albertini, L. Morellon, P.A. Algarabel, M.R. Ibarra, L. Pareti, et al., Journal of Applied Physics, 89 (2001) 5614-5617

[12] K. Oikawa, T. Ota, F. Gejima, T. Ohmori, R. Kainuma, et al., Materials Transactions, 42 (2001) 2472-2475.

[13] K. Oikawa, L. Wulff, T. Lijima, F. Gejima, T. Ohmori, et al., Applied Physics Letter, 79 (2001) 3290-3292.

[14] K.S. Sokhey, M.Manekar, M.K. Chattopadhyay, R. Kaul, S.B. Roy, et al., Journal of Physics D: Applied Physics, 36 (2003) 1366-1370.

[15] H.E. Karaca, I. Karaman, D.C. Lagoudas, H.J. Maier, Y.I. Chumlyakov, Scripta Materialia. 49 (2003) 831-836.

[16] M. Wuttig, J. Li, C. Craciunescu, Scripta Materialia, 44 (2001) 2393-2397.

[17] C. Craciunescu, Y. Kishi, T.A. Lograsso, M. Wuttig, Scripta Materialia, 47 (2002) 285-288.

[18] Y. Kishi, C. Craciunescu, M. Sato, T. Okazaki, Y. Furuya, et al., Journal of Magnetism and Magnetic Materials, 262 (2003) L186-L191.

[19] D.L. Schlagel, Y.L. Wu, W. Zhang, T.A. Lograsso, Journal of Alloys and Compounds, 312 (2000) 77-85.

[20] A.A. Cherechukin, V.V. Khovalio, R.V. Koposov, E.P. Krasnoperov, T. Takagi, et al., Journal of Magnetism and Magnetic Materials, 258-259 (2003) 523-525.

[21] G.B. Olson, Introduction: Martensite in Perspective. In: Martensite, G.B. Olson, W.S. Owen (eds.), ASM International, Materials Park, OH, 1992, pp. 1-10.

[22] M. Cohen, Phase Transformations, Wiley, USA, 1951, p. 588.

[23] G.B. Olson, A.L. Roitburd, Martensitic Nucleation. In: Martensite, G.B. Olson, W.S. Owen (eds.), ASM International, Materials Park, OH, 1992, pp. 149-174.
[24] D.P. Koistinen, R.E. Marburger, Acta Metallurgica, **7** (1959) 59-60.
[25] H. Funakubo (translated into English by J.B. Kennedy), Shape Memory Alloys, Gordon and Breach Science Publishers, 1987.
[26] A.N. Vasil'ev, A.D. Bozhko, V.V. Khovailo, I.E. Dikshtein, V.G. Shavrov, et al., Physical Review B, 59 (1999) 1113-1120.
[27] A.N. Vasil'ev, V.D. Buchel'nikov, T. Takagi, V.V. Khovailo, E.I. Estrin. Physics Uspekhi, 46 (2003) 559–588.
[28] K.F. Hane, T.W. Shield, Philosophical Magazine A: Journal of Physics: Condensed Matter, 78 (1998) 1215–1252.
[29] L. Ma˜nosa, A. Planes, Advanced Solid State Physics, 40 (2000) 361–374.
[30] O. Heczko, N. Scheerbaum, O. Gutfleisch, Magnetic Shape Memory Phenomena. In: Nanoscale Magnetic Materials and Applications, J.P. Liu, E. Fullerton, O. Gutfleisch, D.J. Sellmyer (eds.), Springer, 2009.
[31] L. Kaufman, M. Cohen, Transactions of the American Institute of Mining Engineers, 206 (1956) 1393-1401.
[32] C.M. Wayman, Physical Metallurgy, R.W. Cahn, P. Hassen (eds.), North-Holland Physics Publishing, 1983.
[33] E.C. Bain, Transactions of the American Institute of Mining Engineers, 70 (1924) 25-46.
[34] Z. Peng, Magnetoelastic Coupling in NiMnGa Ferromagnetic Shape Memory Alloy, PhD Dissertation, University of Marylad, 2006.
[35] B.A. Bilby, J.W. Christian, Institute of Metals Monograph, 18 (1955) 121-172.
[36] L.C. Chang, T.A. Read, Transactions of the American Institute of Mining Engineers, 189 (1951) 47-52.
[37] M.W. Buehler, J.W. Gilfrich, R.C. Wiley, Journal of Applied Physics, 34 (1963) 1475-1477.
[38] C.M. Wayman, J.D. Harrison, Journal of Metals, 36 (1989) 26-28.
[39] K. Otsuka, C.M. Wayman, Mechanism of Shape Memory Effect and Superelasticity. In: Shape Memory Materials, K. Otsuka and C.M. Wayman (eds.), Cambridge University Press, 1998, pp, 27-48.
[40] T. Fukuda, T. Saburi, K. Doi, S. Nenno, Materials Transactions, 33 (1992) 271-273.
[41] G.V. Kurdjumov, L.G. Khandros, Doklady Akademii Nauk SSSR, 66 (1949) 211-214.
[42] G. Edwards, J. Perkins, Shape Memory Effects in Alloys. J. Perkins (ed.), Plenum Press, 1975.
[43] D.R. Whittaker, M.F. Fillinger, Vascular and Endovascular Surgery, 40 (2006) 85-94.
[44] J. Van Humbeeck, R. Stalmans, In: Shape Memory Materials, K. Otsuka, C.M. Wayman (eds.), Cambridge University Press, 1998, p.165.
[45] R.C. O'Handley, Modern magnetic materials: Principles and applications, Wiley, USA, 2000.
[46] H.C. Ling, R. Kaplow, Materials Science Engineering, 51 (1981) 193-210.

[47] M. Wuttig, L. Liu, Journal of Applied Physics, 87 (2000) 4707-4711.
[48] V.V. Kokorin, V.A. Chernenko, E. Cesari, J. Pons, C. Segu´ı, Journal of Physics Condensed Matter 8 (1996) 6457-6463.
[49] J. Marcos, L. Manosa, A. Planes, F. Casanova, X. Batlle, et al., Physical Review B 68 (2003) 094401.
[50] V.A. Chernenko, Scripta Materialia, 40 (1999) 523–527.
[51] A.A. Cherechukin, V.V. Khovailo, R.V. Koposiv, E.P. Krasnoperov, T. Takagi, et al., Journal of Magnetism and Magnetic Materials, 258-259 (2003) 523-525.
[52] O. Hecko, L. Straka, K. Ullakko, Journal of Physics IV, 111 (2003) 959–962.
[53] J. Pons, V.A. Chernenko, R. Santamarta, E. Cesari, Acta Mater. 48 (2000) 3027-3038.
[54] K. Ullakko, J.K. Huang, V.V. Kokorin, R.C. O'Handley, Scripta Materialia, 36 (1997) 1133-1138.
[55] J. Pons, E. Cesari, C. Segui, F. Masdeu, R. Santamarta, Materials Science and Engineering A, 481-482 (2008) 57-65.
[56] R.C. O'Handley, Modern Magnetic Materials: Principles and Applications, John Wiley & Sons, Inc., USA, 2000.
[57] R.C. O' Handley, S.J. Murray, M. Marioni, H. Nembach, S.M. Allen, Journal of Applied Physics 87 (2000) 4712-4717.
[58] Y. Kishi, Z. Yajima, K. Shimizu, T. Okazai, Y. Furuya, et al., Material Science and Engineering A, 438-440 (2006) 965-969.
[59] M. Wuttig, L. Liu, K. Tsuchiya, R.D. James, Journal of Applied Physics 87 (2000) 4707-4711.
[60] O'Handley, Journal of Applied Physics, 87 (2000) 5774-5776.
[61] A.V. Srinivasan, D.M. McFarland, Smart Structures: Analysis and Design, Cambridge University Press, USA, 2001.
[62] M. Rohde, A. Schussler, Sensors and Actuators A, 61 (1997) 463-468.
[63] T.F. Kelly, J.B. Vander Sande, In: Chemistry and Physics of Rapidly Solidified Materials, B.J. Berkowitz, R.O. Scattergood (eds.), TMS AIME, Warrendale, Pennsylvania, 1982, p. 35.
[64] W.J. Boettinger, S.R. Coriel, R.F. Sekerka, In: Chemistry and Physics of Rapidly Solidified Materials, B.J. Berkowitz, R.O. Scattergood (eds.), TMS AIME, Warrendale, Pennsylvania, 1982, p. 45.
[65] A. Munitz, R. Abbaschian, In: Undercooled Alloy Phases, C.C. Koch, E.W. Collings (eds.), TMS AIME, Warrendale, Pennsylvania, 1987, p. 23.
[66] M. Cohen, M.C. Flemings, In: Rapidly Solidified Crystalline Alloys, S.K. Das, B.H. Kear, C.M. Adam (eds.), TMS AIME, Warrendale, Pennsylvania, 1985, p. 3.
[67] J.H. Perepzko, Y. Shiahara, J.S. Paik, M.C. Flemings, In: Rapid Solidification Processing: Principles and Technologies III, R. Mehrabian (ed.), NBS, Gaithersburg, Meryland, 1982, p. 28.
[68] J.L. Walker, In: Physical Chemistry of Process Metallurgy, G.R. St. Pierre (ed.), Interscience Publication, New York, 1961, p. 845.
[69] G.J. Abbaschian, M.C. Flemings, Metallurgical Transactions A, 14A (1983) 1147-1157.

[70] J.R. Rogers, M.B. Robinson, R.W. Hyers, L. Savage: Proceedings CD of the International Symposia on Experimental Methods for Microgravity Materials Science, 1991.

[71] R.C. O'Handley, Modern Magnetic Materials: Principles and Applications, Wiley, New York, 2000.

[72] T. Maki, K. Kobayashi, M. Minato, T. Tamura, Scripta Materialia, 18 (1984) 1105-1109.

[73] T. Kakeshita, T. Fukuda, Journal of Physics: Condensed Matter, 16 (2004) S5616-5618.

[74] S. Miyazaki, K. Otsuka, Metallurgical Transactions, 17A (1986) 53-63.

[75] Y. Furuya, N.W. Hagood, S. Tamoto, T. Kubota and T. Okazaki, Journal of the Japan Institute of Metals, 66 (2002) 28-33.

[76] H. C. Lin and K. M. Lin, Scripta Materialia, 34 (1996) 1537.

[77] P.J. Webster, K.R.A. Ziebeck, S.L. Town, M.S. Peak, Philosophical Magazine B, 49 (1984) 295-310.

[78] J. Soltys, Acta Physica Polonica A, 47 (1975) 521-523.

[79] V.V. Kokorin, V.A. Chernenko, Physics of Metals and Metallography, 68 (1989) 111-115.

[80] I.K. Zasimchuk, V.V. Kokorin, V.V. Martynov, A.V. Tkachenko, and V.A. Chernenko, Physics of Metals and Metallography, 69 (1990) 104-108.

[81] A.N. Vasil'ev, V.V. Kokorin, Yu.I. Savchenko, V.A. Chernenko, Soviet Physics JETP, 71 (1991) 803-808.

[82] S.J. Murray, M. Marioni, S.M. Allen, R.C O'Handley, T.A. Lograsso, Applied Physics Letter, **77** (2000) 886-888.

[83] A. Sozinov, A.A. Likhachev, N. Lanska, K. Ullakko, Applied Physics Letter, 80 (2002) 1746-1748.

[84] A. DeSimone, R.D. James, Journal of Mechanics and Physics of Solids, 50 (2002) 283-320.

[85] R.C. O'Handley, Journal of Applied Physics, 83 (1998) 3263-3270.

[86] V.A. L'vov, E.V. Gomonaj, V.A. Chernenko, Journal of Physics: Condensed Matter, 10 (1998) 4587-4596.

[87] N.F. Mott, H. Jones, The properties of Metals and Alloys, Dover, New York, 1958.

[88] E.F. Wassermann, J. Kaestner, M. Acet, P. Entel, In: Proceedings of the International Conference on Solid-Solid Phase Transformations, M. Koiwa, K. Otsuka, T. Miyazaki (eds.), The Japan Institute of Metals, Kyoto, 1999, p. 807.

[89] D.L. Schlagel, Y.L. Wu, W. Zhang, T.A. Lograsso, Journal of Alloys Compound, 312 (2000) 77-85.

[90] R.D. James, K. Hane, Acta Materialia, 48 (2000) 197-222.

[91] T. Nishizawa, K. Ishida, Co-Ni (Cobalt-Nickel). In: Binary Alloy Phase Diagrams, Second Edition, T.B. Massalski (ed.), ASM International, Materials Park, Ohio, 1990, pp. 1214–1215.

[92] H. Okamoto, Co-Ga (Cobalt-Gallium). In: Binary Alloy Phase Diagrams, Second Edition, T.B. Massalski (ed.) 2 (1990) 1186–1189.

[93] J.P. Schaffer, Magnetic Properties. In: The Science and Design of Engineering Materials, Second Edition, J.P. Schaffer, A. Saxena, S.D. Antolovich (eds.), McGraw-Hill, New York, 1999.

[94] K. Ullakko, Journal of Materials Engineering and Performance, 5 (1996) 405-409.

[95] S.Y. Chu, R. Gallagher, M. De Graef, M.E. McHenry, IEEE Transactions on Magnetics, 37 (2001) 2666-2668.

[96] Y. Sutou, Y. Imano, N. Koeda, T. Omori, R. Kainuma, et al., Applied Physics Letters, 19 (2004) 4358-4360.

[97] M. Sato, T. Okazaki, Y. Furuya, Y. Kishi, M. Wuttig, Materials Transactions, 45 (2004) 204-207.

[98] B.D Cullity, C.D. Graham, Introduction to Magnetic Materials, Second Edition, IEEE Press, John Wiley & Sons Publication, 2009.

[99] K. Oikawa, T. Ota, Y. Imano, T. Omori, R. Kainuma, et al., Journal of Phase Equilibria and Diffusion, 27 (2006) 75-82.

[100] J.L. Moran-Lopez, R. Rodriquez-Alba, F. Aguilera-Granja, Journal of Magnetism and Magnetic Materials, 131 (1994) 417-426.

[101] M. Zhang, E. Bruk, F.R. de Boer, G. Wu, Journal of Physics D: Applied Physics, 38 (2005) 1361-1364.

[102] R. Tickle, R.D. James, Journal of Magnetism and Magnetic Materials, 195 (1999) 627-638.

[103] S.J. Murrey, M.A. Marioni, A.M. Kukla, J. Robinson, R.C. O'Handley, et al., Journal of Applied Physics, 87 (2000) 5774-5776.

[104] M. Sato, T. Okazaki, Y. Furuya, M. Wuttig, Materials Transactions, 44 (2003) 372-376.

[105] Y.X. Li, H.Y. Liu, F.B. Meng, L.Q. Yan, G.D. Liu, et al., Applied Physics Letter, 84 (2004) 3594-3596.

[106] W.H. Wang, G.H. Wu, J.L. Chen, W.S. Zhan, Z. Wang, et al., Applied Physics Letter, 77 (2000) 3245-3247.

[107] D.M. Stefanescu, Science and Engineering of Casting Solidification, Second Edition Springer, 2009.

[108] M.E. Glicksman, Principles of Solidification: An Introduction to Modern Casting and Crystal Growth Concepts, Springer, New York, 2011.

[109] M.C. Flemings, Solidification Processing, McGraw-Hill, New York, 1974.

[110] P. Duwez, Transactions of the American Institute of Mining Engineers, 227 (1963) 362-365.

[111] H. Jones, Rapid Solidification of Metals and Alloys, Institution of Metallurgists, London, 1982.

[112] P. Predecki, A.W. Mullendore, N.J. Grant, Transactions of the American Institute of Mining Engineers, 233 (1965) 1581-1586.

[113] D.R. Harbur, J.W. Anderson, W.J. Maraman, Transactions of the American Institute of Mining Engineers, 245 (1969) 1055-1061.

[114] M.J. Aziz, Journal of Applied Physics, 53 (1982) 1158-1168.

[115] R. Abbaschian, W. Kurz, In: Solidification Processes and Microstructures: A Symposium in Honor of Prof. Kurz, M. Rappaz, C. Beckermann, R. Trivedi (eds.), TMS, 2004.
[116] S.L. Sobolev, Physica Status Solidi A, 156 (1996) 293-303.
[117] J.C. Baker, J.W. Cahn, Acta Metallurgica, 17 (1969) 575-578.
[118] W.J. Boettinger, S.R. Coriell, R. Trivedi, In: the 4th conference on Rapid Solidification Processing: Principles and Technologies, R. Mehrabian, P.A. Parrish (eds.), Claitor's Publishing Division, Baton Rouge, LA, 1988, pp. 13-25.
[119] S. Wannaparhun, Roles of Supercooling and Cooling Rates in the Microstructural Evolution of Copper-Cobalt Alloys, PhD Dissertation, University of Florida, 2005.
[120] M. Cohen, R. Mehrabian, In: Rapid Solidification Processing: Principles and Technologies, III, R. Mehrabian (ed.), National Bureau of Standards, Gaithersburg, 1982, pp. 1-27.
[121] Y.Kishi, Z. Yajima, K. Shimizu, T. Okazaki, Y. Furuya, et al., Materials Science and Engineering A, 481-482 (2008) 442-445.
[122] D.A. Porter, K.E. Easterling, Phase Transformation in Metals and Alloys, Nelson Thornes Ltd., UK, 2001.
[123] P.G. Debenedetti, Metastable Liquids: Concepts and Principles, Princeton University Press, 1996.
[124] A.B. Gokhale, R. Abbaschian, Space Commercialization: Platforms and Processing, F. Shahrokhi, G. Hazelrigg, R. Bayuzick (eds.), AIAA, 1990.
[125] S. Zinn, S.L. Semiatin, Elements of Induction Heating: Design, Control and Applications, ASM International, Materials Park, Ohio, 1988.
[126] E.C. Okress, D.M. Wroughton, G. Comenxtz, P.H. Brace, J.C.R. Kelly, Journal of Applied Physics, 23 (1952) 545-552.
[127] N. El-Kaddah, Metallurgical and Materials Transactions B, 14 (1983) 401-410.
[128] S.O. Kasap, Principles of Electronic Materials and Devices, Third Edition, McGraw-Hill, 2005.
[129] B.Q. Li, International Journal of Engineering Science, 32 (1994) 45-67.
[130] T.Z. Kattamis, M.C. Flemings, Metallurgical Transactions, 1 (1970) 1449-1451.
[131] G.J. Abbaschian, Metallurgical Transactions A, 14A (1983) 1147-1147.
[132] M.C. Flemings, Y. Shiohara, Materials Science and Engineering, 65 (1984) 157-170.
[133] X. Zhang, Materials Science and Engineering A, 247 (1998) 214–221.
[134] M. Leonhardt, W. Loeser, H.G. Lindenkreuz, Acta materialia. 47 (1999) 2961-2968.
[135] M.V. Kral, W.H. Hofmeister, J.E. Wittig, Scripta Materialia, 36 (1997) 157-163.
[136] S.Y. Lee, P. Nash, Ga-Ni (Galium-Nickel). In: Phase Diagrams of Binary Nickel Alloys, P. Nash (ed.), ASM International, Materials Park, Ohio, 1991.
[137] J. Liu, H. Xie, Y. Huo, H. Zheng, J. Li, Journal of Alloys and Compounds, 420 (2006) 145-157.
[138] T.B. Massalski, J.L. Murray, L.H. Bennett, H. Baker, L. Kacprzak, Binary Alloy Phase Diagram, ASM International, New York, 1987.

[139] H. Kalaantari, S. Amini, J. Hong, R. Abbaschian, Journal of Materials Science, 46 (2011) 6224-6234.
[140] M. Kaisermayr, J. Combet, H. Ipser, H. Schicketanz, B. Sepiol, et al., Physical Review B, 61 (2000) 12038-12044.
[141] M. Siewert, M.E. Gruner, A. Dannenberg, A. Hucht, S.M. Shapiro, et al., Physical Review B, 82 (2010) 064420-1-064420-11.
[142] R. Ducher, R. Kainuma, K. Ishida, Journal of Alloys and Compounds, 466 (2008) 208-213.
[143] E. Olivos, A.L. Miranda, N. Singh, R. Arroyave, A.H. Romero, Annual Physics, 524 (2012) 212-226.
[144] B.C. Dodrill, Magnetic Media, Measurements with a VSM, Lake Shore Cryotronics Inc, 2009.
[145] X.F. Dai, H.Y. Wang, G.D. Liu, Y.G. Wang, X.F. Duan, et al., Journal of Physics D: Applied Physics, 39 (2006) 2886-2889.
[146] P. Chen, K. Chen, G. H. Wuand X. X. Zhang, Journal of Materials Science, 43 (2008) 4226-4229.
[147] J. Liu, H.X. Zheng, Y.L. Huang, M.X. Xia and J.G. Li, Scripta Materialia. 52 (2005) 935-938.
[148] S. Amini, H. Kalaantari, S. Mojgani, R. Abbaschian, Acta Materialia, 60 (2012) 7123-7131.
[149] S. Amini, Synthesis of Graphene Layers from Metal-Carbon Melts: Nucleation and Growth Kinetics, PhD dissertation, University of California Riverside, 2012.
[150] D.L. Schlagel, T.A. Lograsso, A.O. Pecharsky, Materials Research Society Symposium Proceedings, 785 (2004) 219.
[151] V.A. Chernenko, J. Pons, E. Cesari, I.K. Zasimchuk, Scripta Materialia, 50 (2004), 225-229.
[152] J. Liu, M. Xia, Y. Huang, H. Zhang, J. Li, Journal of Alloys and Compounds, 417 (2006) 96-99.
[153] J.A. Dantzig, M. Rappaz, Solidification, EPFL Press, Lausanne, 2009.
[154] M.J. Aziz, Metallurgical and Materials Transactions A, 27A (1996) 671-686.
[155] H.W. Kerr, W. Kurz, International Materials Reviews, 41 (1996) 129-164.
[156] W.J. Boettinger, S.R. Coriell, Microstructure Formation in Rapidly Solidified Alloys. In: Science and Technology of the Undercooled Melt, P.R. Sahm, H. Jones, C.M. Adam (eds.), NATO ASI Series E-N0114, Martinus-Nijhof, Dodrecht, 1986, p. 81.
[157] Y. Kishi, M. De Graef, C. Craciunrscu, T.A. Lograsso, D.A. Neumann, et al., Journal De Physique IV, 112 (2003) 1021-1024.
[158] K. Prusik, H. Morawiec, B. Kostrubiec, M. Prewendowski, G. Dercz, et al., The European Physical Journal Special Topics, 158 (2008) 155-159.
[159] E. Dogan, I. Karaman, Y.I. Chumlyakov, Z.P. Luo, Acta Materialia, 59 (2011) 1168-1183.
[160] J.Z. Li, J. Liu, M.X. Zhang, J.G. Li, Journal of Alloys and Comppounds, 499 (2010) 39-42.
[161] E. Dogan, I. Karaman, N. Singh, A, Chivukula, H.S. Thawabi, et al., Acta Materialia, 60 (2012) 3545-3558.